NASA Contractor Report 3833

A Linear Aerodynamic Analysis for Unsteady Transonic Cascades

Joseph M. Verdon and Joseph R. Caspar

CONTRACT NAS3-23696
SEPTEMBER 1984

NASA

NASA Contractor Report 3833

A Linear Aerodynamic Analysis for Unsteady Transonic Cascades

Joseph M. Verdon and Joseph R. Caspar
United Technologies Research Center
East Hartford, Connecticut

Prepared for
Lewis Research Center
under Contract NAS3-23696

National Aeronautics
and Space Administration

**Scientific and Technical
Information Branch**

1984

A Linear Aerodynamic Analysis for Unsteady Transonic Cascades

TABLE OF CONTENTS

TABLE OF CONTENTS (Cont'd)

A Linear Aerodynamic Analysis for Unsteady Transonic Cascades

SUMMARY

A potential flow analysis is presented for predicting the unsteady airloads produced by the vibrations of turbomachinery blades operating at transonic Mach numbers. The unsteady aerodynamic model includes the effects of blade geometry, finite mean pressure variation across the blade row, high-frequency blade motion, and shock motion within the framework of a linearized, frequency-domain formulation. The unsteady equations are solved using an implicit, least-squares, finite-difference approximation which is applicable on arbitrary grids. A numerical solution for the entire unsteady field is determined by matching a solution determined on a rectilinear-type cascade mesh, which covers an extended blade-passage region, to a solution determined on a detailed, polar-type local mesh, which covers and extends well beyond the supersonic region(s) adjacent to a blade surface. Results are presented for cascades of double-circular-arc and flat-plate blades to demonstrate the unsteady analysis, and to partially illustrate the effects of blade geometry, inlet Mach number, blade-vibration frequency and shock motion on unsteady response.

INTRODUCTION

At transonic Mach numbers relatively small-amplitude unsteady motions can produce large variations in the magnitude and phase of the aerodynamic forces and moments. These characteristics enhance the likelihood of an aeroelastic instability and thus are a major concern in transonic design. Of particular concern are flutter boundaries. The aeroelastician is normally confronted with determining the stability of a configuration with respect to infinitesimal disturbances. For this purpose a linear unsteady aerodynamic theory is desirable. Although substantial progress has been achieved towards the development of both linear and nonlinear unsteady transonic theories for fixed wings (Ref. 1), these are either too restrictive or require too much computing time to permit their routine use in detailed turbomachinery aeroelastic investigations. Thus the objective of the present effort is to provide a linear unsteady transonic analysis for two-dimensional cascades which accounts for the effects of blade geometry and loading and applies at the frequencies of interest in turbomachinery applications. Although the attention here is focused on two-dimensional cascades, the basic aerodynamic model described in this report could also lead to useful methods for predicting the unsteady loads associated with the motions of a variety of aerodynamic configurations, including those of thick, blunt-nosed, transonic airfoils.

Linear Unsteady Aerodynamic Theories

The unsteady aerodynamic models currently used for turbomachinery aeroelastic design predictions (Ref. 2) are essentially based on classical linear theory. Here both steady and unsteady disturbances caused by airfoil shape and incidence and by airfoil motion, respectively, are regarded as being of the same order of magnitude and small relative to the free-stream speed, leading to linear, constant-coefficient, boundary-value problems for the steady and unsteady disturbance potentials. The classical formulation admits very efficient semi-analytic solutions for entirely subsonic or entirely supersonic flows, but it does not account for interactions between the steady and unsteady disturbances. Such interactions are believed to be crucial to the successful prediction of unsteady transonic airloads as well as for the understanding of a variety of turbomachinery aeroelastic phenomena. The influence of steady disturbances on unsteady response is retained in the so called "time-linearized", transonic small-disturbance approximation. Here, unsteady disturbances are regarded as small relative to steady disturbances caused by airfoil shape and incidence, which are in turn assumed to be small relative to the free-stream speed. These assumptions along with appropriate independent variable scalings provide a linear, variable-coefficient, boundary-value problem for the unsteady potential which formally applies at free-stream Mach numbers close to one, but only for low-frequency unsteady motions. Both frequency- and time-domain (Refs. 3 and 4)

finite-difference methods have been developed for the time-linearized transonic equations and applied to predict unsteady flows with moving shocks, but such methods have only been applied to flows around isolated airfoils.

The simple treatment of arbitrary airfoils and their motions are the primary advantages of the foregoing linearized unsteady models. Surface conditions can be imposed on flat, mean-surface approximations of the airfoils and their wakes. However, the assumptions, which permit this simplification, place severe restrictions on airfoil geometry and loading, and in the transonic case, on the frequency of the unsteady motion. As such, these theories fail to meet the needs of turbomachinery designers over a wide range of practical operating conditions. To partially overcome the limitations of classical theory, unsteady aerodynamic models have been formulated for subsonic cascades which include the effects of blade geometry and loading on unsteady response (Refs. 5 through 8). Here the unsteady flow is regarded as a small-amplitude harmonic fluctuation about a fully nonuniform steady flow. The steady flow is determined as a solution of the full-potential equation and the unsteady flow is governed by a linear equation with variable coefficients which depend on the underlying steady flow. Several accurate and reliable numerical solution algorithms for the nonlinear steady problem are currently available (c.f., Ref. 9). In addition, a finite-difference approximation, based on an implicit least-squares development and applicable on arbitrary grids, has been developed by the present authors for resolving the subsonic, linear, unsteady problem (Ref. 10). Results have been reported for cascades of sharp-edged, double-circular-arc and thin- circular-arc airfoils (Refs. 5 and 10) and for cascades of blunt-nosed NACA 0012 (Refs. 11 and 12) and NACA 65 series airfoils. Predictions for the NACA 65 series airfoils were found to be in excellent agreement with cascade wind tunnel measurements (Ref. 13).

Scope of the Present Investigation

In the present investigation the aerodynamic and numerical models, described in Refs. 5 and 10 through 12, have been extended for transonic applications. This has been accomplished by introducing shock-jump conditions into the linear unsteady formulation and by including the concentrated loads produced by shock motion (Refs. 14 and 15) in the determination of unsteady force and moment. In addition, rotated (Ref. 16) and type-dependent (Refs. 17 and 18) differencing strategies and shock fitting procedures have been incorporated into the unsteady numerical approximation. The numerical approximation has been implemented on both cascade and local meshes. Local mesh calculations are required to accurately resolve the flow in supersonic regions and to fit shocks into the unsteady solution. With the present unsteady transonic analysis, we seek a first-order approximation to a weak solution (i.e., a solution containing discontinuities) of the time-dependent full-potential equation for small-amplitude (infinitesimal), harmonic, blade motions. This analysis is intended for

application at reduced frequencies of order one — an important feature for turbomachinery applications — and includes the effects of blade geometry, finite mean pressure rise (or fall) across the blade row, and shocks and their motions within the framework of a linearized frequency-domain formulation. In this report the unsteady transonic aerodynamic model and numerical approximation are described, and numerical results are presented and evaluated for cascades of vibrating, sharp-edged, double-circular-arc (DCA) airfoils having their mean positions aligned with the steady flow. This simple example configuration has been selected to permit concentration on the transonic aspects of the unsteady problem (i.e., local supersonic regions and moving shocks) without introducing the additional complications associated with mean incidence and steady flow stagnation at blade leading edges.

THE POTENTIAL FLOW AERODYNAMIC MODEL

Problem Description

In the following discussion all physical quantities are dimensionless. Lengths have been scaled with respect to blade chord, time with respect to the ratio of blade chord to upstream free-stream speed, and density and pressure with respect to the upstream free-stream density and dynamic pressure, respectively. We consider adiabatic flow, with negligible body forces, of an inviscid, non-heat conducting, perfect gas through a two-dimensional oscillating cascade (Fig. 1). The mean or steady-state positions of the blade chord lines coincide with the line segments $\eta = \xi \tan \Theta + m|\vec{G}|$, $0 \leq \xi \leq \cos \Theta$, $m = 0, \pm 1, \pm 2, \ldots$, where ξ and η are the cascade axial and circumferential coordinates, m is a blade number index, Θ is the cascade stagger angle, and $\vec{G}$ is the cascade gap vector which is directed along the η-axis with magnitude equal to the blade spacing (Fig. 1). It is assumed that in the absence of blade motions uniform subsonic conditions exist far upstream and downstream of the blade row. The blades are undergoing identical harmonic motions at frequency, ω, and with constant phase angle, σ, between the motion of adjacent blades. Blade shape and orientation relative to the inlet free stream and the amplitude, frequency, and mode of the blade motion are assumed to be such that the flow remains attached to the blade surfaces. Thus, thin vortex sheets (unsteady wakes) emanate from the blade trailing edges and extend downstream. In addition, for sufficiently high subsonic inlet conditions, local supersonic regions which terminate at moving shocks will appear adjacent to blade surfaces.

Time-Dependent Full-Potential Formulation

Equations governing the fluid motion can be derived from the integral conservation laws for mass, momentum and energy, and the thermodynamic equation of state. These provide corresponding differential equations in regions where the flow variables are continuously differentiable and "jump" conditions at surfaces across which (in the inviscid approximation) the flow variables are discontinuous; i.e., at shocks and blade wakes. In continuous regions the energy equation can be replaced by the requirement that the entropy following a fluid particle must remain constant (Ref. 19). In general, the discontinuous changes in the flow quantities across shocks are proportional to the shock strength, but the increase in entropy across the shock is proportional only to the third power of the shock strength (Ref. 20). Thus for shocks of weak to moderate strength, it is a reasonable approximation to neglect changes in entropy across the shock. With this approximation, the uniform undisturbed flow far upstream of the cascade will produce an isentropic and hence, by the Helmholtz theorem, an irrotational, time-dependent flow.

Field Equation

The mass conservation law then provides the following form of the differential equation governing the fluid density, $\hat{\rho}$, and velocity potential, $\hat{\Phi}$,

$$\frac{\partial \hat{\rho}}{\partial t} + \nabla\cdot(\hat{\rho}\nabla\Phi) = 0 \qquad (1)$$

where t is time. In addition, after substituting the isentropic relations into the differential form of the momentum conservation law and integrating the resulting expression, the following relations (Bernoulli's equation) between the flow variables are obtained

$$\hat{\rho}^{(\gamma-1)} = (\gamma M_{-\infty}^2 \hat{P}/2)^{(\gamma-1)/\gamma} = (M_{-\infty}\hat{A})^2 = 1 - (\gamma-1)M_{-\infty}^2 \{\hat{\Phi}_t + [(\nabla\hat{\Phi})^2-1]/2\} \qquad (2)$$

Here γ is the specific heat ratio of the fluid, M is the Mach number of the undisturbed or steady flow, $\hat{P}$ is the fluid pressure, $\hat{A}$ is the speed of sound propagation, and the subscript $-\infty$ refers to the upstream free-stream condition. If the dependence of the density on the velocity potential is explicitly included in Eq. (1), the latter can be written in the following nonconservative form

$$\hat{A}^2\nabla^2\hat{\Phi} = \hat{\Phi}_{tt} + 2\nabla\hat{\Phi}\cdot\nabla\hat{\Phi}_t + \nabla\hat{\Phi}\cdot\nabla(\nabla\hat{\Phi})^2/2 \qquad (3)$$

Since, by assumption, unsteady disturbances are produced solely by the blade motion, the admissable solutions of either Eq. (1) or Eq. (3) for the present application are those in which acoustic energy does not radiate towards the blade row. Blade motions are then classified as subresonant if all acoustic waves attenuate in the far field; as superresonant if at least one such wave propagates axially and away from the blade row in either the far upstream or downstream directions; or as resonant if at least one wave neither attenuates nor propagates in the axial direction (Ref. 5).

Surface Conditions

The foregoing equations are supplemented by boundary conditions on moving blade surfaces, $\mathcal{B}_m$, and jump conditions at moving blade wakes, $\mathcal{W}_m$, and at moving shocks, $\mathcal{S}h_{m,\pm}$, where the subscript + or - refers to a shock emanating from the upper or lower surface, respectively, of the mth blade. The vectors $\vec{R}$, $\vec{n}$, and $\vec{\tau}$ are introduced below in conjunction with the surface conditions. The relative displacement vector, $\vec{R}$, measures the displacement of a point on the instantaneous position of a surface (blade, wake, or shock) relative to its mean or steady-state position. The unit vectors $\vec{n}$ and $\vec{\tau}$ are normal and tangent, respectively, to a surface and directed such that $\vec{n} \times \vec{\tau} = \vec{e}_z$ points out from the page. The unit normal vector is directed outward from blade surfaces, upward at wakes, and downstream at shocks.

For attached flows, the normal component of the fluid velocity must equal the normal component of the surface velocity at blade surfaces (flow tangency); i.e.,

$$\nabla\hat{\Phi} \cdot \vec{n} = \frac{\partial \vec{R}}{\partial t} \cdot \vec{n} , \qquad \text{on } \mathcal{B}_m \tag{4}$$

where the vector $\vec{R}$ is prescribed. The blade wakes are also material surfaces; i.e., a fluid particle on the wake always remains there. Hence, Eq. (4) also applies at wake surfaces. However, since the wake displacement vector is unknown a priori, "wake-jump" conditions are usually imposed. It follows from the foregoing kinematic condition and the integral conservation laws that the component of fluid velocity normal to the wake and the thermodynamic properties of the fluid must be continuous across thin vortex wakes. Thus, the conditions

$$[\![\nabla\hat{\Phi}]\!] \cdot \vec{n} = [\![\hat{P}]\!] = 0 , \qquad \text{on } \mathcal{W}_m \tag{5}$$

apply at wake surfaces, where $[\![\ ]\!]$ denotes that difference (upper minus lower) in a quantity across a wake. Since the instantaneous wake locations, $\mathcal{W}_m$, are unknown, the usual procedure is to apply these conditions on prescribed surfaces which lie close to the actual wake positions.

At shocks the integral form of the mass conservation law provides the following condition

$$\left[\!\left[\hat{\rho}(\nabla\hat{\Phi} - \frac{\partial\vec{\hat{R}}}{\partial t})\right]\!\right]\cdot\vec{n} = 0 \ , \quad \text{on } \mathcal{S}\!\mathcal{h}_{m,\pm} \tag{6}$$

where $[\![\ ]\!]$ denotes the jump or difference (downstream minus upstream) in a quantity across a shock. Note that the normal shock-displacement must be determined as part of the solution. Thus a second shock-jump condition is required. This follows from the conservation of momentum tangent to the shock and requires that the component of fluid velocity tangent to the shock or, after integrating along the shock, that the velocity potential must be continuous across the shock; i.e.,

$$\vec{\tau}\cdot\left[\!\left[\nabla\hat{\Phi}\right]\!\right] = \left[\!\left[\hat{\Phi}\right]\!\right] = 0, \quad \text{on } \mathcal{S}\!\mathcal{h}_{m,\pm} \tag{7}$$

Equation (7) also represents the requirement that no vorticity be produced at the shock. In the potential approximation neither the normal component of fluid momentum nor energy is conserved across a shock.

This completes the formulation of the boundary value problem for the velocity potential, $\hat{\Phi}$. The problem posed is a formidable one consisting of a nonlinear, time-dependent, partial differential equation along with conditions imposed on moving blade, shock and wake surfaces, in which the instantaneous locations of shock and wake surfaces must, in principle, be determined as part of the solution. Even if accurate solution procedures could be developed for this problem, they would be of limited practical value because their computing time requirements would make it prohibitively expensive to obtain the unsteady response predictions required for detailed flutter calculations. Thus in the present effort we will derive a first-order approximation to the foregoing boundary value problem for small-amplitude blade motions with the intention of providing a useful analytical model for turbomachinery aeroelastic investigations.

THE SMALL UNSTEADY-DISTURBANCE APPROXIMATION

Linearization

For small-amplitude blade motions; i.e., $|\vec{R}_\beta| \sim \mathcal{O}(\varepsilon) \ll 1$, an approximate solution for the time-dependent flow can be determined by employing a perturbation analysis. Flow variables are first expanded in an asymptotic series in ε; e.g.,

$$\hat{\Phi}(\vec{\hat{X}},t) = \phi_0(\vec{\hat{X}}) + \varepsilon\phi_1(\vec{\hat{X}},t) + \mathcal{O}(\varepsilon^2) \tag{8}$$

where $\vec{\hat{X}}$ is a position vector referred to the space-fixed x,y-Cartesian coordinate frame of Fig. 1. In addition, Taylor series expansions; e.g.,

$$\nabla\hat{\Phi}|_{\mathcal{S}} = \nabla\hat{\Phi}|_S + (\vec{R}\cdot\nabla)\nabla\hat{\Phi}|_S + \mathcal{O}(\varepsilon^2) \tag{9}$$

are applied to refer information at a moving blade, wake, or shock surface to the mean position of this surface. In Eq. (9) the subscripts $\mathcal{S}$ and S refer to the instantaneous and mean surface locations, respectively, and $\vec{R}$ measures the displacement of a point on the moving surface relative to its mean position. Unit tangent and normal vectors at a point on a moving surface are expressed in terms of the unit tangent and normal vectors at the location of this point on the mean surface by the following relations

$$\vec{\tau}_{\mathcal{S}} = \vec{\tau}_S\,[1 - \vec{\tau}_S\cdot\nabla\vec{R}\cdot\vec{\tau}_S] + (\vec{\tau}_S\cdot\nabla)\vec{R} + \mathcal{O}(\varepsilon^2) \tag{10a}$$

$$\vec{n}_{\mathcal{S}} = \vec{\tau}_{\mathcal{S}} \times \vec{e}_z = \vec{n}_S\,[1 - \vec{\tau}_S\cdot\nabla\vec{R}\cdot\vec{\tau}_S] + (\vec{\tau}_S\cdot\nabla)\vec{R} \times \vec{e}_z + \mathcal{O}(\varepsilon^2) \tag{10b}$$

After substituting the foregoing series expansions and surface vector relations into the full governing equations, equating terms of like power in ε and neglecting terms of second and higher order in ε, nonlinear and linear, variable-coefficient, boundary value problems are obtained, respectively, for the zeroth- and first-order flows.

As $\varepsilon \to 0$ the blade surfaces collapse to their mean positions. Hence, the zeroth-order term, $\phi_0(\vec{X})$, of the asymptotic expansion (8) is the velocity potential, $\Phi(\vec{X})$, due to steady flow past a stationary cascade. Since the first-order, unsteady problem is linear, the first-order potential induced by the harmonic blade motions must also have harmonic time-dependence. We take advantage of this feature by introducing a complex representation; e.g., $\varepsilon\phi_1(\vec{X},t) = \phi(\vec{X})e^{i\omega t}$, for all first-order flow properties, including the surface-displacement vectors, and adopting the convention that the real parts of these complex parameters represent the actual time-dependent physical quantities. The complex representation serves to remove explicit time dependence from the unsteady boundary value problem thereby facilitating the determination of a solution. In addition, the cascade geometry, the prescribed form of the blade motion; i.e.,

$$\vec{R}(\vec{X} + m\vec{G}, t) = \vec{r}(\vec{X})e^{i(\omega t + m\sigma)}, \qquad \vec{X} \text{ on } B \tag{11}$$

where $\vec{R}$ is now a complex displacement vector and the vector $\vec{r}$ defines the amplitude and direction of the reference blade displacement, and the linearity of the first-order problem require that both the steady and unsteady flows exhibit blade-to-blade periodicity. Thus

$$\Phi(\vec{X}) = \Phi(\vec{X} + m\vec{G}) - m\vec{V}_{-\infty}\cdot\vec{G} \tag{12a}$$

$$\phi(\vec{X}) = \phi(\vec{X} + m\vec{G})e^{-im\sigma} \tag{12b}$$

Conditions (12a) and (12b) allow a numerical resolution of the steady and unsteady flows to be limited to a single, extended, blade-passage region of the cascade and permit properties at the mth blade, wake, or shock surface to be evaluated in terms of information provided at the corresponding reference ($m = 0$) surface. For simplicity, the subscript m will be omitted in the following discussion when referring to a reference surface.

It should be noted that the foregoing linearization is not valid in the neighborhood of a moving shock (Refs. 14 and 15). An observer situated between the extreme shock positions will experience large-amplitude jumps in the flow variables as the shock passes by. Such local anharmonic effects can be accounted for by including additional terms in the asymptotic representations of the flow variables (c.f. Ref. 14). However, since these terms do not impact the steady or unsteady boundary value problems, we defer their introduction to the subsequent discussion on unsteady aerodynamic response.

The Steady and Unsteady Boundary Value Problems

Equations governing the steady flow, which is assumed to be known in the present study, follow from Eqs. (1) through (4), (6) and (7), after replacing the time-dependent flow quantities, $\hat{\Phi}$, $\hat{P}$, $\hat{\rho}$, and $\hat{A}$, by their zeroth-order or steady flow counterparts, Φ, P, $\bar{\rho}$ and A, and setting time-derivative terms equal to zero. The steady flow tangency and shock-jump conditions are imposed at the mean positions of the blade, B_m, and shock $Sh_{m,\pm}$, surfaces, and uniform subsonic conditions are imposed far upstream ($\xi \to -\infty$) and downstream ($\xi \to \infty$) from the blade row. In general, three of the following quantities: the inlet Mach number, $M_{-\infty}$, the inlet flow angle, $\Omega_{-\infty}$, the exit Mach number, M_{∞}, or the exit flow angle, Ω_{∞}, are prescribed and the fourth is determined by a global mass balance. However, for sharp-edged blades, conditions (e.g., a Kutta condition at blade trailing edges) can be imposed at blade leading and/or trailing edges in lieu of prescribing an inlet and/or an exit flow parameter. Note that the wake-jump conditions are automatically satisfied in the two-dimensional steady problem since the steady flow is continuous downstream of the blade row. Further, since the shock locations are unknown a priori, the usual practice in steady flow calculations is to express the field equation in conservative form and then to solve this equation through shocks. Thus the shock-jump conditions are usually not imposed and steady shock phenomena are said to be captured.

It follows from the differential form of the mass conservation law, Eq. (1), the Bernoulli relations, Eq. (2), and the asymptotic expansions for the flow variables (e.g., Eq. (8)) that the linear unsteady flow is governed by the conservative-form equation

$$i\omega\rho + \nabla\cdot\left[\bar{\rho}\nabla\phi + \rho\nabla\Phi\right] = 0 \tag{13}$$

and that the complex amplitudes of the unsteady density, ρ, pressure, p, speed of sound, a, and velocity potential, ϕ, are related by

$$\rho/\bar{\rho} = \gamma^{-1}\, p/P = \left(\frac{2}{\gamma - 1}\right) a/A = -A^{-2}\,\frac{D_S\phi}{Dt} \tag{14}$$

where D_S/Dt is a mean-flow convective derivative operator; i.e.,

$$\frac{D_S}{Dt} = \frac{\partial}{\partial t} + \nabla\Phi\cdot\nabla = i\omega + \nabla\Phi\cdot\nabla \tag{15}$$

Upon substituting the steady and unsteady, Eq. (14), Bernoulli relations into Eq. (13), or alternatively, the series expansion, Eq. (8), into the nonconservative, time-dependent, full-potential equation, Eq. (3), and performing some algebra, the following field equation for the unsteady potential is obtained

$$A^2\nabla^2\phi = \frac{D_S^2\phi}{Dt^2} + (\gamma - 1)\nabla^2\Phi\,\frac{D_S\phi}{Dt} + \nabla(\nabla\Phi)^2\cdot\nabla\phi/2 \tag{16}$$

Since we intend to fit shocks into the unsteady solution; i.e., to satisfy the first-order shock-jump conditions, we will seek a numerical solution to this nonconservative field equation for prescribed blade motions.

Surface Conditions

Conditions on the unsteady flow at blade, wake, and shock mean positions are similarly obtained by substituting the asymptotic and Taylor series expansions and the surface vector relations, Eqs. (10), into the time-dependent flow tangency, Eq. (4), wake-continuity, Eqs. (5), and shock-jump, Eqs. (6) and (7), conditions. After performing some straightforward algebra, the following conditions on the linear unsteady flow are determined. The first-order flow tangency condition has the form

$$\nabla\phi\cdot\vec{n} = \left[i\omega\vec{r} + (\nabla\Phi\cdot\vec{\tau})(\vec{\tau}\cdot\nabla)\vec{r} - (\vec{r}\cdot\nabla)\nabla\Phi\right]\cdot\vec{n}e^{im\sigma}, \quad \text{on } B_m \tag{17}$$

The first term on the right-hand-side of Eq. (17) is the velocity of the blade motion. The second and third terms account for the effects of a varying displacement along the blade surface and of motion through a spatially varying mean velocity field, respectively. Since the steady flow is continuous downstream of the blade row, the conditions of continuity of normal velocity and pressure across blade wakes (c.f., Eqs. (5)) reduce to

$$\left[\!\left[\nabla\phi\right]\!\right]\cdot\vec{n} = \left[\!\left[\frac{D_S\phi}{Dt}\right]\!\right] = 0, \quad \text{on } W_m \tag{18}$$

where the wake mean positions, W_m, are assumed to coincide with the downstream, steady-flow, stagnation streamlines.

At shocks, conservation of mass and tangential momentum require that

$$\left(i\omega r_n + \Phi_\tau \frac{\partial r_n}{\partial \tau}\right) e^{im\sigma}\left[\!\left[\bar{\rho}\right]\!\right] = \left[\!\left[\bar{\rho}\nabla\phi + \rho\nabla\Phi\right]\!\right]\cdot\vec{n} + r_n e^{im\sigma}\left[\!\left[(\bar{\rho}\Phi_n)_n\right]\!\right], \text{ on } Sh_{m,\pm} \tag{19}$$

and

$$\left[\!\left[\phi\right]\!\right] + e^{im\sigma} r_n \left[\!\left[\Phi_n\right]\!\right] = 0, \text{ on } Sh_{m,\pm} \tag{20}$$

respectively, where

$$\vec{R}\,(\vec{X} + m\vec{G},\ t)\cdot\vec{n} = r_n e^{i(\omega t + m\sigma)}, \qquad \vec{X} \text{ on } Sh_{\pm} \tag{21}$$

and r_n is the complex amplitude of the shock displacement normal to the mean shock locus. For normal shocks $\Phi_\tau\big|_{Sh} = 0$, and it follows from the zeroth-order continuity equation that $\left[\!\left[(\bar{\rho}\Phi_n)_n\right]\!\right] = 0$. Therefore from Eqs. (19) and (20) we have

$$i\omega r_n e^{im\sigma}\left[\!\left[\bar{\rho}\right]\!\right] = -\,i\omega\left[\!\left[\bar{\rho}\right]\!\right]\left[\!\left[\phi\right]\!\right] / \left[\!\left[\Phi_n\right]\!\right] = \left[\!\left[\bar{\rho}\phi_n + \rho\Phi_n\right]\!\right], \text{ on } Sh_{m,\pm} \tag{22}$$

After employing the zeroth- and first-order Bernoulli relations to eliminate ρ in Eq. (22) and rearranging the resulting expression, the following relation for the jump in the unsteady potential across the shock is obtained.

$$\begin{aligned} i\omega\left[\!\left(\left[\!\left[\bar{\rho}\right]\!\right] - M_{-\infty}^2\,\bar{\rho}^{(2-\gamma)}\Phi_n\left[\!\left[\Phi_n\right]\!\right]\right)\phi\right]\!\right] \\ = \left[\!\left[\Phi_n\right]\!\right]\left[\!\left[\bar{\rho}\,(M_{-\infty}^2\,\bar{\rho}^{(1-\gamma)}\Phi_n^2 - 1)\,\phi_n\right]\!\right], \text{ on } Sh_{m,\pm} \end{aligned} \tag{23}$$

where $\bar{\rho}$, Φ, and the mean shock locations, $Sh_{m,\pm}$, are assumed to be known from the steady solution. Equations (23) and (20) provide the required relations for determining the jump in the unsteady potential at the mean location of a normal shock and the complex amplitude of the shock displacement in the streamwise direction. The latter quantity is required to determine the concentrated loads produced by the shock motion.

Unsteady Far-Field Behavior

In general unsteady disturbances do not attenuate with distance from the blade row, and hence, it is difficult to place explicit conditions on the unsteady potential in the far field. However, under uniform subsonic inlet and exit conditions, the departure of steady flow quantities from their free-stream values will be of $\mathcal{O}(\varepsilon)$ beyond some finite distances upstream and downstream from the blade row, say $\xi \leq \xi_-$ and $\xi \geq \xi_+$, where ξ is the cascade axial coordinate (Fig. 1). Thus to within the first-order approximation considered here, the unsteady differential equation, Eq. (16), reduces to constant coefficient equations, for which analytic far-field solutions can be determined. The unsteady potential is continuous upstream of the blade row and has both a continuous and a discontinuous component downstream. The continuous potential accounts for acoustic wave propagation. Fourier methods (Refs. 5 and 21) can be used to provide expressions for this component of the potential in the far field in terms of the cascade axial and tangential coordinates ξ and η (Fig. 1). The discontinuous component of the unsteady potential accounts for the counter-vorticity shed from the blade trailing edges and convected along the blade wakes. A closed-form solution for the discontinuous component of the potential in the far field has been determined in terms of Cartesian coordinates parallel and normal to the far-downstream reference ($m = 0$) wake (c.f., Refs. 5 and 21). These analytic solutions can be matched to a near-field numerical solution, and thus serve to complete the specification of the unsteady boundary value problem.

AERODYNAMIC RESPONSE COEFFICIENTS

Surface Pressure Distributions

Solutions to the steady and unsteady boundary value problems are required to determine surface pressure distributions and unsteady airloads. The latter are the important results of an aerodynamic analysis intended for flutter prediction, since they permit the evaluation of aerodynamic work per cycle and/or aerodynamic damping (Ref. 22), either of which can be used to determine whether the airstream tends to support or suppress a prescribed blade motion. The pressure acting at the instantaneous position of the mth blade surface is given by

$$\hat{P}_{\mathcal{B}_m}(\tau,t) = P_B(\tau) + \mathrm{Re}\left\{p_{\mathcal{B}}(\tau)e^{i(\omega t+m\sigma)}\right\}$$

$$+ P_{\mathcal{S}h_{m,+}}(\tau,t) + P_{\mathcal{S}h_{m,-}}(\tau,t) + \ldots \qquad (24)$$

where τ is a coordinate measuring distance in the counter-clockwise direction along the mean blade surface. The first two terms on the right-hand-side of Eq. (24) are the steady and first-harmonic components of the pressure acting at the mth moving blade surface outside the small intervals bounded by the mean and instantaneous shock locations. The third and fourth terms represent the anharmonic contributions to the unsteady surface pressure caused by the motion of the shocks along the upper and lower surfaces of the mth blade.

After expanding the pressure $\hat{P}$ in the manner indicated by Eqs. (8) and (9), it follows from the steady and unsteady Bernoulli relations that

$$P_B = 2(\gamma M_{-\infty}^2)^{-1}\,(M_{-\infty}A)_B^{2\gamma/(\gamma-1)} \qquad (25)$$

and

$$p_{\mathcal{B}} = \left[-2(M_{-\infty}A)^{2/(\gamma-1)}\,\frac{D_S\phi}{Dt} + (\dot{\vec{r}}\cdot\nabla)P\right]_B \qquad (26)$$

Thus the steady and the first-harmonic components of the pressure acting at a moving blade surface, $\mathcal{B}_m$, are evaluated in terms of information supplied at the mean position, B, of the reference blade. The first term of the right-hand-side of Eq. (26) is the harmonic unsteady pressure at the mean position of the reference blade and the second is the harmonic pressure produced by motion through a spatially varying steady pressure field.

The local anharmonic effect caused by shock motion is accounted for by assuming that (c.f. Ref. 14)

$$P_{\mathcal{S}_h}(\tau,t) = -\frac{\mathrm{Re}\{r_n(0)\}}{|\mathrm{Re}\{r_n(0)\}|}\, H[(\tau-\tau_{Sh})(\tau_{\mathcal{S}_h}-\tau)]\, Q(\tau,t) \tag{27}$$

where $r_n(0)$ is the displacement of the shock foot along the blade surface,

$$H(\tau) = \begin{cases} 0, & \tau < 0 \\ 1, & \tau > 0 \end{cases} \tag{28}$$

and

$$Q(\tau,t) = [\![P_B]\!] + (\tau-\tau_{Sh})\,[\![\partial P_B/\partial\tau]\!] + \mathrm{Re}\,\{[\![P_\beta]\!]e^{i(\omega t+m\sigma)}\} \tag{29}$$

The first two terms on the right-hand-side of Eq. (24) are discontinuous at the undisturbed shock locations. The third and fourth terms cancel these discontinuities and transfer them to the instantaneous shock locations. Thus after setting $\tau = \tau_{\mathcal{S}_h}$ in the foregoing equations it follows that

$$[\![\hat{P}_\beta]\!]_{\mathcal{S}_h} = [\![P_B]\!] + (\tau_{\mathcal{S}_h} - \tau_{Sh})\,[\![\partial P_B/\partial\tau]\!] + \mathrm{Re}\{[\![P_\beta]\!]\, e^{i(\omega t+m\sigma)}\} \tag{30}$$

The discontinuous terms on the right-hand-side of Eqs. (29) and (30) are evaluated at the mean position of the shock foot. Although the unsteady pressure disturbance is not everywhere harmonic, its regions of anharmonicity are small. Consequently (c.f., Refs. 3 and 23), the first-order global aerodynamic coefficients are harmonic in time.

Unsteady Force and Moment

Up to this point we have placed no restriction on the mode of the blade motion. But we now limit consideration to the case usually considered in turbomachinery flutter calculations wherein each incremental blade section is undergoing a rigid-body motion. In this case only the unsteady force and moment coefficients must be determined to analyze the stability of the blade motion. For rigid blade motions the first-order displacement-amplitude vector is given by

$$\vec{r}(\vec{X}) = \vec{h} + \vec{\alpha} \times \vec{R}_p \qquad , \vec{X} \text{ on } B \tag{31}$$

where $\vec{h}$ defines the amplitude and direction of blade translations, $\vec{\alpha}$ defines the amplitude and direction (positive counter-clockwise) of blade rotations, and $\vec{R}_p$ is a position vector extending from the mean position of the reference blade axis of rotation (i.e., the point X_p, Y_p) to points on the mean position of the reference blade surface. These rigid two-dimensional motions model bending and torsional vibrations of actual rotor blades. The components, h_x, h_y, and α, are, in general, complex to permit phase differences between the translations in the x- and y-directions and the rotation.

The force and moment (coefficients) acting on the mth blade surface are given by

$$\hat{\vec{C}}_{F_m} = \text{Re}\left\{-\oint_{\beta_m} \hat{P}\,\vec{n}\,d\tau\right\} = \vec{C}_F + \text{Re}\left\{\vec{c}_F\, e^{i(\omega t + m\sigma)}\right\} + \mathcal{O}(\epsilon^2) \tag{32}$$

and

$$\hat{C}_{M_m} = \text{Re}\left\{\oint_{\beta_m} \hat{P}\,\hat{\vec{R}}_p \cdot d\vec{\tau}\right\} = C_M + \text{Re}\left\{c_M e^{i(\omega t + m\sigma)}\right\} + \mathcal{O}(\epsilon^2) \tag{33}$$

where the moment is taken about the moving pitching axis and $\hat{\vec{R}}_p$ extends from this axis to points on the moving blade surface. After some algebra, it follows that the complex amplitudes of the unsteady force and moment can be determined in terms of information evaluated at the mean position of the reference blade; i.e.,

$$\vec{c}_F = \vec{\alpha} \times \vec{C}_F - \oint_B p_\beta\,\vec{n}\,d\tau + r_n(0)\left[\!\left[P_B\right]\!\right]\vec{n}_B\Big|_+ + r_n(0)\left[\!\left[P_B\right]\!\right]\vec{n}_B\Big|_- \tag{34}$$

and

$$c_M = \oint_B p_\beta\,\vec{R}_p \cdot d\vec{\tau} - r_n(0)\left[\!\left[P_B\right]\!\right](\vec{R}_p \cdot \vec{\tau}_B)\Big|_+ - r_n(0)\left[\!\left[P_B\right]\!\right](\vec{R}_p \cdot \vec{\tau}_B)\Big|_- \tag{35}$$

Recall that p_β is the complex amplitude of the harmonic unsteady surface pressure, Eq. (26), the subscript B refers to the mean blade surface, and r_n is the streamwise shock displacement. The last two terms in Eqs. (34) and (35) account for the concentrated loads due to shock motion, and they are evaluated at the mean positions of the shock roots.

THE UNSTEADY NUMERICAL APPROXIMATION

For simplicity the numerical approximation will be outlined for transonic flow through a cascade of oscillating, sharp-edged airfoils in which at most a single shock occurs in each blade passage. Thus unsteady phenomena associated with mean flow stagnation (c.f. Refs. 11 and 12) and multiple shocks are omitted from present consideration. A numerical resolution of the linear, variable-coefficient, unsteady, boundary-value problem is required over a single, extended, blade-passage region of finite extent. The unsteady differential equation must be solved in continuous regions of the flow, subject to boundary or jump conditions at the mean positions of the blade, wake and shock surfaces. Blade mean positions are prescribed, and the mean positions of wake (i.e., the downstream stagnation streamlines) and shock surfaces are determined as part of the steady solution. Finally, the unsteady, near-field, numerical solution must be matched to far-field analytical solutions at finite distances ($\xi = \xi_{\mp}$) upstream and downstream from the blade row. The major elements of the numerical approximation, i.e., the discrete domains or calculation meshes, the finite-difference model, and the solution procedure are described briefly below.

Calculation Meshes

In view of the stringent and often conflicting requirements placed on the construction of a computational mesh for cascade flows, we have adopted a two-step solution procedure for the resolution of unsteady cascade flows. The basic approach is to first capture large scale unsteady phenomena on a rectilinear-type cascade mesh of moderate density and then to determine a solution on a dense, polar-type local grid. The cascade mesh covers the extended-blade-passage solution domain, while the local mesh covers (and extends well beyond) a region of high velocity gradient; for example, near a rounded leading edge in Refs. 11 and 12 or near a shock in the present study. The velocity potential distribution as determined by the cascade mesh solution provides the outer boundary condition information for the local mesh calculation. The solution to the unsteady boundary value problem is taken to be the local solution in a region covered by a local mesh and the cascade solution elsewhere.

The cascade mesh is the periodic and body-fitted, but non-orthogonal, one shown in Fig. 2a. It is composed of axial lines (ξ = constant) which are parallel to the blade row making the mesh periodic, and tangential curves which are percentile averages of the upper and lower boundaries making the mesh body-fitted over most of the blade and wake surfaces. This mesh facilitates the implementation of blade and wake boundary conditions as well as the cascade periodicity conditions. It also allows for a convenient matching of the

analytical and numerical unsteady solutions at the far field boundaries. However, the cascade mesh does not provide an accurate solution near rounded blade edges or near shocks. Moreover, for staggered cascades this mesh is not well-suited for the accurate implementation of transonic differencing procedures.

Thus in the present study, a local mesh such as that shown in Fig. 2b is applied to resolve the flow in the vicinity of a normal shock and in the supersonic region lying adjacent to the blade surface and upstream of the shock. This mesh consists of radial and circumferential lines, normal and roughly parallel, respectively, to the reference blade surface. Two of the radial lines (herein referred to as the upstream and downstream shock mesh lines) are positioned at the mean location of the shock foot so that information on the upstream and downstream side of the shock can be accurately represented. Hence, the mean shock locus is currently approximated as being normal to the airfoil surface in the local unsteady calculation. The local mesh facilitates the implementation of the unsteady shock-jump conditions as well as the implementation of rotated and type-dependent transonic differencing approximations. At present unsteady transonic solutions are calculated by the two-step procedure just described in which the local solution is essentially a correction to the cascade solution. Because of this it is necessary to choose a rather extensive local region.

Difference Approximation

Algebraic approximations to the various linear operators, which make up the unsteady boundary value problem, are obtained using the implicit, least-squares, interpolation procedure of Ref. 10. Thus consider a linear differential operator $\mathcal{L}$ which operates on a constant by multiplying that constant by q^0. An algebraic approximation, $L\phi$, to $\mathcal{L}\phi$ at the mesh point Q_0 can be written in terms of the values of ϕ at Q_0 and at certain neighboring points, Q_1, ..., Q_m, which together with Q_0 are called a neighbor set. This approximation can be expressed in the form

$$(\mathcal{L}\phi)_0 \approx (L\phi)_0 \equiv q^0\phi_0 + \sum_{m=1}^{M} \beta_m(\phi_m-\phi_0) \tag{36}$$

where the difference coefficients, β_m, are evaluated in terms of a prescribed set of interpolating functions and a set of interpolating coefficients. The latter are determined by a weighted least-squares procedure. For the present application the neighbor sets are defined as shown in Fig. 2; i.e., in a "centered" fashion for interior points and in a one-sided fashion for boundary

points. The foregoing finite-difference model along with its application to unsteady subsonic cascades has been described in detail in Refs. 10 and 11. Here we describe only those modifications to the overall difference approximation which are required for transonic applications.

Transonic Differencing Strategies

Following Murman and Cole (Refs. 17 and 18), the plan is to distinguish between regions of subsonic flow where the unsteady differential equation is elliptic and supersonic flow where it is hyperbolic and to use a differencing scheme which is sensitive to its local character. To accomplish this we first apply the rotated differencing concept introduced by Jameson (Ref. 16). Thus at each point of the discrete domain the field equation is expressed in canonical form; i.e.,

$$\mathcal{L}_0\phi = (\mathcal{L}_1 + \mathcal{L}_2)\phi \tag{37}$$

where

$$\mathcal{L}_1\phi = A^2(1-M^2)\phi_{SS} = M^{-2}(1-M^2)(\Phi_\xi^2\phi_{\xi\xi}+2\Phi_\xi\Phi_\eta\phi_{\xi\eta}+\Phi_\eta^2\,\phi_{\eta\eta})$$

$$\mathcal{L}_2\phi = A^2\phi_{NN} + \ldots = M^{-2}[\Phi_\eta^2\,\phi_{\xi\xi}-2\Phi_\xi\Phi_\eta\phi_{\xi\eta} + \Phi_\xi^2\,\phi_{\eta\eta}] + \ldots \tag{38}$$

S and N are the local canonical coordinates; i.e., the Cartesian coordinates aligned with and normal to, respectively, the local steady flow direction, and ξ and η are the computational coordinates; i.e., the cascade axial and circumferential coordinates (Fig. 1). The principal part of the unsteady differential equation is shown explicitly in Eq. (38) and the dots refer to the remaining terms.

It is now clear that the local character of the unsteady differential equation depends on the local steady Mach number, and it becomes a simple matter to construct a suitable type-dependent differencing scheme. Thus, the linear operator $\mathcal{L}_2$ is always approximated by a central difference expression, but the difference approximation to the operator $\mathcal{L}_1$ will depend on the local steady Mach

number, and hence, on the local type of the unsteady field equation. If $M_{i,j}$ is less than one, where the indices i and j refer to the axial and tangential lines, respectively, of the cascade mesh or to the radial and circumferential lines, respectively, of the local mesh, the flow is locally subsonic (elliptic) and we set

$$\mathcal{L}_1\phi|_{i,j} \approx L_1\phi|_{i,j} , \qquad M_{i,j} < 1 \tag{39}$$

where L_1 is a central difference operator. If $M_{i,j}$ is greater than one, the flow is locally supersonic (hyperbolic) and $(\mathcal{L}_1\phi)_{i,j}$ is approximated by the retarded or upwind difference expression

$$\mathcal{L}_1\phi|_{i,j} \approx L_1\phi|_{i-1,j} , \qquad M_{i,j} > 1 \tag{40}$$

i.e., a central difference expression evaluated at the previous upstream mesh point on the jth tangential or circumferential mesh line. Strictly speaking, at supersonic points the differencing should be retarded along both sets of mesh lines in the cascade and local calculations, but since the tangential and circumferential mesh lines are closely aligned with the mean flow direction, it should be sufficient to employ upwind differencing only along these lines.

Unsteady shock phenomena are captured in the cascade calculation; i.e., the unsteady differential equation is approximated, using either Eq. (40) or Eq. (39) at the field points immediately upstream or downstream, respectively, of the mean shock location. Shocks are subsequently fitted into the local unsteady solution by imposing the jump condition, Eq. (23), at shock points on the downstream shock mesh line. The shock-jump condition is modeled using one-sided difference approximations (first-order accurate on the upstream side and second-order accurate on the downstream side) to evaluate the normal derivatives of the unsteady potential at the shock mean position. At points on the downstream shock mesh line at which the steady flow is continuous, the condition $[\![\phi]\!] = 0$ is imposed. To assist in evaluating the numerical solution procedure, a shock capturing option has also been included in the local calculation. In this case the condition $[\![\phi]\!] = 0$ is imposed at all points on the downstream shock mesh line.

Solution Procedure

For the cascade calculation all neighbor points fall on the axial mesh line through the calculation point and on the two immediately adjacent axial mesh lines. This placement leads to a desirable structure for the system of algebraic equations which approximate the unsteady boundary value problem. At a field or interior point the unsteady differential equation is approximated using neighbor sets centered at this point and, if the flow is locally supersonic, at the adjacent upstream point. The field equation is approximated at points on the upper, upstream, periodic boundary with ϕ values at neighbors above the mesh region related to ϕ values at points within the mesh region by the periodic condition of Eq. (12b). On the lower periodic boundary the periodic condition is applied directly. For points on the far-upstream or far-downstream boundaries (i.e., at $\xi = \xi_{\mp}$) ϕ values at the neighbors upstream or downstream, respectively, of the mesh region are related to ϕ values at the boundaries using the far-field analytic solutions of Ref. 5. Finally, at blade and wake points the flow tangency condition, Eq. (17), and the wake continuity conditions, Eqs.(18), are approximated, respectively, using one-sided neighbor sets.

For the local calculation, neighbor sets are chosen in a similar fashion; i.e., centered at field points and one-sided at points on the blade surface. With the exception of those points on the upstream shock mesh line, the unsteady differential equation and flow tangency condition are approximated as described above. At the upstream shock mesh line derivatives normal to the flow direction are evaluated only in terms of information provided along this mesh line; i.e., without crossing the shock. On the downstream shock mesh line the shock-jump condition, Eq. (23), is approximated at shock points and the condition $[\![\phi]\!] = 0$ is applied at the remaining points. The normal derivative, ϕ_n, in Eq. (23) is approximated by first- and second-order accurate one-sided difference expressions on the upstream (supersonic) and downstream (subsonic) sides of the shock, respectively. Thus the streamwise derivatives appearing in the unsteady differential equation and in the unsteady shock-jump condition are approximated to within the same order of accuracy in the local calculation. At points on the outer boundary of the local mesh the unsteady potential is given the values interpolated from the cascade mesh solution.

Let $\underset{\sim}{\phi}_i$ be a vector of ϕ values on the ith axial mesh line for the cascade calculation or on the ith radial mesh line for the local calculation. Because: (1) neighbor sets for points on the ith line include only points from the lines i-1, i, and i+1; (2) the difference approximation to the unsteady differential equation involves only neighbor sets centered on the lines i and i-1; (3) first and second-order accurate difference approximations are used in the local calculation to approximate normal (to the shock) derivatives on the upstream and downstream sides of the shock, respectively; and (4) the cascade mesh is periodic; the system of linear algebraic equations which approximates the unsteady boundary value problem on both the cascade and local meshes has the following block-quindiagonal form

$$
\begin{aligned}
C_1\underset{\sim}{\phi}_1 + D_1\underset{\sim}{\phi}_2 &= \underset{\sim}{F}_1 \\
A_i\underset{\sim}{\phi}_{i-2} + B_i\underset{\sim}{\phi}_{i-1} + C_i\underset{\sim}{\phi}_i + D_i\underset{\sim}{\phi}_{i+1} + E_i\underset{\sim}{\phi}_{i+2} &= \underset{\sim}{F}_i \ , \ 2 \leq i \leq I-1 \qquad (41) \\
B_I\underset{\sim}{\phi}_{i-1} + C_I\underset{\sim}{\phi}_I &= F_I
\end{aligned}
$$

where the submatrices A_i, B_i, C_i, D_i, and E_i are sparse being basically scalar tridiagonal. Note that, with the exception of the points on the downstream side of a fitted shock, $A_i \equiv 0$ at subsonic points and $E_i \equiv 0$. With this structure the system of equations (41) can be solved directly and efficiently using Gaussian elimination.

NUMERICAL RESULTS

The foregoing analysis has been applied to cascades of vibrating, sharp-edged, double-circular-arc (DCA) airfoils operating at high subsonic and transonic Mach numbers. The mean location of the zeroth or reference blade surface is defined by

$$y_{\pm}(x) = \mathrm{sgn}(H_{\pm}) \left[|H_{\pm}| - R_{\pm} + \sqrt{R_{\pm}^2 - (x-0.5)^2} \right], \qquad H_{\pm} \neq 0 \tag{42}$$

$$= 0, \qquad H_{\pm} = 0$$

where $0 \leq x \leq 1$, H is the y-coordinate of the surface at midchord, $R = |H|^{-1}(H^2 + 0.25)/2$ is the radius of curvature of the surface, $\mathrm{sgn}(H) = \pm 1$ for $H \gtrless 0$, and the subscripts + or - refer to the upper or lower surfaces of the blade. Mean inlet Mach numbers ($M_{-\infty}<1$) are prescribed and corresponding exit Mach numbers ($M_{\infty}<1$) and inlet ($\Omega_{-\infty}$) and exit (Ω_{∞}) flow angles are determined as part of the steady solution by applying a global mass balance and imposing the requirement that

$$\vec{V} \cdot d\vec{\tau} \Big|_{B_-} = - \vec{V} \cdot d\vec{\tau} \Big|_{B_+}, \qquad x = 0,1 \tag{43}$$

at blade leading (unique incidence condition) and trailing (Kutta condition) edges. For simplicity we will present results only for two DCA configurations: an unstaggered ($\Theta = 0$ deg.) array and a staggered (with $\Theta = 45$ deg.) array each with unit gap/chord ratio ($G = 1$) and consisting of 5 percent thick, flat-bottomed, DCA blades (i.e., $H_+ = 0.05$, $H_- = 0$). In addition, for purposes of comparison, results will also be presented for similar arrays of flat-plate ($H_{\pm} = 0$) airfoils. For the flat-plate cascades the steady Mach number is constant throughout the field, and hence, there is no coupling between the steady and unsteady flows.

Unsteady solutions have been determined on a cascade mesh extending one axial chord upstream and downstream from the blade row. For those cases in which a normal shock emanates from the suction surface of each blade, solutions are also determined on a local mesh extending from 10 to 90 percent of blade chord

along the suction surface of the reference blade and outward from this surface to well beyond the end of the shock. For the unstaggered configurations the cascade mesh consisted of 62 axial lines, 30 of which intersected blade surfaces, and 20 tangential lines. A finer mesh is generally required for the 45 deg. staggered configurations and one consisting of 100 axial lines, 44 of which intersect the blade surfaces, and 30 tangential lines was employed. The local mesh consisted of 61 radial lines and 11 circumferential lines. Variable mesh spacings were used in both the cascade and local calculations with cascade tangential and local circumferential lines concentrated near blade surfaces, cascade axial lines concentrated near blade edges, and local radial lines concentrated near shocks. Harmonic, unsteady, pressure-difference (Δp) distributions, where

$$\Delta p(x) = p_{\beta_-}(\tilde{\tilde{X}}) - p_{\beta_+}(\tilde{\tilde{X}}) = p_{\beta_{1,-}}(\tilde{\tilde{X}}+\tilde{\tilde{G}})e^{-i\sigma} - p_{\beta_{0,+}}(\tilde{\tilde{X}}), \qquad \tilde{\tilde{X}} \text{ on } B \tag{44}$$

the shock displacement at the foot of the shock ($r_n(0)$), and unsteady lift (c_L) and moment (c_M) coefficients will be presented for blades undergoing pure torsional motions (with $\alpha = 1, 0$) about midchord ($X_p, Y_p = 0.5, 0$) at prescribed frequencies (ω) and interblade phase angles (σ). When the imaginary part of the torsional amplitude is set equal to zero, the real and imaginary parts of the response coefficients are in- and out-of-phase, respectively, with the blade displacement. Further, the stability of a single-degree-of-freedom torsional motion is governed by the sign of the out-of-phase component (imaginary part) of the unsteady moment. Thus if $\mathrm{Im}\{c_M\} < 0$ for a pure torsional motion, the airstream tends to suppress the motion, and hence, this motion is stable according to linear theory (Ref. 24).

Steady Mach Number Distributions

Full potential steady flows have been determined on similar but coarser cascade and local meshes using the finite-area numerical approximation developed by Caspar, Hobbs and Davis for subsonic cascade flow (Ref. 25) and subsequently extended by Caspar for transonic flow (Ref. 26). It should be noted that with the procedure of Refs. 25 and 26, the steady differential equation is solved in conservative form and shocks are captured. It would be preferable to use a steady solution with a fitted shock for the present application. However, it appears that steady information in the vicinity of a shock can be determined with sufficient accuracy, using the methods of Refs. 25 and 26, to define the mean shock location and to permit the imposition of shock-jump conditions in the present unsteady calculation.

Predicted steady, surface-Mach-number distributions for the example DCA configurations are shown in Figs. 3 and 4. For the unstaggered cascade (Fig. 3) prescribed inlet (and calculated exit) Mach numbers of 0.70, 0.72, 0.74 and 0.76 are considered. Corresponding inlet and exit flow angles vary from $\Omega_{\mp\infty}$ = ±4.3 deg for $M_{-\infty}$ = 0.70 to $\Omega_{\mp\infty}$ = ±4.65 deg for $M_{-\infty}$ = 0.76. At the three lower Mach numbers, $M_{-\infty}$ = 0.7, 0.72 and 0.74, the calculated steady flows are continuous with peak Mach numbers of 0.91, 0.95 and 1.01, respectively, occurring at midchord on the blade suction surface. For $M_{-\infty}$ = 0.74 the supersonic region extends from 43% to 57% of blade chord along the suction surface. At the highest inlet Mach number, $M_{-\infty}$ = 0.76, a shock emanates from the blade suction surface at 64.5 percent of chord downstream from the leading edge. The Mach numbers at the foot of the shock are 1.157 upstream and 0.935 downstream, and the supersonic region extends from x = 0.32 to x = 0.645 along the blade suction surface. For the 45 deg. staggered DCA cascade (Fig. 4) the prescribed inlet Mach numbers are 0.7, 0.8, and 0.9 and the calculated exit Mach numbers are 0.57, 0.62 and 0.65, respectively. The corresponding inlet flow angles are 49.2 deg, 49.4 deg, and 49.6 deg, respectively, and in each case the exit flow angle is 43.0 deg. The steady flows at $M_{-\infty}$ = 0.7 and $M_{-\infty}$ = 0.8 are entirely subsonic with peak suction-surface Mach numbers of 0.804 and 0.941 occurring at 38.5 and 36.7 percent of blade chord, respectively, downstream from the leading edge. The steady flow is transonic for $M_{-\infty}$ = 0.9 with the supersonic region extending from 18.5 to 52.5 percent of blade chord along the suction surface and terminating at a shock. The Mach numbers at the foot of the shock are 1.193 on the upstream or supersonic side and 0.871 on the downstream or subsonic side.

Response Predictions for Unstaggered Cascades

Although unstaggered configurations are of limited practical interest, they are the simplest and therefore perhaps the most useful ones for the initial evaluation of complicated aerodynamic and numerical analyses. We therefore present rather detailed results for unstaggered arrays of DCA and flat plate airfoils undergoing out-of-phase (σ = 180 deg.) and in-phase (σ = 0 deg.) torsional vibrations at low (ω = 0.1) through moderate (up to ω = 1.0) frequencies, and at the inlet Mach numbers indicated in Fig. 3. Particular emphasis is placed on unsteady response predictions for the discontinuous mean flow at $M_{-\infty}$ = 0.76, and the highest frequency considered (i.e., ω = 1.0) is the most representative one for turbomachinery flutter applications.

As a first example we consider the aerodynamic response to low-frequency, out-of-phase, torsional vibrations for the DCA cascade in Fig. 5 and for the flat-plate cascade in Fig. 6. These results have been determined by performing unsteady calculations on the cascade mesh only, and hence, unsteady shock phenomena have been captured in the numerical solution for the DCA cascade operating at $M_{-\infty} = 0.76$. The well-defined shock depicted in Fig. 5 results from using one-sided difference approximations to evaluate the surface pressures at the mesh points just upstream and downstream of the shock and extrapolating the calculated surface pressures to the known mean shock location. A comparison of the low-frequency predictions for the unstaggered DCA and flat plate cascades reveals (as expected) the substantial effect of the steady flow gradients produced by blade thickness and camber on the unsteady response to low-frequency blade motions, particularly at transonic Mach numbers.

The results shown in Figs. 7 through 10 are presented to illustrate several features of the unsteady numerical solution procedure for discontinuous transonic flows. Cascade and combined (i.e., cascade and local) mesh response predictions are depicted in Figs. 7 and 8 for the unstaggered DCA cascade operating at an inlet Mach number of 0.76. These results have been determined by shock capture; i.e., the unsteady differential equation has been solved across the shock in the cascade calculation, and the continuity condition, $[\![\phi]\!] = 0$, has been applied on the downstream shock mesh line in the local calculation. The two solutions are in very close agreement, except in the vicinity of the shock. In particular, the sharp rise in the imaginary component of the unsteady pressure difference for $\omega = 1.0$ just upstream of the shock (Fig. 7) is removed by the local solution (Fig. 8). The overall agreement between the cascade and combined mesh solutions for unstaggered cascades of relatively thin blades is not too suprising since the cascade axial lines are nearly normal to the mean flow direction. The differences between the cascade and the local solutions near the shock can be attributed to local radial lines being more closely aligned with the mean shock locus than cascade axial lines and to the greater mesh density used in the local calculation.

Unsteady velocity potential distributions on the suction surface of the reference blade are shown in Figs. 9 and 10 to partially illustrate the effect of fitting shocks into the unsteady solution. The results depicted in Fig. 9 have been determined by imposing the shock capture or continuity condition ($[\![\phi]\!] = 0$) on the downstream shock mesh line in the local calculation, while those depicted in Fig. 10 have been determined by fitting the shock (i.e., imposing the shock-jump condition of Eq. 23). The continuous and discontinuous surface potential distributions are identical upstream, but they differ substantially downstream of the mean shock location. Recall that the jump in the unsteady potential across the shock is proportional to the shock displacement (c.f. Eq. (20)). For the steady flow at $M_{-\infty} = 0.76$ the results shown in Fig. 10 indicate that the

complex shock displacement along the blade surface leads the blade rotational displacement, α, by a phase angle which is greater than 90 deg for $\omega = 0.1$ and $\omega = 0.5$, and slightly less than 90 deg for $\omega = 1.0$. Hence, the instantaneous location of the shock foot will generally be upstream of its mean position at the two lower frequencies and downstream of its mean position at the highest frequency when the blade is displaced nose-down from its mean position.

The effect of frequency on the response to out-of-phase torsional vibrations of the unstaggered DCA and flat plate cascades is illustrated in Figs. 11 and 12. The DCA results (Fig. 11) include the effects of shock motion. A comparison of these results with the continuous, shock-capture solutions of Fig. 8 reveals that the shock displacement has a substantial impact on the harmonic component of the unsteady surface pressure downstream of the shock. In particular, the out-of-phase (imaginary) moments corresponding to the pressure difference distributions in Fig. 11b are substantially less than those corresponding to the pressure difference distributions shown in Fig. 8. This stabilizing effect is partially compensated for by the unsteady moment due to the concentrated shock load. For the DCA cascade operating at $M_{-\infty} = 0.76$ there is a steady pressure jump, $[\![P]\!]$, on the blade suction surface of 0.509. Since the shock mean position is downstream of the torsional axis ($\vec{R}_p \cdot \vec{\tau}_B = -0.142$) and $\mathrm{Im}\{r_n(0)\}$ is positive for the motions considered in Fig. 11, the anharmonic component of the unsteady pressure, produced by the shock motion, provides a positive or counterclockwise out-of-phase moment (c.f. Eq. 35) which tends to destabilize the blade motion. However, at least for the present examples, the net effect of shock motion is a stabilizing one. A comparison of the DCA results (Fig. 11) with those for the flat plate cascade (Fig. 12) reveals the dramatic influence of blade geometry on the low through moderate frequency unsteady response at high subsonic inlet Mach number. Note that the torsional stability margin increases much more substantially with increasing frequency for the flat plate than for the DCA configuration.

The effect of frequency on the response to in-phase ($\sigma = 0$ deg.) torsional vibrations of the unstaggered DCA and flat plate cascades is illustrated in Figs. 13 and 14, respectively. For subsonic inlet and exit conditions in-phase blade vibrations are superresonant; i.e., acoustic energy persists far-upstream and/or downstream of the blade row, whereas the out-of-phase motions considered above are subresonant. The magnitudes of the complex response coefficients for the in-phase torsional vibrations of Figs. 13 and 14 are much smaller than those for the out-of-phase torsional vibrations of Figs. 11 and 12. As a result, the stability margin for each in-phase torsional vibration considered is significantly lower than it is for the corresponding out-of-phase torsional vibration at the same frequency. For the DCA configuration, the out-of-phase component of the shock displacement; i.e., $\mathrm{Im}\{r_n(0)\}$, is negative for each of the five frequencies considered. Thus, in each case, the anharmonic component of the unsteady pressure tends to amplify the blade motion. However, due to its influence on the harmonic pressure response, the net effect of the shock motion is a destabilizing one for each of the in-phase vibrations considered in Fig. 13.

The effect of Mach number on the unsteady response to unit-frequency, out-of-phase, and in-phase torsional vibrations of unstaggered DCA and flat-plate cascades is illustrated in Figs. 15 through 18. A comparison of these DCA and flat-plate results again reveals the substantial impact of mean flow gradients on the unsteady response at transonic Mach numbers. Recall that for $M_{-\infty} = 0.74$ the calculated steady flow is continuous with a local supersonic region occurring adjacent to the suction surface of each blade. There is some question as to whether a continuous linear perturbation of a continuous, transonic, zeroth-order or steady flow is meaningful, or whether a shock must form as a result of the small excitation. Indeed, the present authors have determined spurious unsteady solutions which suggest the formation of a shock for different sets of continuous, steady, transonic, input data (e.g., see Fig. 8 of Ref. 27). Since current steady codes predict continuous transonic phenomena over a range of inlet conditions, this question is an important one with regard to the range application of a linear unsteady analysis and deserves future research consideration. The unsteady pressure difference distributions, shown in Fig. 15 and 17, corresponding to the continuous transonic mean flow at $M_{-\infty} = 0.74$ do contain surprisingly large variations with distance along the blade chord over an interval in which the local steady Mach number is close to one. However, the distributions for $M_{-\infty} = 0.7$, 0.72 and 0.74 follow reasonable trends with increasing inlet Mach number.

Response Predictions for Staggered Cascades

The discussion on the unsteady response behavior of staggered (at $\Theta = 45$ deg.) DCA and flat plate cascades will parallel that just given for the unstaggered configurations. Thus numerical results will be presented for blades undergoing out-of-phase and in-phase torsional vibrations, about an axis at midchord, at low ($\omega = 0.1$) through moderate (up to $\omega = 1.0$) frequencies. Particular emphasis will be placed on the resolution of unsteady transonic phenomena. Only three inlet Mach numbers (i.e., $M_{-\infty} = 0.7$, 0.8 and 0.9) will be considered. The steady flow through the DCA cascade is everywhere subsonic at the two lower inlet Mach numbers and transonic with a shock discontinuity emanating from the suction surface of each blade for $M_{-\infty} = 0.9$. The inlet and exit Mach numbers differ substantially for the staggered DCA configuration, and this difference effects the overall character of the unsteady flow. For example at $M_{-\infty} = 0.9$, the unit-frequency, out-of-phase, torsional vibrations of both the staggered DCA ($M_\infty = 0.65$) and flat plate ($M_\infty = 0.9$) cascades are super-resonant. However, acoustic energy only propagates in the far upstream direction for the DCA array, because the waves travelling downstream at the lower exit Mach number attenuate with increasing distance from the blade row.

The results shown in Figs. 19 through 22 are analogous to those given in Figs. 7 through 10, and are provided to illustrate the cascade and local mesh solutions as well as the effect of imposing the shock-jump condition, Eq. (23), in the local unsteady calculation. Cascade and combined mesh response predictions for the staggered DCA configuration operating at an inlet Mach number of 0.9 are shown in Figs. 19 and 20, respectively. These results have been determined by shock capture and they clearly illustrate the need for the local unsteady analysis to resolve the flow through a staggered transonic cascade. The unsteady pressure difference distributions determined from the cascade mesh solution (Fig. 19) are unsatisfactory, especially in the vicinity of the normal shock. In particular, the cascade mesh solutions suggest that local maxima of minima will appear in the unsteady pressure difference distributions upstream of the shock. The errors associated with the cascade calculation occur because this mesh is highly skewed for a cascade with a 45 deg. stagger angle and, as a result, a number of axial mesh lines cross the normal shock. The combined mesh solutions shown in Fig. 20 indicate the significant improvement in the resolution of the unsteady flow near the shock that can be achieved with the local mesh calculation.

The unsteady velocity potential distributions on the suction surface of the reference blade of the transonic DCA cascade are shown in Figs. 21 and 22. The results in Fig. 21 have been determined by shock capture and those in Fig. 22 have been determined by shock fit. As in the case of the unstaggered DCA cascade (Figs. 9 and 10), the continuous and discontinuous surface potential distributions are identical upstream of the mean shock location, but they differ substantially just downstream of the shock discontinuity. For the staggered configuration the complex shock displacement along the blade surface, $r_n(0)$, leads the blade rotational displacement, α, by an angle greater than 90 deg. for $\omega = 0.1$ and less than 90 deg for $\omega = 0.5$ and $\omega = 1.0$. Hence, the instantaneous location of the shock foot will generally be upstream of its mean position at $\omega = 0.1$ and downstream of its mean position at $\omega = 0.5$ and $\omega = 1.0$ when the blade is displaced nose-down from its mean position.

The effect of frequency on the response to out-of-phase torsional blade vibrations for the staggered DCA and flat-plate cascades is illustrated in Figs. 23 and 24. These motions are subresonant at the lower frequencies, $\omega = 0.1$ and $\omega = 0.25$, and super- resonant at $\omega = 0.5$, 0.75 and 1.0. The results for the DCA cascade have been determined by shock fitting and, as in the previous examples, there are significant differences between the unsteady responses to the DCA (Fig. 23) and flat plate (Fig. 24) blade motions. A comparison of the DCA results in Fig. 23 with the continuous solutions shown in Fig. 20 again reveals the substantial impact of shock motion on the harmonic pressure differences downstream of the shock mean position, particularly at low reduced frequency. For the examples considered here, one effect of including the shock-jump condition in the local

unsteady calculation is a decrease in the imaginary part of the unsteady pressure difference downstream of the shock, and hence, a decrease in the out-of-phase moment; i.e., stability enhancement. However, the anharmonic component of the unsteady pressure produced by the shock motion partially compensates for this. The steady pressure jump across the foot of the shock is positive ($[\![p]\!]=0.593$), the shock mean position is slightly downstream of the torsional axis ($\hat{R}_p \cdot \hat{\tau}_B = -0.025$), and the out-of-phase component of the shock displacement is positive ($\mathrm{Im}\{r_n(0)\} > 0$). Therefore the anharmonic component of the unsteady pressure produces a small but positive or counterclockwise imaginary moment (c.f. Eq. (35)) which tends to amplify the blade motion. For the motions considered in Figs. 20 and 23, the net effect of including the shock motion in each unsteady solution is a stabilizing one. The moment predictions for the staggered DCA configuration indicate that the stability of out-of-phase torsional vibrations will be enhanced with increasing blade-vibration frequency unless the frequency increases through a resonance condition, in which case, there will be a significant reduction in the stability margin. The limited results presented in Fig. 24 for the flat plate cascade indicate a reduction in stability margin with increasing frequency.

The effect of frequency on the response to the in-phase, torsional, blade vibrations for the staggered DCA and flat-plate cascades is illustrated in Figs. 25 and 26. The motions considered are superresonant with acoustic energy propagating away from the blade row in both the far-upstream and far-downstream directions, and the amplitudes of the complex response parameters are generally smaller than those for out-of-phase torsional vibrations at the same frequency. For the staggered DCA cascade operating at $M_{-\infty} = 0.9$, the complex shock displacement, $r_n(0)$, lags the blade rotational displacement for $\omega = 0.1$, 0.25 and 0.5 and leads the rotational displacement for $\omega = 0.75$ and 1.0. Thus the out-of-phase component of the shock displacement, $\mathrm{Im}\{r_n(0)\}$, is negative at the three lower frequencies and positive at the two higher frequencies. Since the mean shock location is slightly aft of midchord, the concentrated load due to shock motion produces a small stabilizing moment for $\omega = 0.1$, 0.25 and 0.5 and a small destabilizing moment for $\omega = 0.75$ and 1.0. The stability margin for in-phase torsional vibrations of the DCA cascade tends to increase with increasing frequency (Fig. 25b). This is not the case for the flat-plate cascade (Fig. 26) where the moment resisting the blade motion ($-\mathrm{Im}\{c_M\}$) is greater at $\omega = 0.5$ than it is at $\omega = 1.0$.

The effect of Mach number on the unit-frequency response to out-of-phase and in-phase torsional vibrations of DCA and flat-plate cascades is illustrated in Figs. 27 through 30. Inlet Mach numbers of 0.7, 0.8 and 0.9 are considered. Recall that at $M_{-\infty} = 0.7$ and $M_{-\infty} = 0.8$ the flow through the DCA cascade is

everywhere subsonic, while at $M_{\infty} = 0.9$ it is transonic with a shock emanating on the suction surface of each blade. The out-of-phase motions of the DCA cascade are subresonant at $M_{\infty} = 0.7$ and superresonant at the two higher Mach numbers, while the out-of-phase motions of the flat-plate cascade are subresonant at $M_{\infty} = 0.7$ and $M_{\infty} = 0.8$ and superresonant at $M_{\infty} = 0.9$. For each cascade the out-of-phase motion at $M_{\infty} = 0.8$ is close to a resonance condition, and as a result accurate response predictions can be difficult to achieve. The in-phase motions of both the DCA and flat-plate cascades are superresonant. The unsteady pressure difference distributions for the out-of-phase vibrations of the DCA (Fig. 27) and flat-plate (Fig. 28) cascades are very similar for $M_{\infty} = 0.7$, but differ substantially for $M_{\infty} = 0.8$ and $M_{\infty} = 0.9$. The differences at $M_{\infty} = 0.8$ are primarily due to the different character of the unsteady motions (i.e., superresonant or subresonant) and to the near resonance operation of each cascade. At the highest Mach number the differences in the DCA and flat-plate unsteady pressure difference distributions are due to the transonic and shock motion phenomena associated with the DCA configuration. For the three inlet Mach numbers considered the stability margin for the out-of-phase torsional vibrations of the DCA cascade decreases with increasing inlet Mach number, while the stability margin for the flat plate cascade is lowest at $M_{\infty} = 0.8$. The unsteady pressure difference distributions for the in-phase vibrations of the DCA and flat plate cascades are again similar for $M_{\infty} = 0.7$, differ somewhat for $M_{\infty} = 0.8$ and differ substantially for $M_{\infty} = 0.9$. The differences at $M_{\infty} = 0.8$ can be attributed to the large mean Mach number variations which occur along the suction surface and upstream of midchord of each DCA blade, while those at $M_{\infty} = 0.9$ are due to the transonic phenomena occurring in the DCA cascade. The in-phase torsional stability margin for the DCA cascade is smaller at $M_{\infty} = 0.7$ and $M_{\infty} = 0.8$ but larger at $M_{\infty} = 0.9$ than it is for the flat-plate cascade.

CONCLUDING REMARKS

An unsteady aerodynamic analysis has been developed for turbomachinery aeroelastic applications. Here, the unsteady flow is produced by the small-amplitude (infinitesimal), harmonic vibrations of the blades of a two-dimensional cascade operating in an inviscid transonic flow with embedded shocks. The unsteady potential is determined as the solution of a linear, variable-coefficient, boundary value problem in which surface conditions are imposed at the mean positions of blade, wake, and shock surfaces, and the variable coefficients depend on the underlying full-potential, mean or steady flow. The local character of the unsteady differential equation (i.e., elliptic or hyperbolic) depends on the local steady Mach number, and the unsteady potential is discontinuous at the mean shock positions. Shock displacement and hence, the concentrated loads produced by this displacement are proportional to the discontinuity in the unsteady potential. The analysis applies at the reduced frequencies of interest for turbomachinery flutter applications (i.e., $\omega \sim \mathcal{O}(1)$) and includes the effects of real blade geometry and finite mean pressure rise (or fall) across the blade row as well as the effects of transonic Mach numbers and shock motions within the framework of a linear frequency-domain formulation. It therefore represents an important advance over the classical linearized analyses currently employed in turbomachinery aeroelastic studies, and over the time-linearized, unsteady, transonic analyses that have been developed for fixed-wing applications.

The numerical solutions, presented in this report, have been determined using an implicit, least-squares, finite-difference approximation which has been modified to include transonic differencing strategies and options for fitting or capturing unsteady shock phenomena. Unsteady solutions have been determined on cascade and local grids. The local analysis is required for the accurate resolution of unsteady transonic flows through staggered cascades as well as for the prediction of shock motion phenomena. Examples have been provided to establish confidence in the unsteady transonic analysis, especially at high reduced frequency, and to illustrate the strong impact of nonuniform steady flow on the unsteady response at high subsonic and transonic Mach numbers. Particular emphasis has been placed on evaluating the effect of shock motion. Such motions must be included to achieve a uniformly valid first-order solution; however, at least for the examples considered here, they produced harmonic and anharmonic unsteady surface pressure responses which gave opposing contributions to the global unsteady airloads. Thus the solutions determined by shock capture provided reasonable estimates of the unsteady lift and moment. In future work it is recommended that detailed parametric studies be conducted to provide a more complete understanding of the effects of blade geometry and loading, blade-vibration mode and frequency, and shock motion phenomena on the unsteady aerodynamic response, and hence, on the aerodynamic stability of cascades operating at transonic Mach numbers.

Efforts should also be undertaken to extend the range of application of the present analysis and to improve the accuracy of the unsteady response predictions. In particular, the local calculation should be applied on a mesh which wraps around the leading edge and extends along the lower surface of the reference blade so that mean incidence effects and shocks emanating from both the suction and pressure surfaces of each blade can be simultaneously analyzed. In addition, mean-flow equi-potential and streamlines should be used as local mesh lines in the vicinity of a shock to permit a more accurate resolution of unsteady shock phenomena, and an iterative procedure should be used in matching the cascade and local solutions. The latter is particularly important for transonic applications because essentially different boundary value problems are solved in the cascade and local analyses. The unsteady differential equation is solved across the shock in the former, and shock-jump conditions are imposed in the latter. This situation can lead to errors at the cascade-local interface. Finally, since steady transonic cascade analyses tend to predict continuous transonic flows over a range of inlet conditions, the impact of continuous transonic input data on unsteady perturbation solutions must be carefully determined and evaluated.

REFERENCES

1. Tijdeman, H. and R. Seebass: Transonic Flow Past Oscillating Airfoils. Annual Review of Fluid Mechanics, Vol. 12, 1980, pp. 181-222.

2. Whitehead, D. S.: Unsteady Aerodynamics in Turbomachinery. Special Course on Unsteady Aerodynamics, AGARD Report No. 679, June 1980.

3. Ehlers, F. E. and W. H. Weatherill: A Harmonic Analysis Method for Unsteady Transonic Flow and Its Application to the Flutter of Airfoils. NASA CR 3537, prepared under Contract NAS1-15957 for Langley Research Center, May 1982.

4. Fung, K. Y., N. J. Yu, and R. Seebass: Small Unsteady Perturbations in Transonic Flows. AIAA Journal, Vol. 16, No. 8, pp. 815-822, August 1978.

5. Verdon, J. M. and J. R. Caspar: Subsonic Flow Past an Oscillating Cascade with Finite Mean Flow Deflection. AIAA Journal, Vol. 18, No. 5, May 1980, pp. 540-548.

6. Atassi, H. and T. J. Akai: Effect of Blade Loading and Thickness on the Aerodynamics of Oscillating Cascades. Paper No. 78-227, AIAA 16th Aerospace Sciences Meeting, Huntsville, AL, January 16-18, 1978.

7. Whitehead, D. S. and R. J. Grant: Force and Moment Coefficients for High Deflection Cascades. Aeroelasticity in Turbomachines, P. Suter (editor), Proceedings of the Second International Symposium held in Lausanne, Switzerland, September 8-12, 1980, Juris-Verlag Zurich, 1981, pp. 85-127.

8. Caruthers, J. E.: Aerodynamic Analysis of Cascaded Airfoils in Unsteady Rotational Flow. Aeroelasticity in Turbomachines, P. Suter (editor), Proceedings of the Second International Symposium held in Lausanne, Switzerland, September 8-12, 1980, Juris-Verlag Zurich, 1981, pp. 31-64.

9. McNally, W. D. and P. M. Sockol: Computational Methods for Internal Flows with Emphasis on Turbomachinery. NASA Technical Memorandum 82764, November 1981.

10. Caspar, J. R. and J. M. Verdon: Numerical Treatment of Unsteady Subsonic Flow Past an Oscillating Cascade. AIAA Journal, Vol. 19, No. 12, December 1981, pp. 1531-1539.

11. Verdon, J. M. and J. R. Caspar: Development of an Unsteady Aerodynamic Analysis for Finite-Deflection Subsonic Cascades. NASA CR 3455, prepared under Contract NAS3-21981 for Lewis Research Center, September 1981.

REFERENCES (Cont'd)

12. Verdon, J. M. and J. R. Caspar: Development of a Linear Unsteady Aerodynamic Analysis for Finite-Deflection Subsonic Cascades. AIAA Journal, Vol. 20, No. 9, September 1982, pp. 1259-1267.

13. Carta, F. O.: Unsteady Aerodynamics and Gapwise Periodicity of Oscillating Cascaded Airfoils. Transactions of the ASME, Journal of Engineering for Power, Series A, Vol. 105, No. 3, July 1983, pp. 565-574.

14. Williams, M. H.: Linearization of Unsteady Transonic Flows Containing Shocks. AIAA Journal, Vol. 17, No. 4, April 1979, pp. 394-397.

15. Hounjet, M. H. L.: Transonic Panel Method to Determine Loads on Oscillating Airfoils with Shocks. AIAA Journal, Vol. 19, No. 5, May 1981, pp. 559-566.

16. Jameson, A.: Iterative Solution of Transonic Flows Over Airfoils and Wings Including Flows at Mach 1. Communications on Pure and Applied Mathematics, Vol. 27, 1974, pp. 283-309.

17. Murman, E. H. and J. D. Cole: Calculation of Plane Steady Transonic Flows. AIAA Journal, Vol. 9, No. 1, pp. 114-121, January 1971.

18. Murman, E. H.: Analysis of Embedded Shock Waves Calculated by Relaxation Methods. AIAA Journal, Vol. 12, No. 5, May 1974, pp. 626-633.

19. Aris, A.: Vectors, Tensors and the Basic Equations of Fluid Mechanics. Prentice-Hall, Inc., Englewood Cliffs, New Jersey, 1962, p. 122.

20. Whitham, G. B.: Linear and Nonlinear Waves. John Wiley and Sons, New York, 1974, pp. 172-176.

21. Verdon, J. M., J. J. Adamczyk and J. R. Caspar: Subsonic Flow Past an Oscillating Cascade with Steady Blade Loading - Basic Formulation. Unsteady Aerodynamics, R. B. Kinney (editor), Proceedings of a Symposium held at the University of Arizona, Tuscon, AZ, March 1975, Vol. II, pp. 827-851.

22. Carta, F. O.: Coupled Blade-Disk-Shroud Flutter Instabilities in Turbojet Engine Rotors. Transactions of the ASME, Journal of Engineering for Power, Series A, Vol. 89, No. 3, July 1967, pp. 419-427.

23. Tijdeman, H.: Investigations of the Transonic Flow Around Oscillating Airfoils. NLR TR 77090-U, National Aerospace Laboratory (Amsterdam), December 1977.

24. Fung, Y. C.: An Introduction to the Theory of Aeroelasticity. John Wiley and Sons, Inc., New York, 1955, pp. 166-168.

25. Caspar, J. R., D. E. Hobbs and R. L. Davis: Calculation of Two-Dimensional Potential Cascade Flow Using Finite Area Methods. AIAA Journal, Vol. 18, January 1980, pp. 103-109.

26. Caspar, J. R.: Unconditionally Stable Calculation of Transonic Potential Flow through Cascades Using an Adaptive Mesh for Shock Capture. Transactions of the ASME, Journal of Engineering for Power, Series A, Vol. 105, No. 3, July 1983, pp. 504-513.

27. Verdon, J. M. and J. R. Caspar: Development of a Linear Aerodynamic Analysis for Unsteady Transonic Cascades. NASA CR 168038, prepared under Contract NAS3-21981 for Lewis Research Center, October 1982.

LIST OF SYMBOLS

NOTE: All quantities are dimensionless. Lengths have been scaled with respect to blade chord, time with respect to the ratio of blade chord to upstream free-stream speed, and density and pressure with respect to the upstream free-stream density and dynamic pressure, respectively.

Latin

$A_i, B_i, C_i, D_i, E_i, F_i$	Submatrices of block-quindiagonal system of algebraic equations, Eq. (41)
$\hat{A}$	Speed of sound, Eq. (2)
A	Zeroth-order or steady speed of sound, Eq. (14)
$ae^{i\omega t}$	Harmonic component of unsteady (first-order) speed of sound, Eq. (14)
β	Instantaneous position of blade surface
B	Mean position of blade surface, Fig. 1
$\hat{\vec{C}}_F, \hat{C}_M$	Aerodynamic force, moment coefficient, Eqs. (32) and (33)
$\hat{C}_F$	Zeroth-order or steady force coefficient, Eq. (34)
c_F, c_M	First-order or unsteady force, moment coefficient, Eqs. (34) and (35)
c_L	Unsteady lift coefficient
D_S/D	Material or convective derivative operator relative to the zeroth-order or steady flow, Eq. (15)
$d\vec{\tau}$	Differential vector tangent to mean blade surface, Eq. (32)
$\vec{G}$	Cascade gap vector, Fig. 1
H	y-coordinate of reference DCA blade at midchord, Eq. (42)

LIST OF SYMBOLS (Cont'd)

Latin

$H(\ )$	Unit-step function, Eq. (28)
$\vec{h}$	Translational displacement vector, Eq. (31)
I	Number of axial or radial mesh lines, Eq. (41)
$\mathrm{Im}\{\ \}$	Imaginary part of { }
i	Imaginary unit
$\mathcal{L}$	Linear differential operator, Eq. (37)
L	Linear difference operator, Eq. (39)
M	Zeroth-order or steady Mach number, Eq. (2); number of neighbor points
m	Blade number index (m = 0 denotes the reference blade)
$\vec{n}$	Unit normal vector directed outward from blade surfaces, upward at wakes, and downstream at shocks
$\mathcal{O}$	Order symbol
$\hat{P}$	Pressure, Eq. (2)
P	Zeroth-order or steady pressure, Eq. (14)
$pe^{i\omega t}$	Harmonic component of unsteady (first-order) pressure, Eq. (14)
$P_{\mathcal{SH}}$	Anharmonic component of unsteady pressure, Eq. (27)
Q_m	Mesh point, m = 0 refers to calculation point, m = 1, ..., M refers to neighboring mesh points
$Q(\tau,t)$	Shock transfer function, Eq. (27)

LIST OF SYMBOLS (Cont'd)

Latin

q^0	Multiplicative constant, Eq. (36)
$\vec{\mathcal{R}}$	Blade, Eq. (4), wake, or shock, Eq. (6), displacement vector
R	Radius of curvature of DCA blade surface, Eq. (42)
$\vec{R}_p, \hat{\vec{R}}_p$	Position vectors extending from the mean, instantaneous position of the reference blade axis of rotation to points on the mean, instantaneous position of the reference blade surface, Eqs. (31) and (33)
Re { }	Real part of { }
$\vec{r}$	Blade displacement-amplitude vector, Eq. (11)
r_n	Amplitude of shock displacement normal to the mean shock position, Eq. (20)
S,N	Local canonical Cartesian coordinates with S-axis directed along steady streamline, Eq. (38)
$\mathcal{Sh}$	Instantaneous position of shock surface
Sh	Mean position of shock surface, Fig. 1
t	Time
V	Zeroth-order or steady velocity, Eq. (12a)
$\mathcal{W}$	Instantaneous position of wake surface
W	Mean position of wake surface, Fig. 1
$\vec{X}$	Position vector in space-fixed x,y-coordinate frame, Eq. (8)
X_p, Y_p	x,y-Coordinates of mean position or reference blade pitching (torsional) axis

Latin

x,y	Space-fixed Cartesian coordinates with x-axis coinciding with mean position of the reference blade chord line and directed downstream, Fig. 1

Greek

$\vec{\alpha}$	Rotational displacement vector, Eq. (31)
β_m	Difference coefficient, Eq. (36)
γ	Specific heat ratio
Δp	Harmonic unsteady pressure difference coefficient, Eq. (44)
ε	Small parameter, Eq. (8)
Θ	Cascade stagger angle, Fig. 1
ξ,η	Space-fixed Cartesian coordinates with the ξ-axis lying along the cascade axis and directed downstream, Fig. 1
$\xi_{\mp}$	ξ-coordinate of far upstream, downstream boundaries
$\hat{\rho}$	Fluid density, Eq. (2)
$\bar{\rho}$	Zeroth-order or steady density, Eq. (14)
$\rho e^{i\omega t}$	Harmonic component of unsteady density, Eq. (14)
σ	Interblade phase angle, positive when motion of the (m+1)th blade leads the motion of the mth blade, Eq. (11)
$\vec{\tau}$	Unit vector tangent to blade, wake, or shock surface and directed such that $\vec{n} \times \vec{\tau} = \vec{e}_z$
$\hat{\Phi}$	Velocity potential, Eq. (1)
Φ	Zeroth-order or steady velocity potential
$\phi e^{i\omega t}$	Harmonic component of unsteady velocity potential, Eq. (16)

LIST OF SYMBOLS (Cont'd)

Greek

$\Omega_{\mp\infty}$	Inlet, exit flow angle, Fig. 1
ω	Frequency (circular) of blade motion, Eq. (11)

Subscripts

$\mathcal{B}$	Instantaneous position of blade surface, Eq. (24)
B	Mean position of blade surface, Eq. (24)
i,j	Axial, tangential or radial, circumferential mesh line index
m	Blade number; neighboring mesh point
$\mathcal{S}$	Instantaneous position of blade, wake or shock surface, Eq. (10)
S	Mean position of blade, wake, or shock surface, Eq. (10)
$\mathcal{S}h$	Instantaneous shock location, Eq. (27)
Sh	Mean shock location, Eq. (27)
S,N, , , ,n	Vector component or partial derivative in indicated direction
t	Local time derivative
0	Calculation point
0,1	Zeroth-, first-order quantity, Eq. (8)
+, -	Upper, lower surface of blade or wake; downstream, upstream of blade row
$\mp\infty$	Far upstream, downstream of blade row

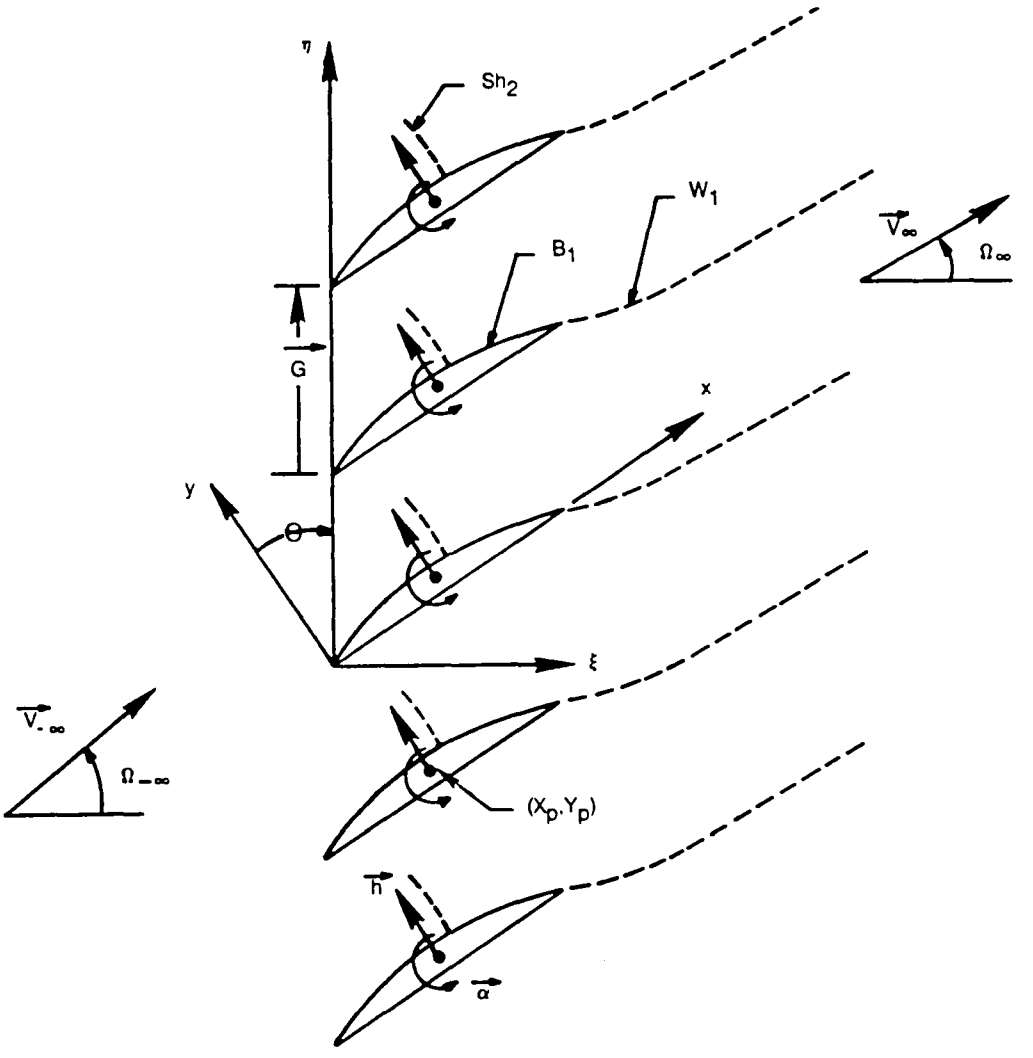

Fig. 1 Two-Dimensional Oscillating Transonic Cascade with Finite Mean-Flow Deflection

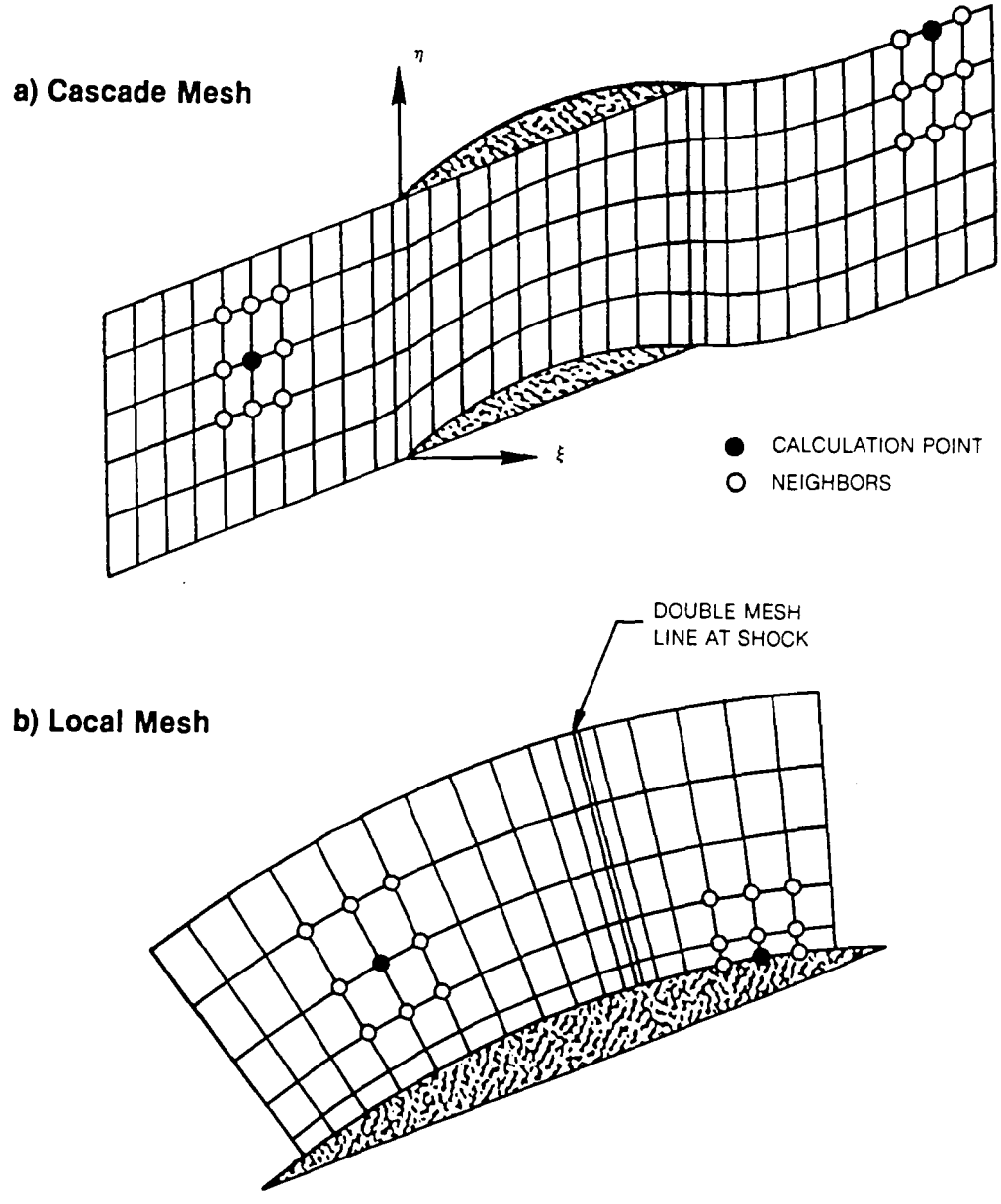

Fig. 2 Calculation Meshes for Unsteady Transonic Cascade Flow

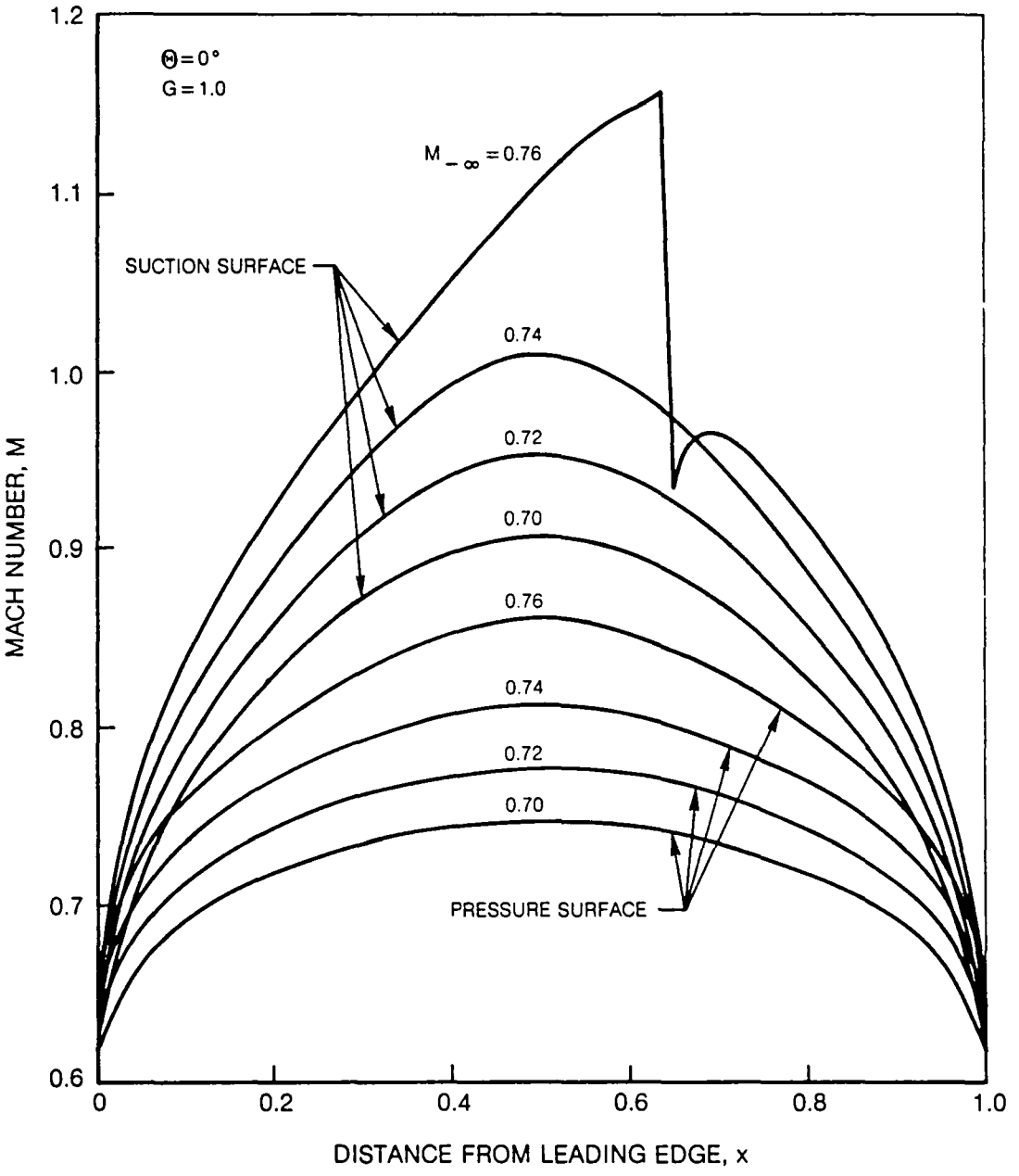

Fig. 3 Surface Mach Number Distributions for an Unstaggered DCA Cascade

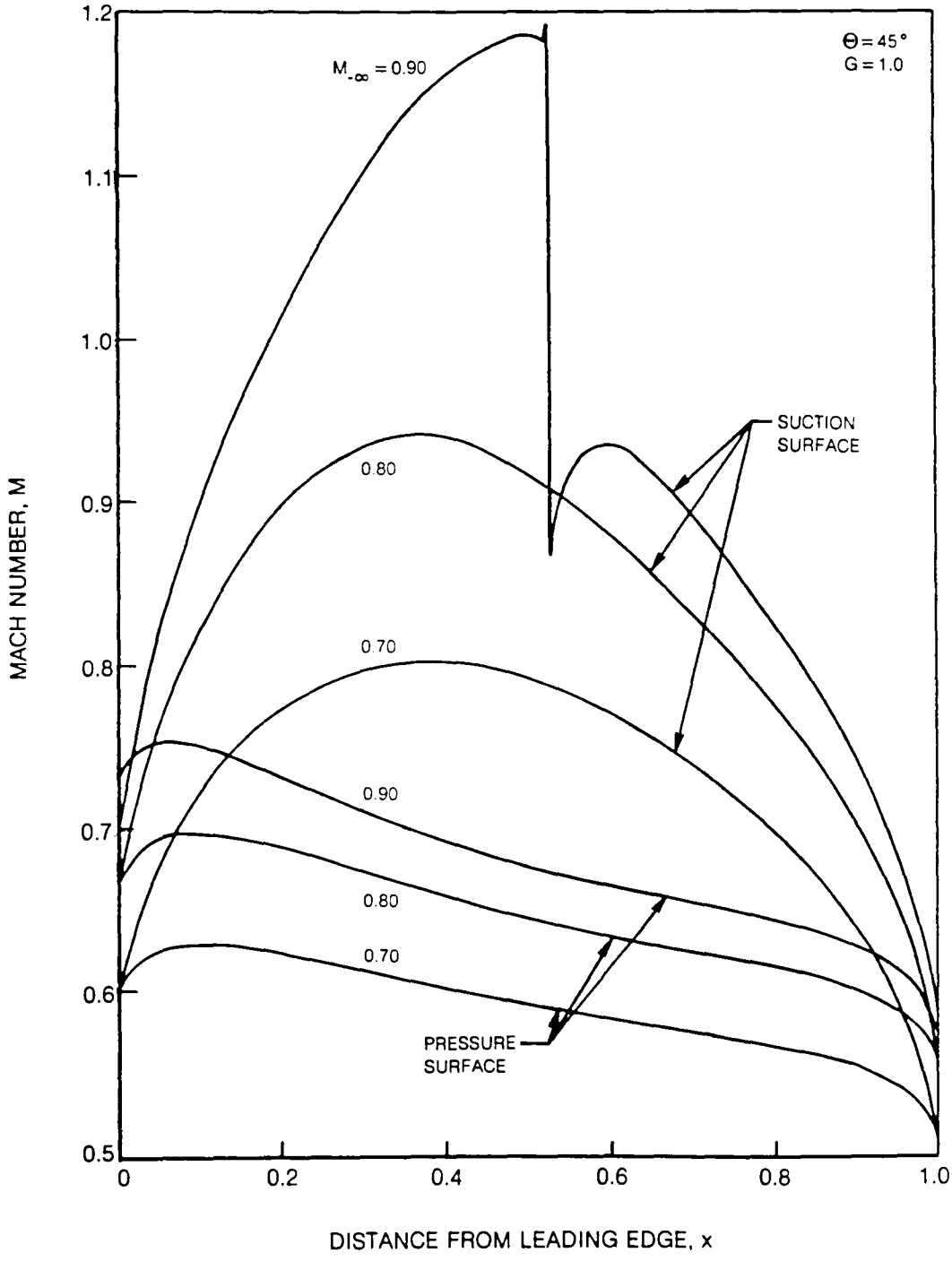

Fig. 4 Surface Mach Number Distributions for a Staggered DCA Cascade

83-12-22-5

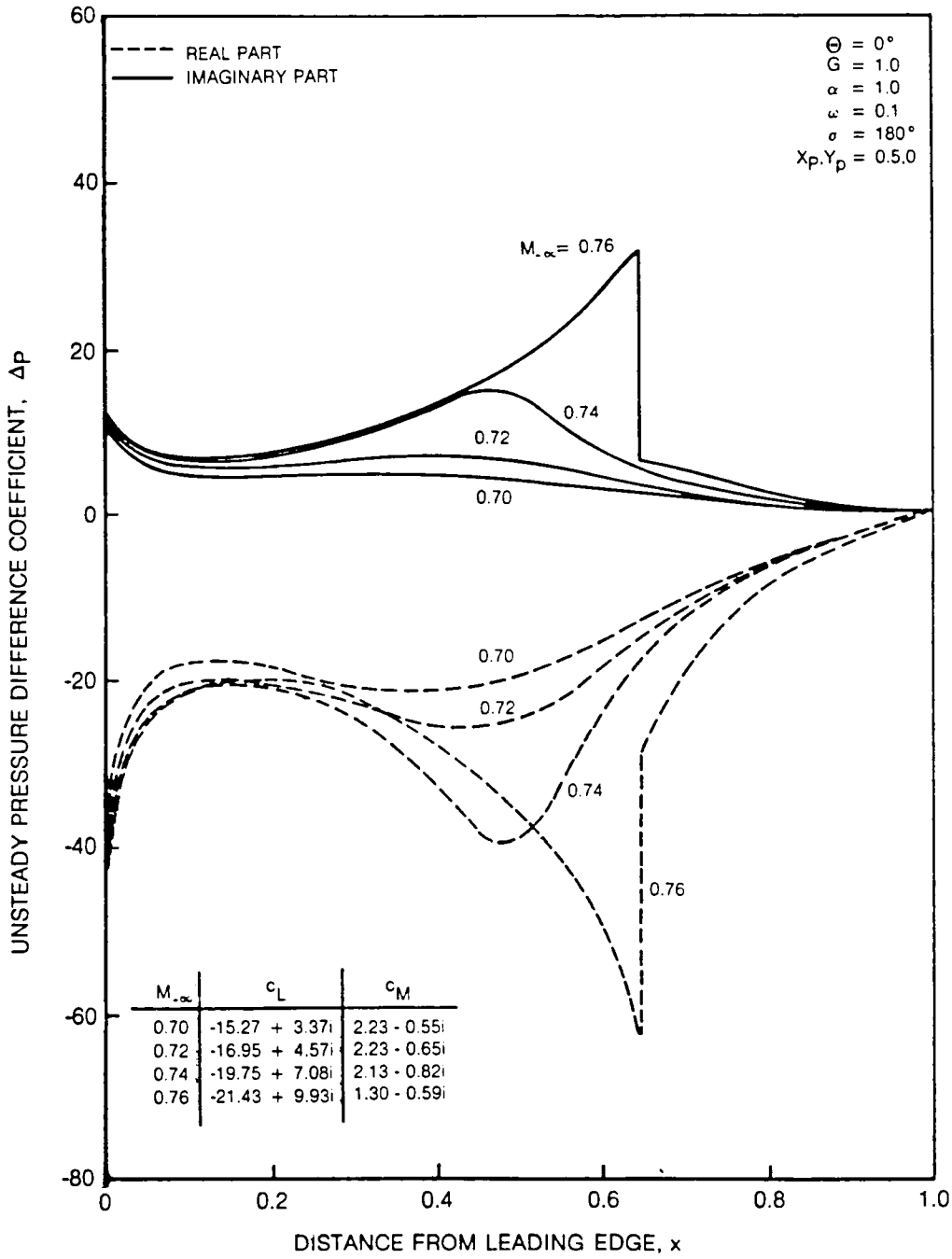

Fig. 5 Response Predictions, Determined on the Cascade Mesh, for Low-Frequency Torsional Vibrations of an Unstaggered DCA Cascade

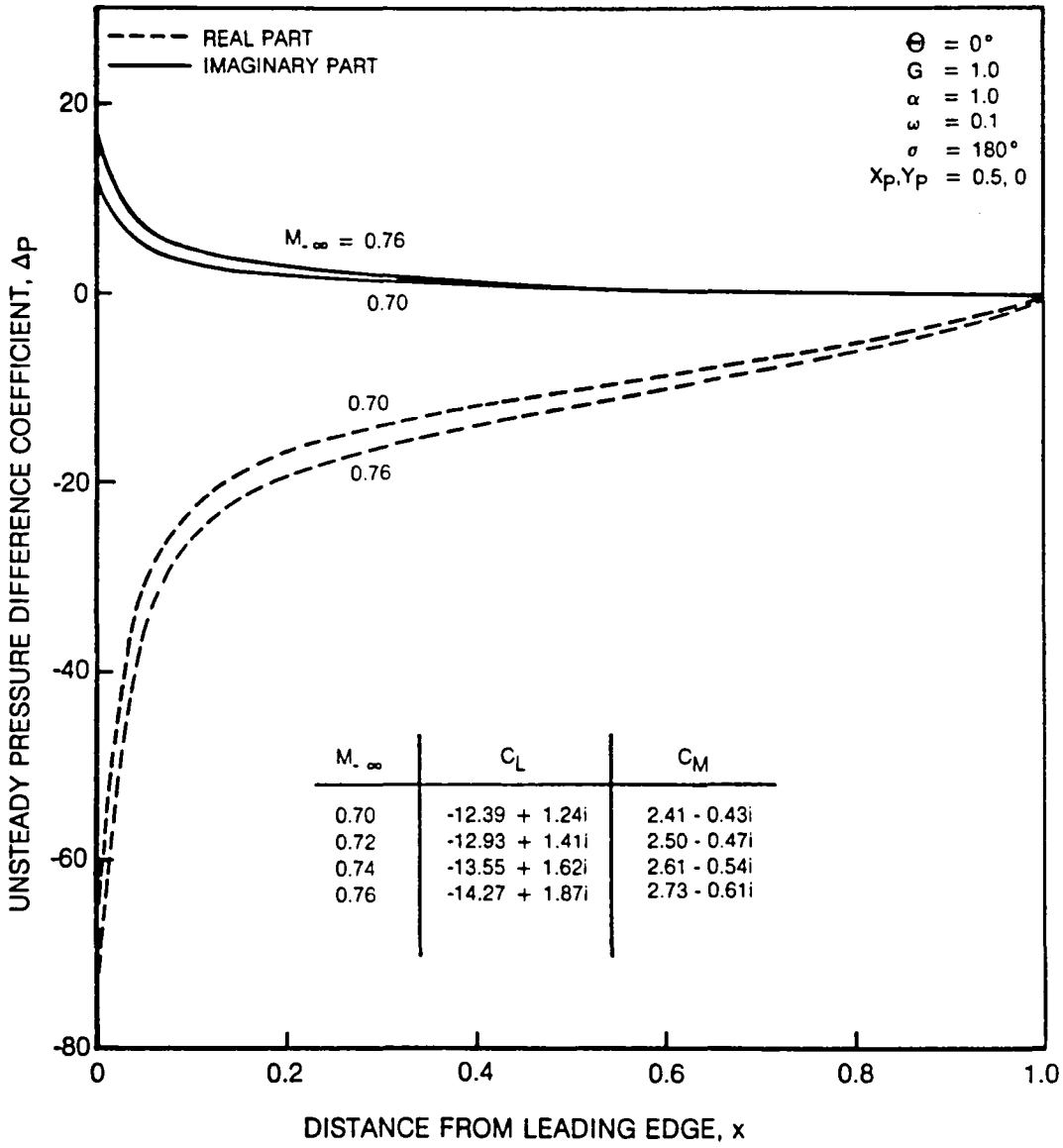

Fig. 6 Response Predictions for Low-Frequency Torsional Vibrations of an Unstaggered Flat-Plate Cascade

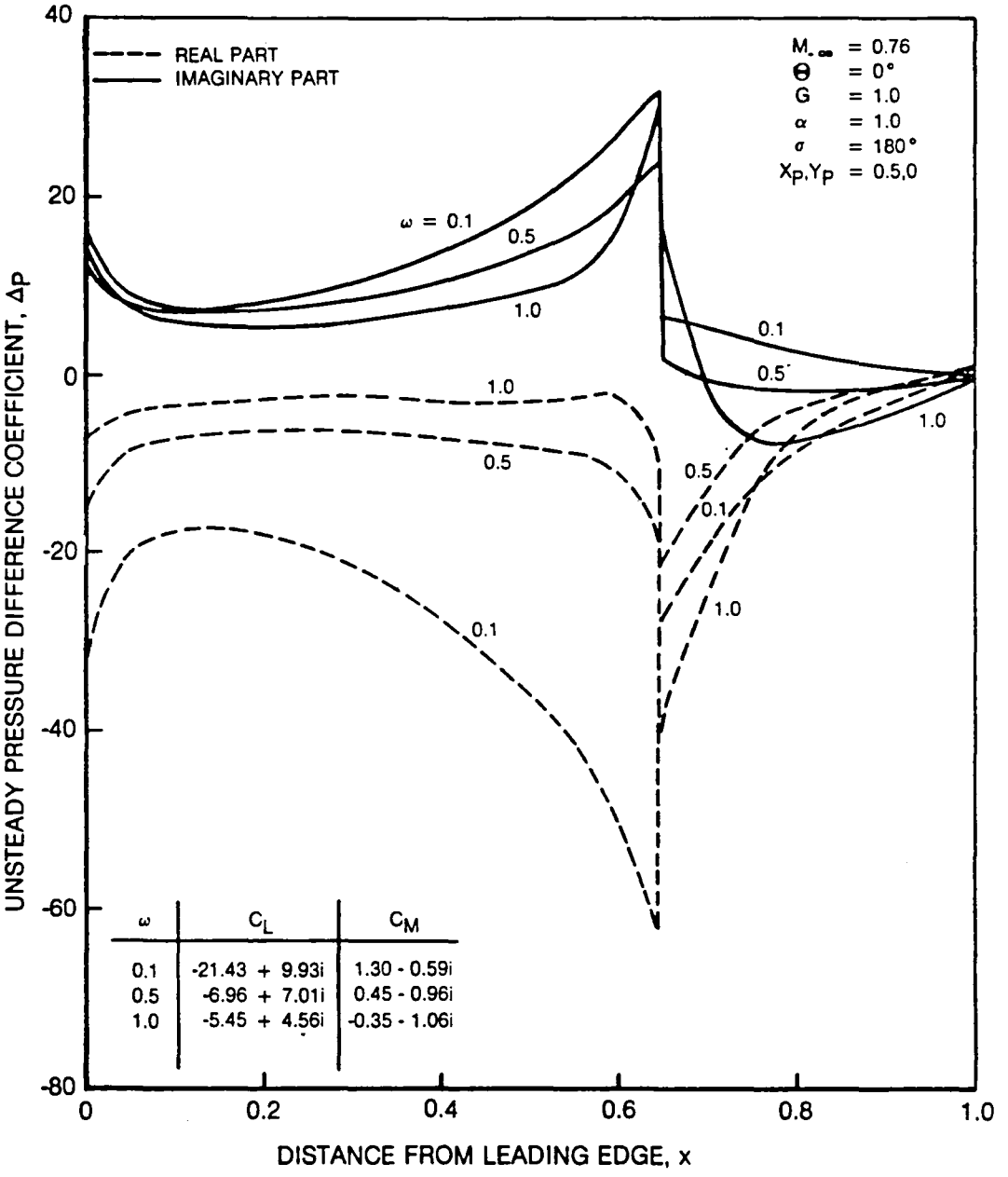

ω	C_L	C_M
0.1	-21.43 + 9.93i	1.30 - 0.59i
0.5	-6.96 + 7.01i	0.45 - 0.96i
1.0	-5.45 + 4.56i	-0.35 - 1.06i

Fig. 7 Cascade Mesh Response Predictions for Torsional Vibrations of an Unstaggered DCA Cascade

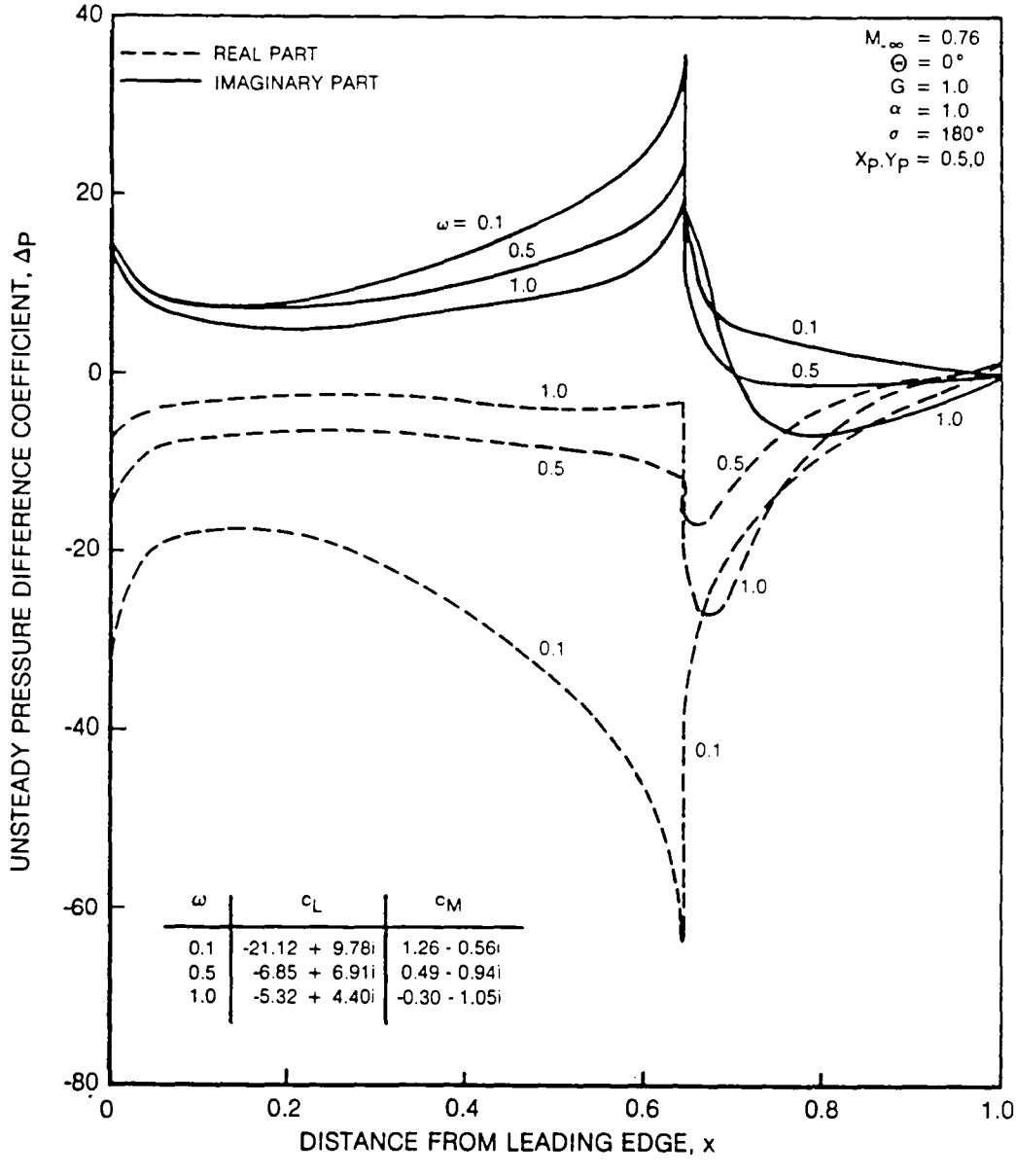

Fig. 8 Cascade Plus Local Mesh Response Predictions for Torsional Vibrations of an Unstaggered DCA Cascade: Unsteady Solutions Determined by Shock Capture

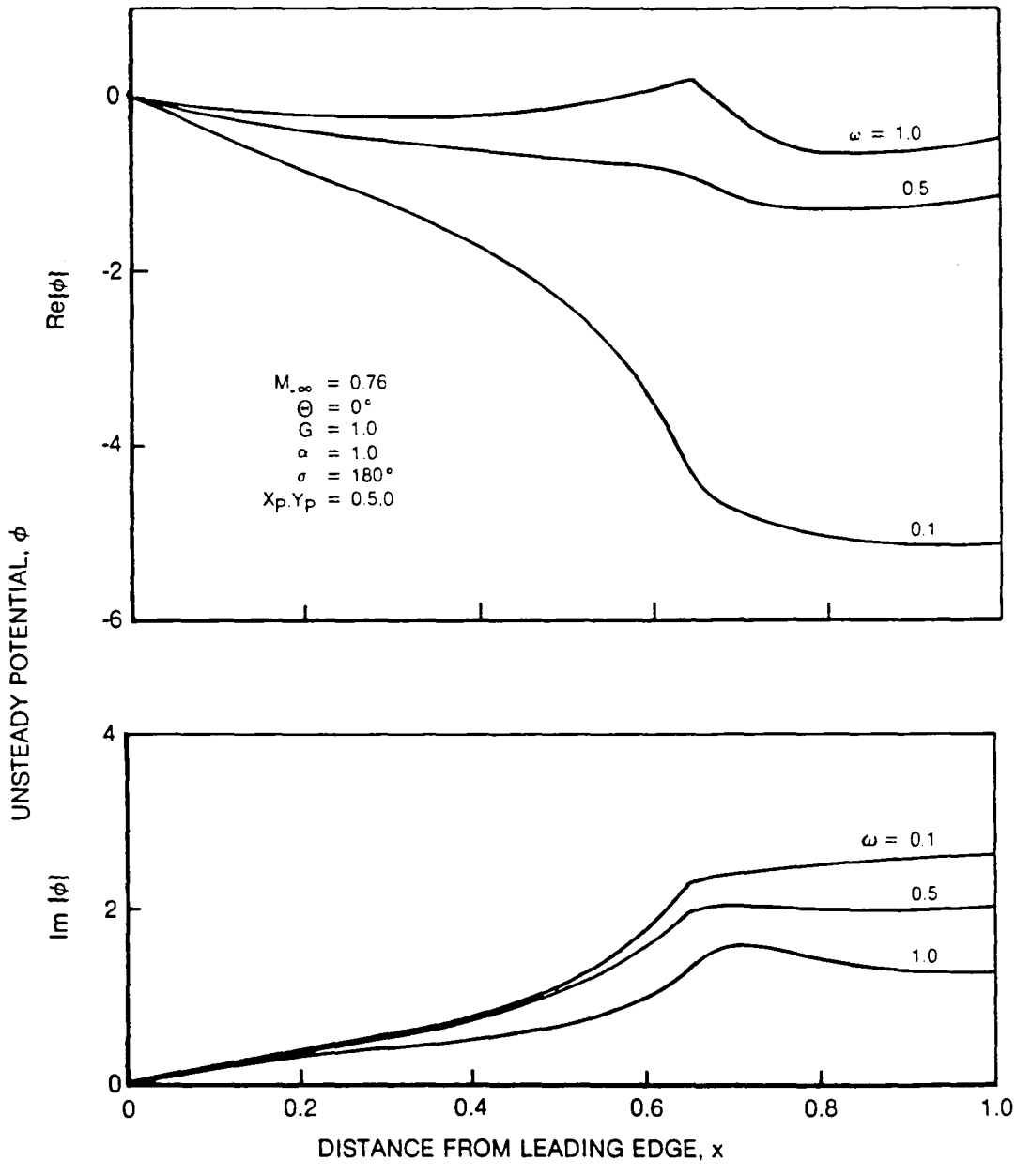

Fig. 9 Unsteady Potential Distributions on the Suction Surface of the Reference Blade of an Unstaggered DCA Cascade: Unsteady Solutions Determined by Shock Capture

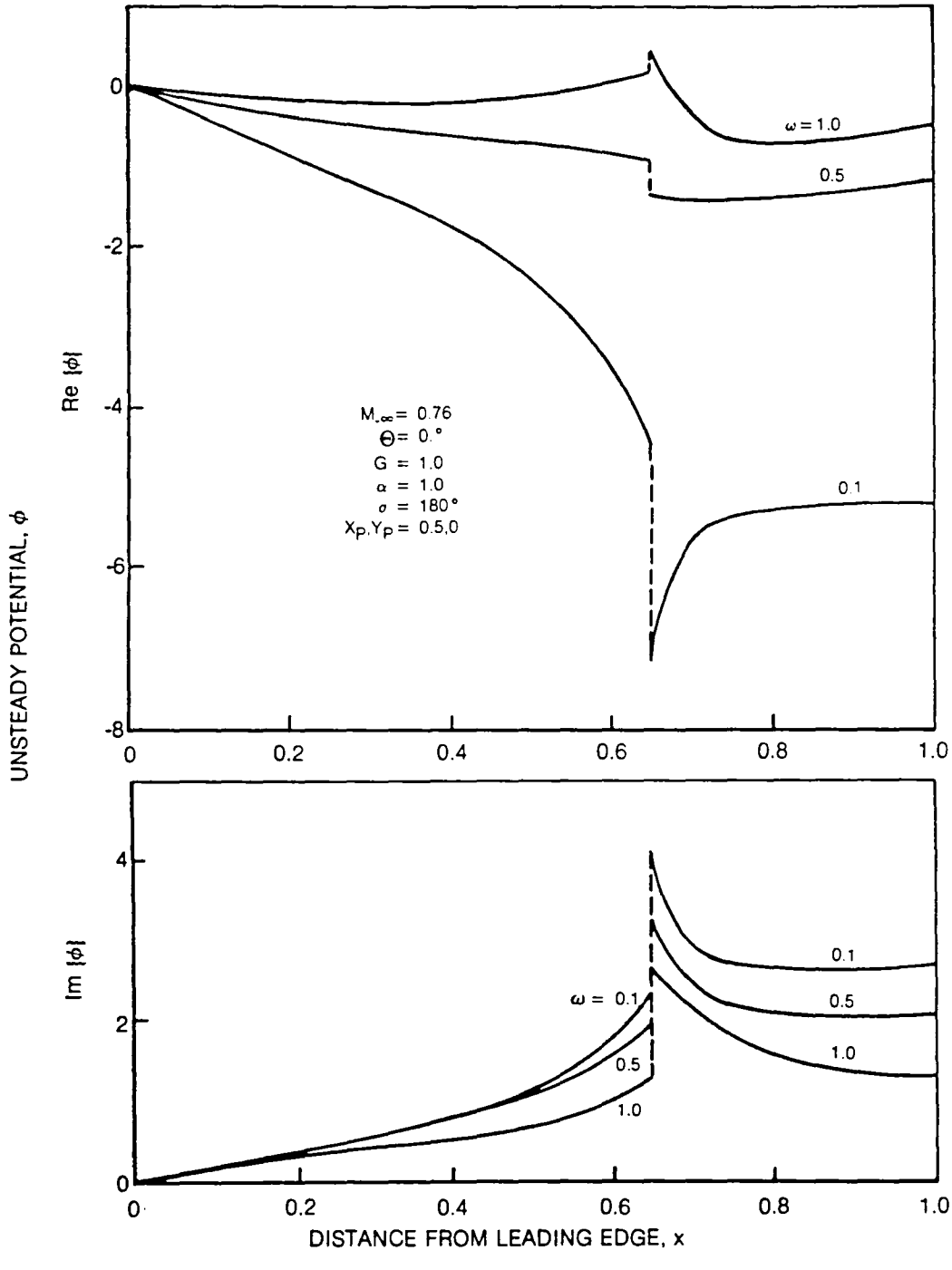

Fig. 10 Unsteady Potential Distributions on the Suction Surface of the Reference Blade of an Unstaggered DCA Cascade: Unsteady Solutions Determined by Shock Fit

83-9-87-8

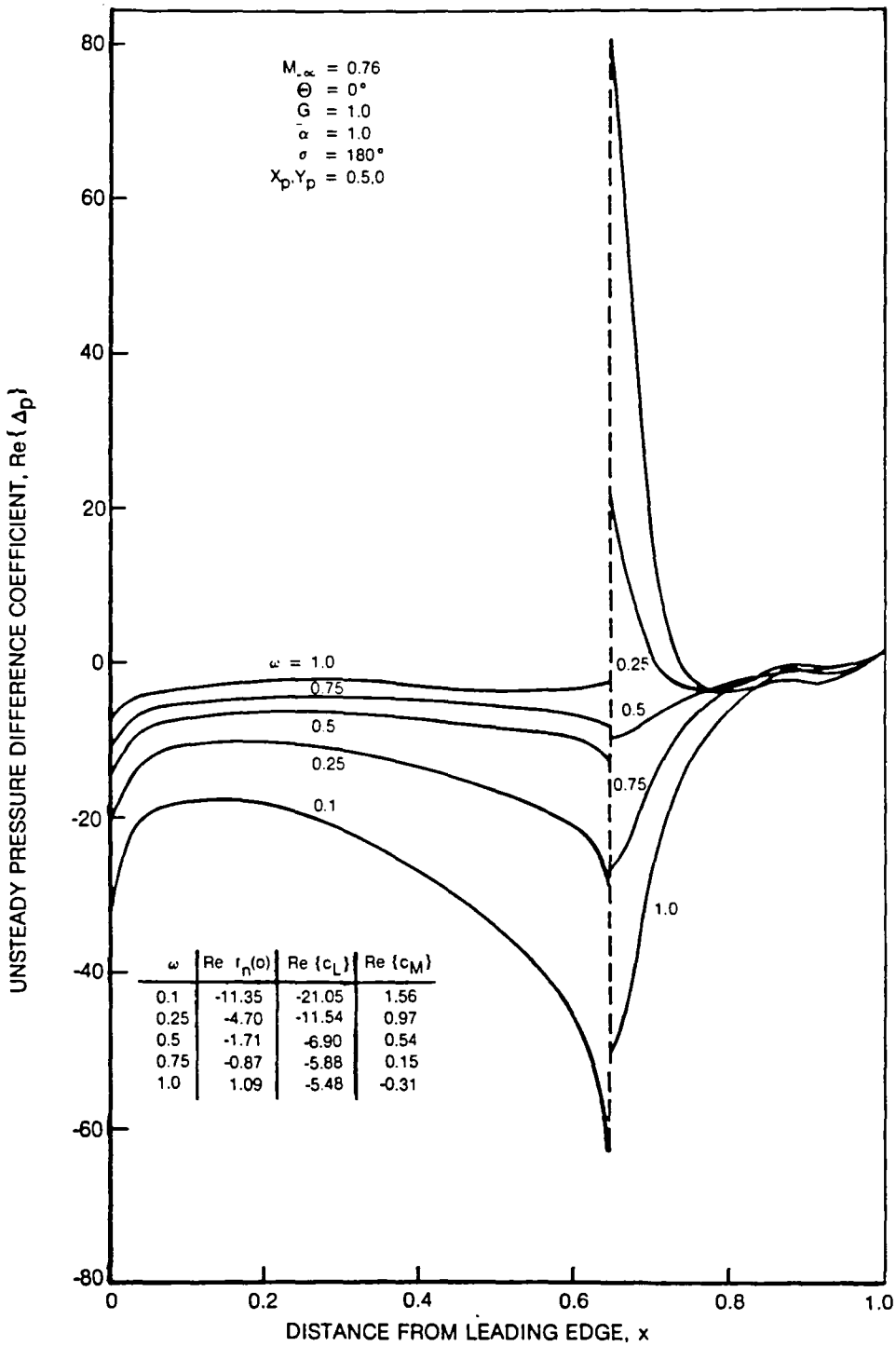

Fig. 11 Effect of Frequency on the Unsteady Response due to Torsional Vibrations of an Unstaggered DCA Cascade
a) In-phase Component (Real Part) of the Unsteady Response

83-9-87-9

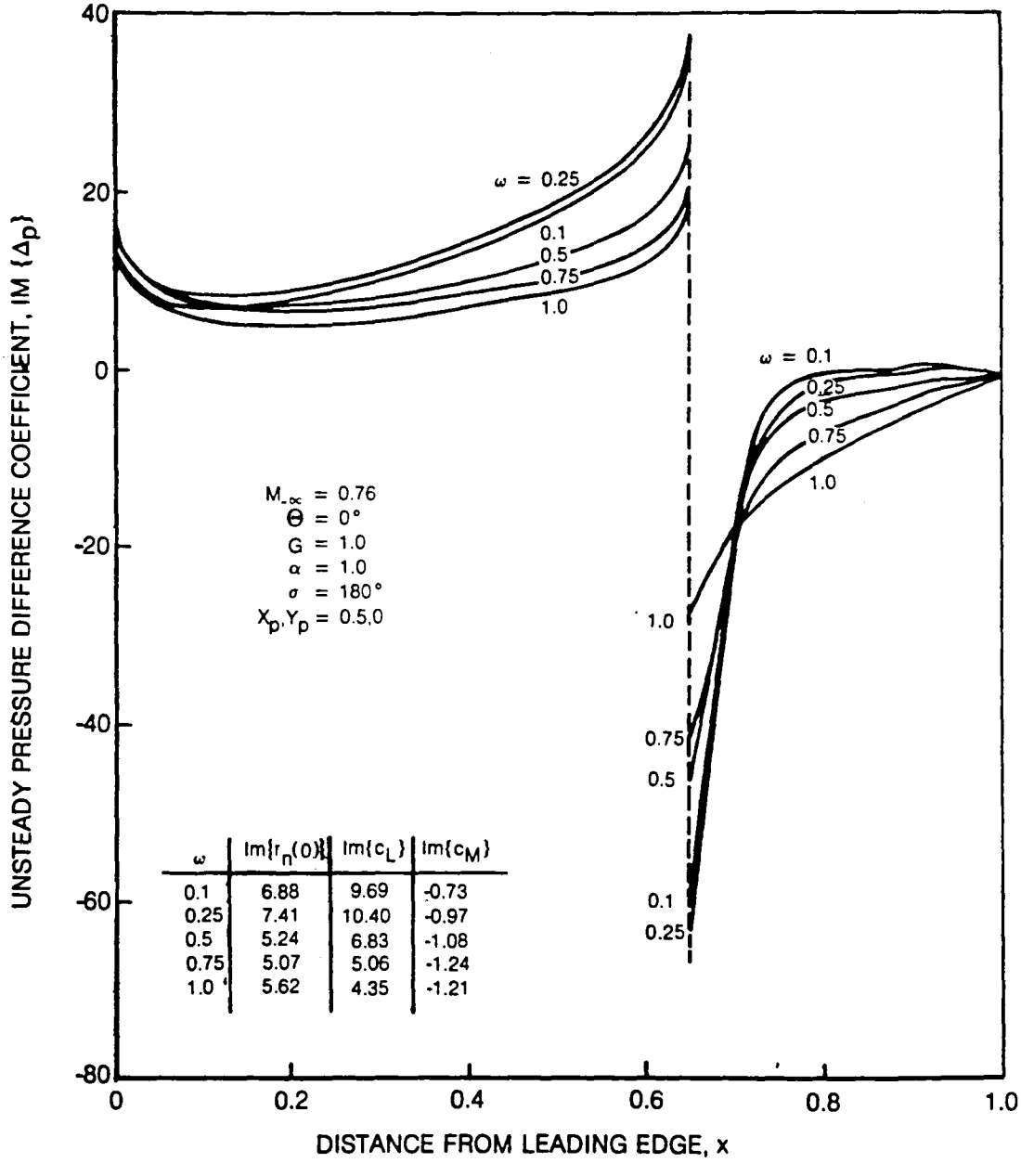

Fig. 11 Effect of Frequency on the Unsteady Response due to Torsional Vibrations of an Unstaggered DCA Cascade
b) Out-of-Phase Component (Imaginary Part) of the Unsteady Response

83-9-87-10

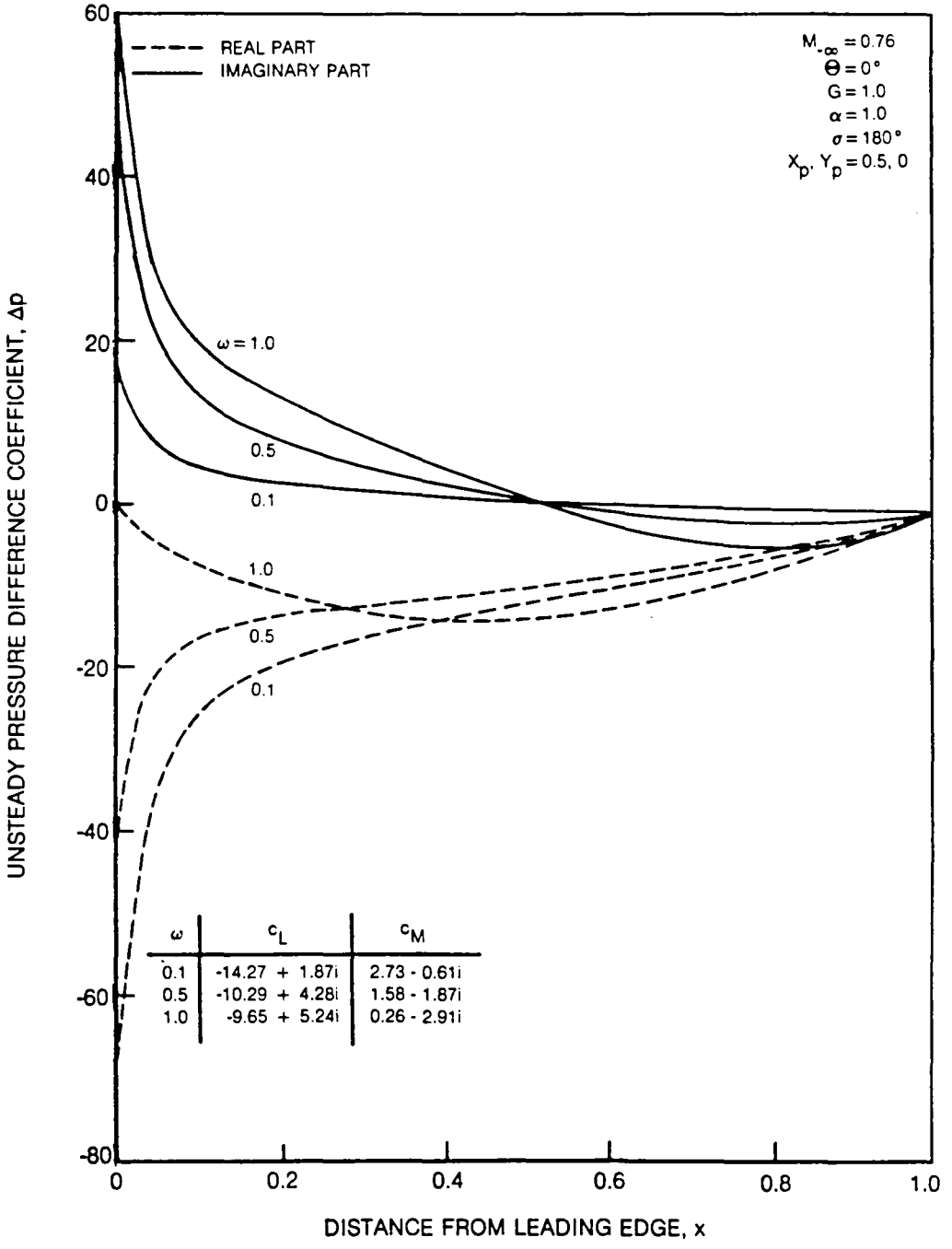

Fig. 12 Effect of Frequency on the Unsteady Response due to Torsional Vibrations of an Unstaggered Flat-Plate Cascade

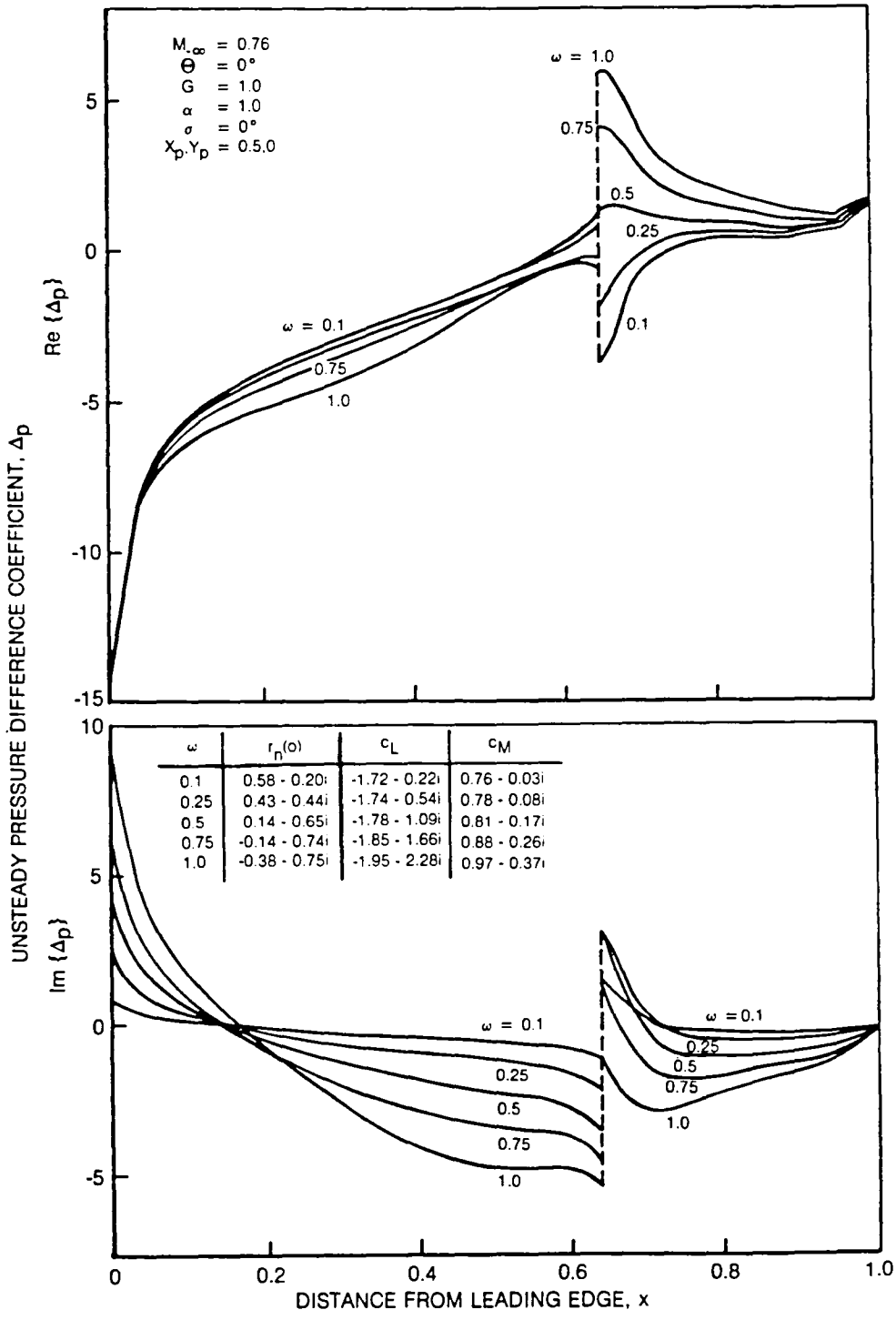

ω	$r_n(o)$	c_L	c_M
0.1	0.58 - 0.20i	-1.72 - 0.22i	0.76 - 0.03i
0.25	0.43 - 0.44i	-1.74 - 0.54i	0.78 - 0.08i
0.5	0.14 - 0.65i	-1.78 - 1.09i	0.81 - 0.17i
0.75	-0.14 - 0.74i	-1.85 - 1.66i	0.88 - 0.26i
1.0	-0.38 - 0.75i	-1.95 - 2.28i	0.97 - 0.37i

Fig. 13 Effect of Frequency on the Unsteady Response due to In-Phase Torsional Vibrations of an Unstaggered DCA Cascade

83-9-87-12

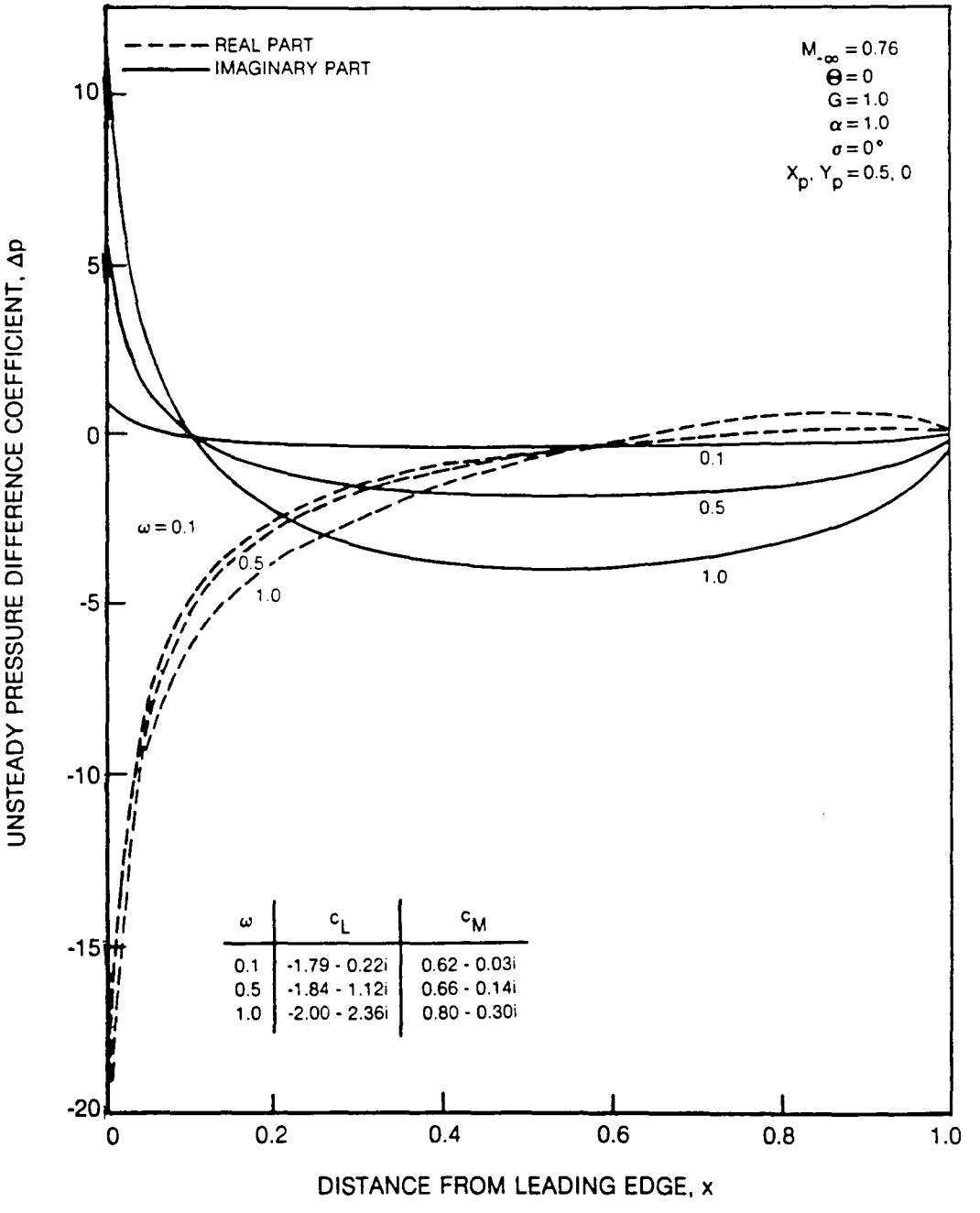

Fig. 14 Effect of Frequency on the Unsteady Response to In-Phase Torsional Vibrations of an Unstaggered Flat-Plate Cascade

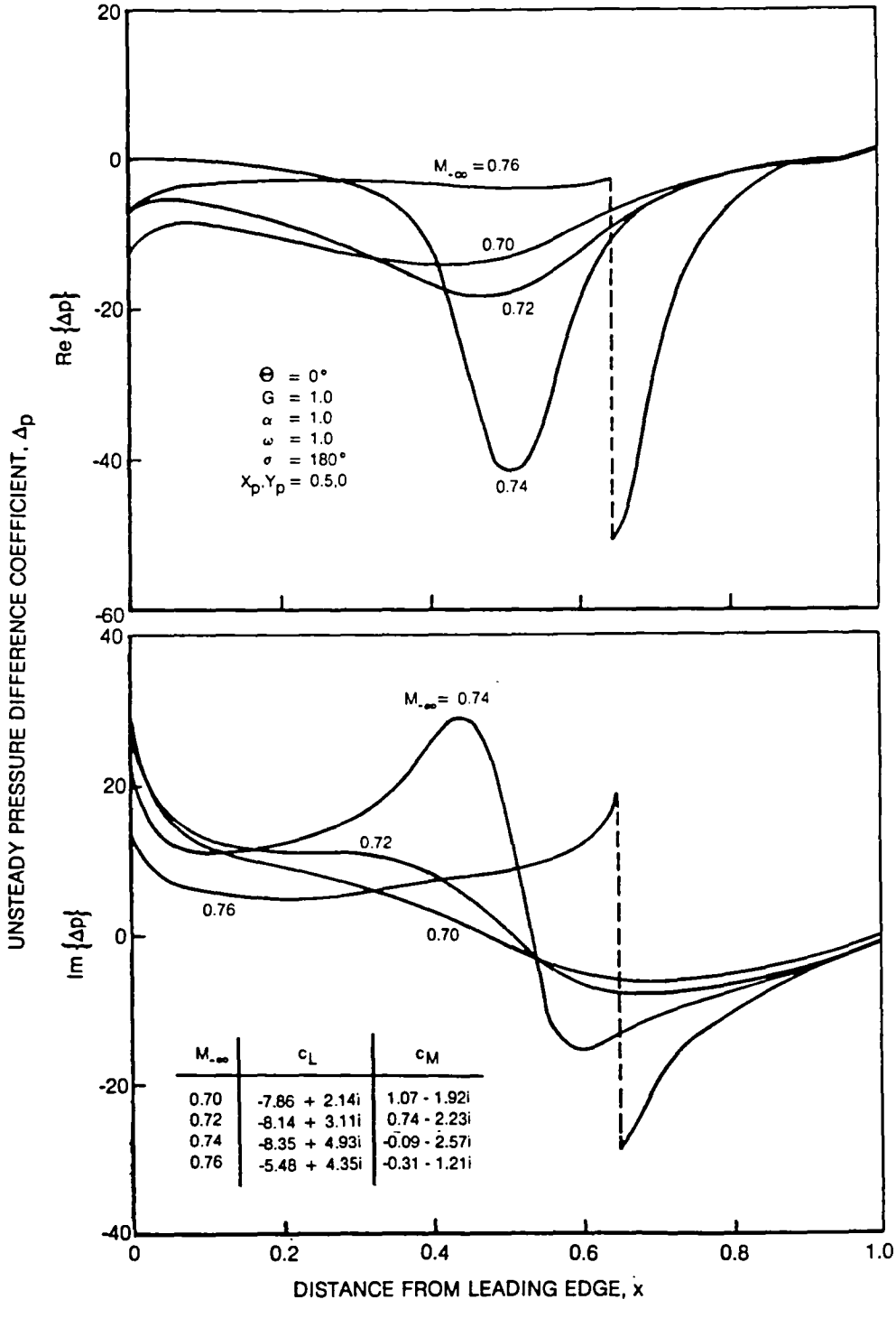

Fig. 15 Effect of Mach Number on the Unit-Frequency Response due to Out-of-Phase ($\sigma = 180$ deg.) Torsional Vibrations of a Staggered DCA Cascade

83-9-87-11

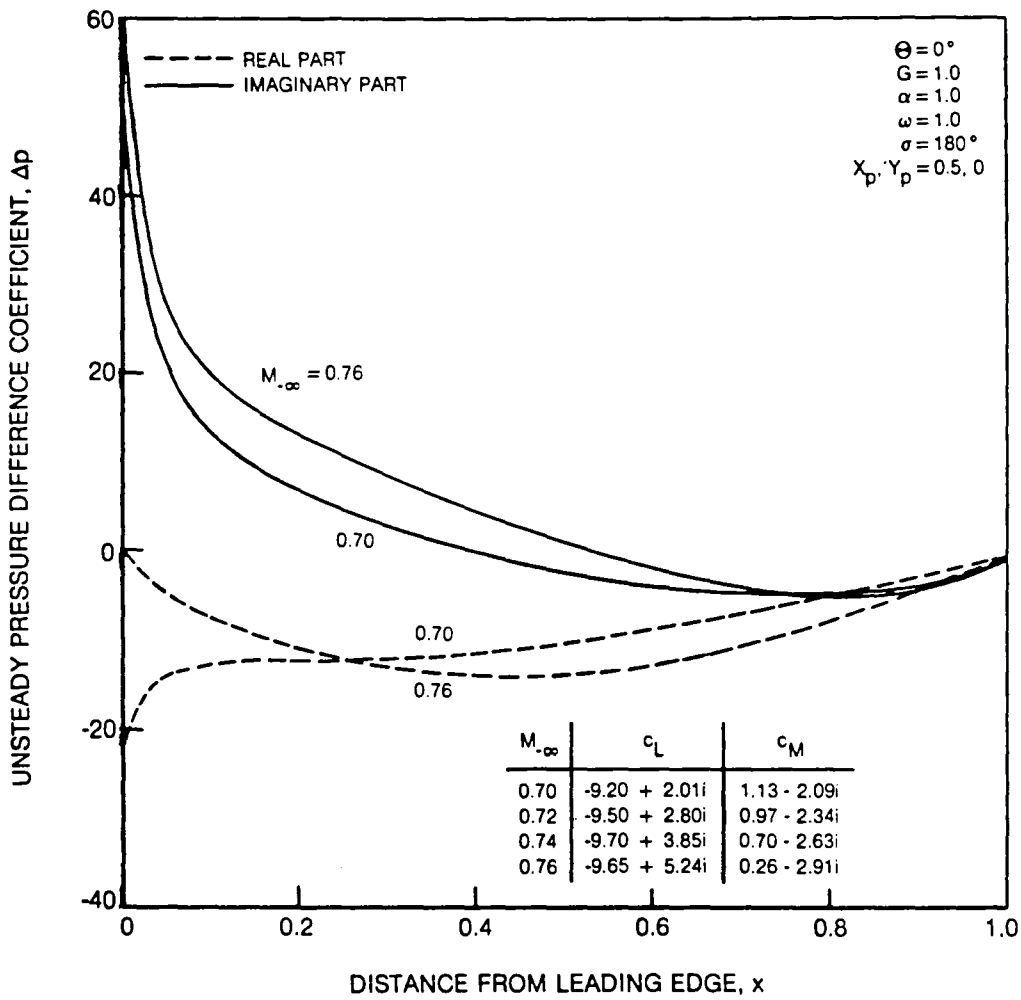

Fig. 16 Effect of Mach Number on the Unit-Frequency Response due to Out-of-Phase Torsional Vibrations of an Unstaggered Flat-Plate Cascade

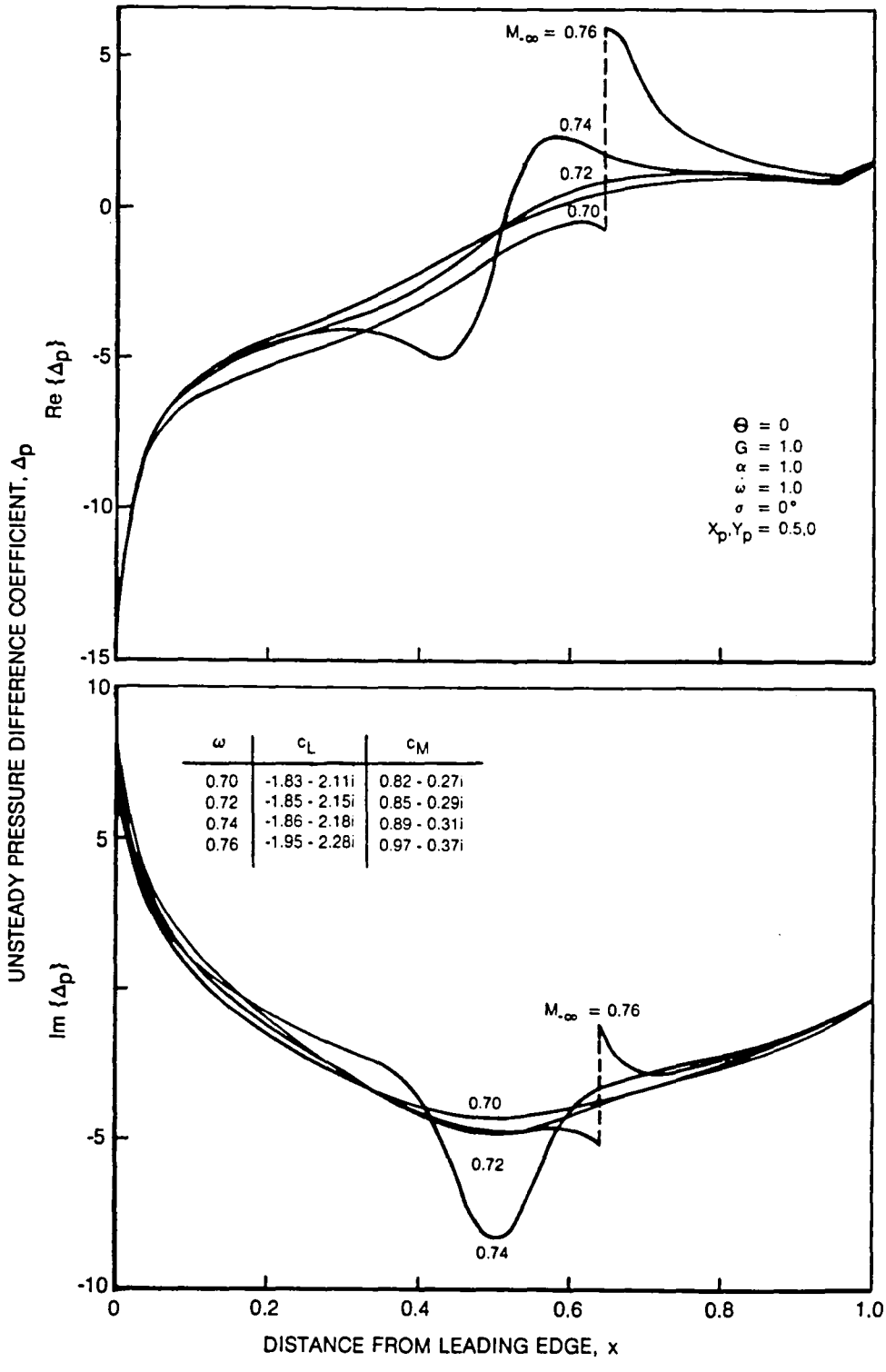

Fig. 17 Effect of Mach Number on the High-Frequency Response to In-Phase (σ = 0 deg.) Torsional Vibrations of an Unstaggered DCA Cascade

83-9-87-13

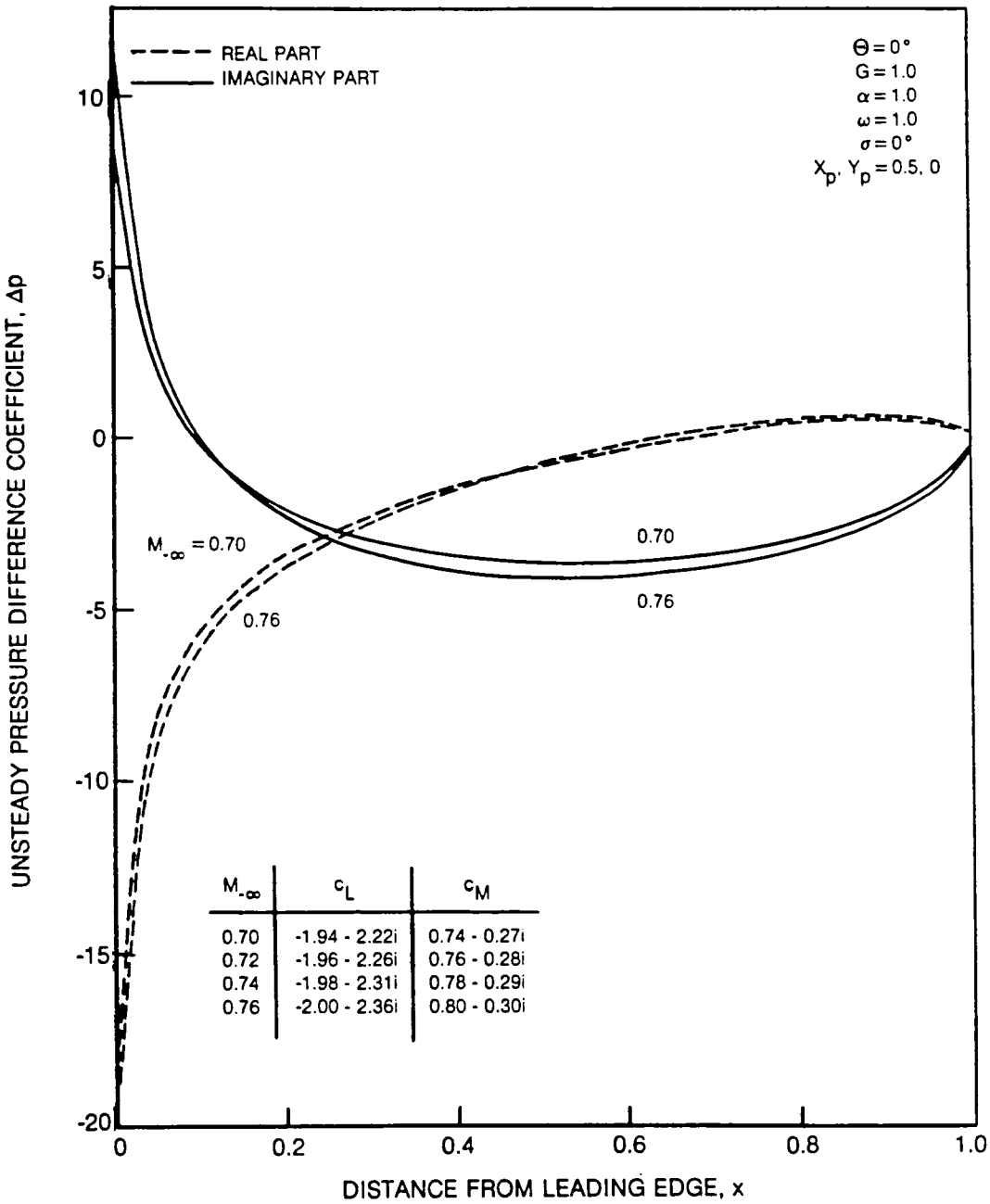

Fig. 18 Effect of Mach Number on the Unit-Frequency Response to In-Phase ($\sigma = 0$ deg.) Torsional Vibrations of an Unstaggered Flat-Plate Cascade

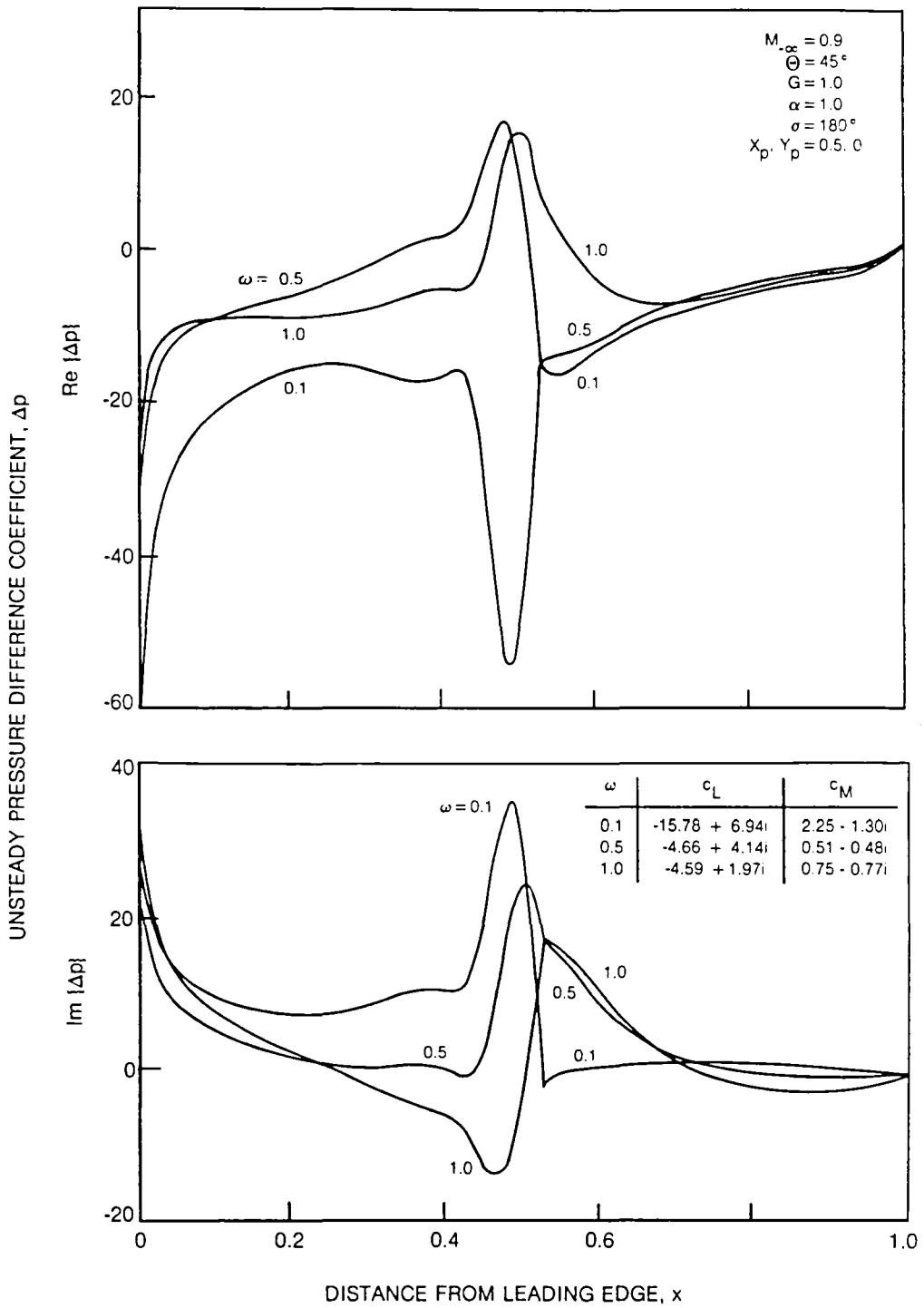

Fig. 19 Cascade Mesh Response Predictions for Torsional Vibrations of a Staggered DCA Cascade

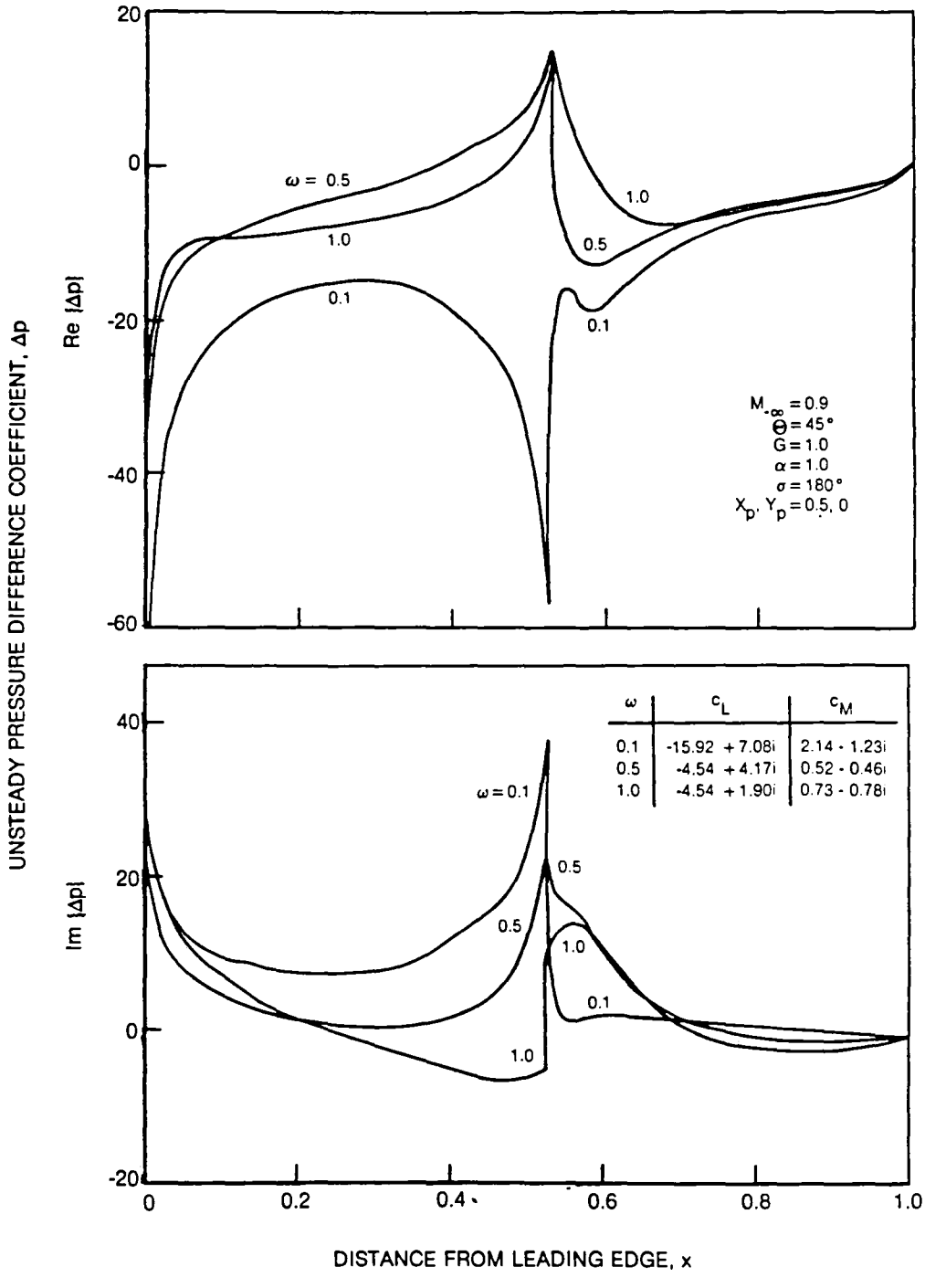

Fig. 20 Cascade Plus Local Mesh Response Predictions for Torsional Vibrations of a Staggered DCA Cascade: Unsteady Solutions Determined by Shock Capture

83-12-22-18

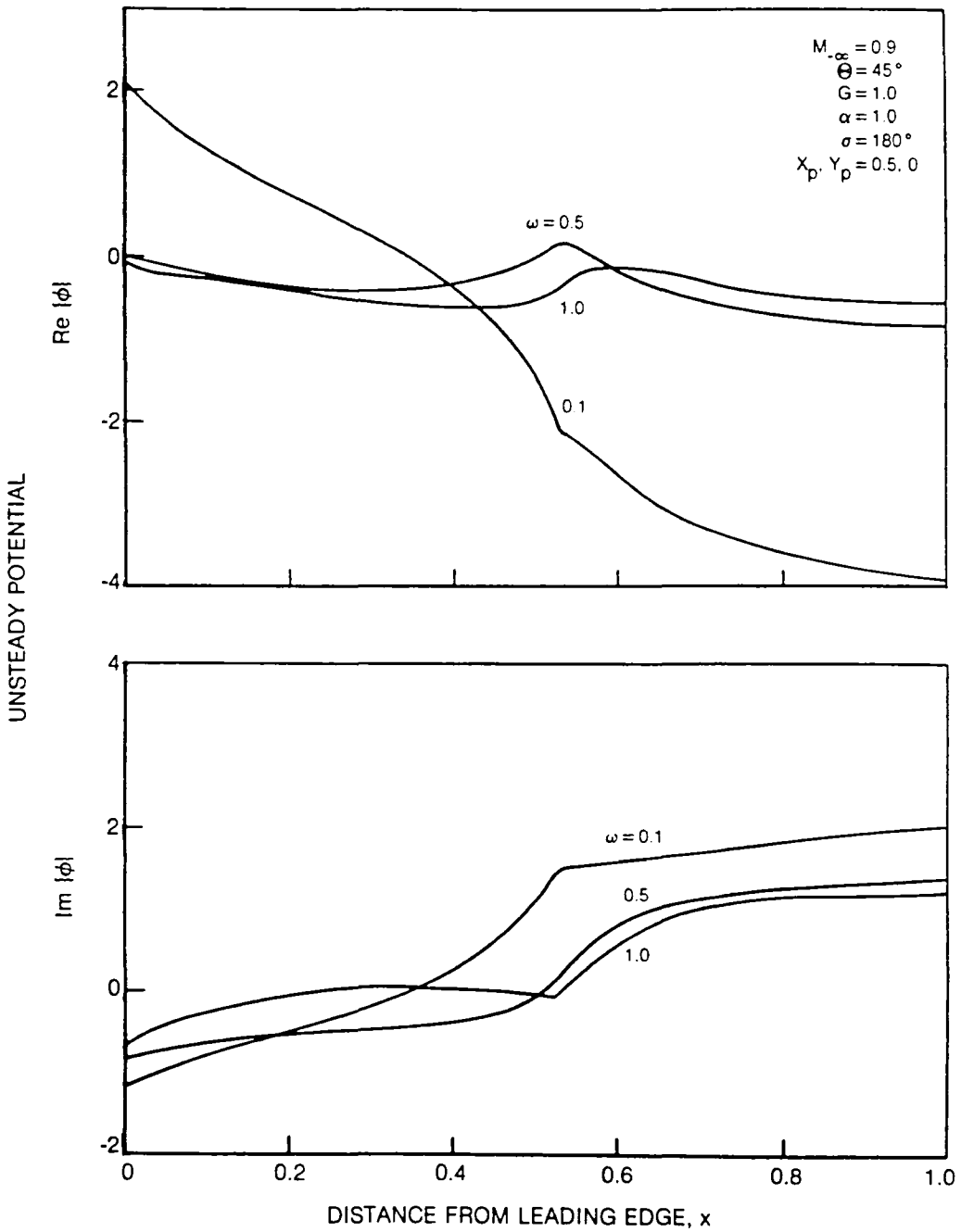

Fig. 21 Unsteady Potential Distributions on the Suction Surface of the Reference Blade of a Staggered DCA Cascade: Unsteady Solutions Determined by Shock Capture

83-12-22-19

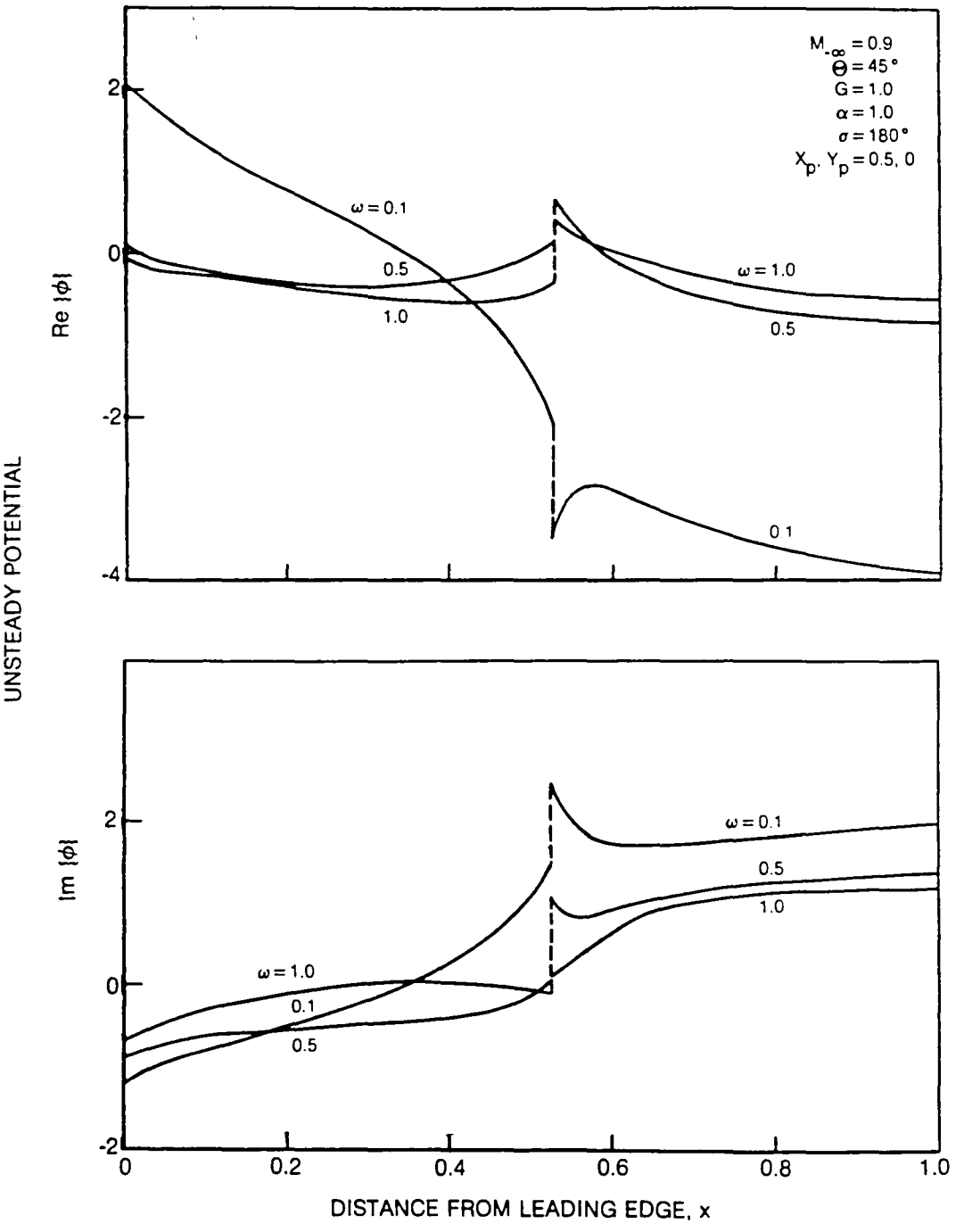

Fig. 22 Unsteady Potential Distributions on the Suction Surface of the Reference Blade of a Staggered DCA Cascade: Unsteady Solutions Determined by Shock Fit

83-12-22-20

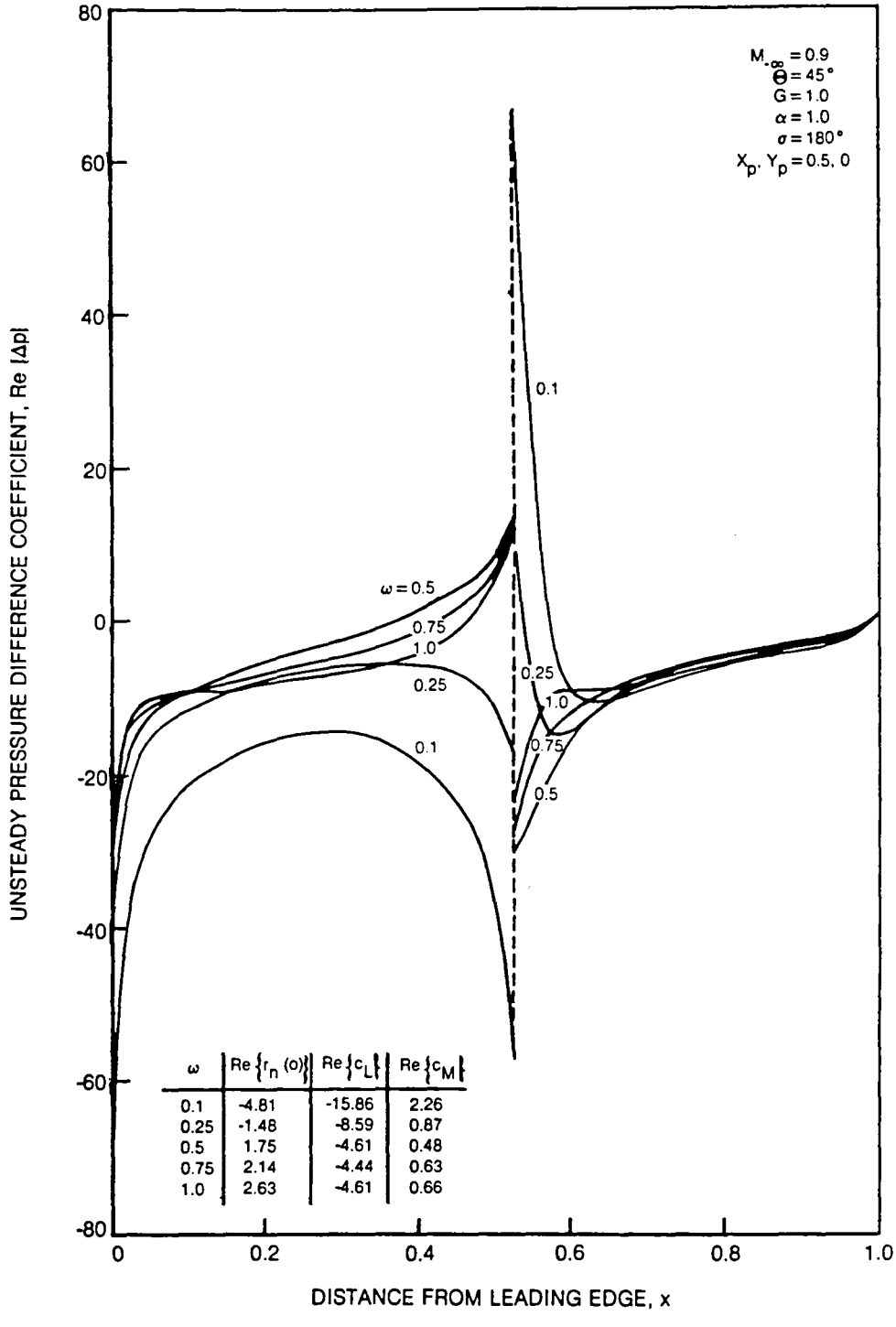

ω	Re {r_n (o)}	Re {c_L}	Re {c_M}
0.1	-4.81	-15.86	2.26
0.25	-1.48	-8.59	0.87
0.5	1.75	-4.61	0.48
0.75	2.14	-4.44	0.63
1.0	2.63	-4.61	0.66

Fig. 23 Effect of Frequency on the Unsteady Response due to Torsional Vibrations of a Staggered DCA Cascade
a) In-Phase Component (Real Part) of the Unsteady Response

83-12-22-21

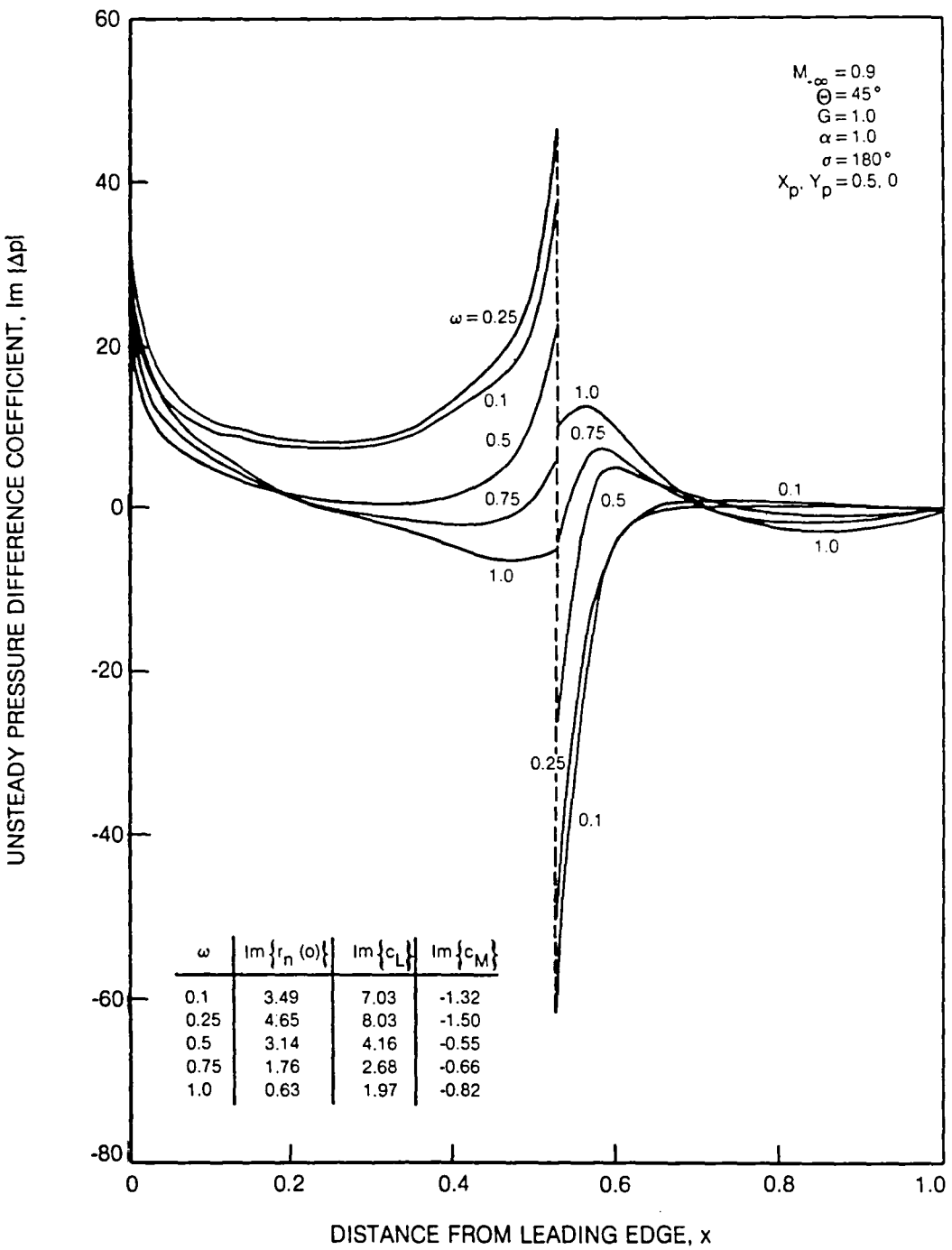

Fig. 23 Effect of Frequency on the Unsteady Response due to Torsional Vibrations of a Staggered DCA Cascade
b) Out-of-Phase Component (Imaginary Part) of the Unsteady Response

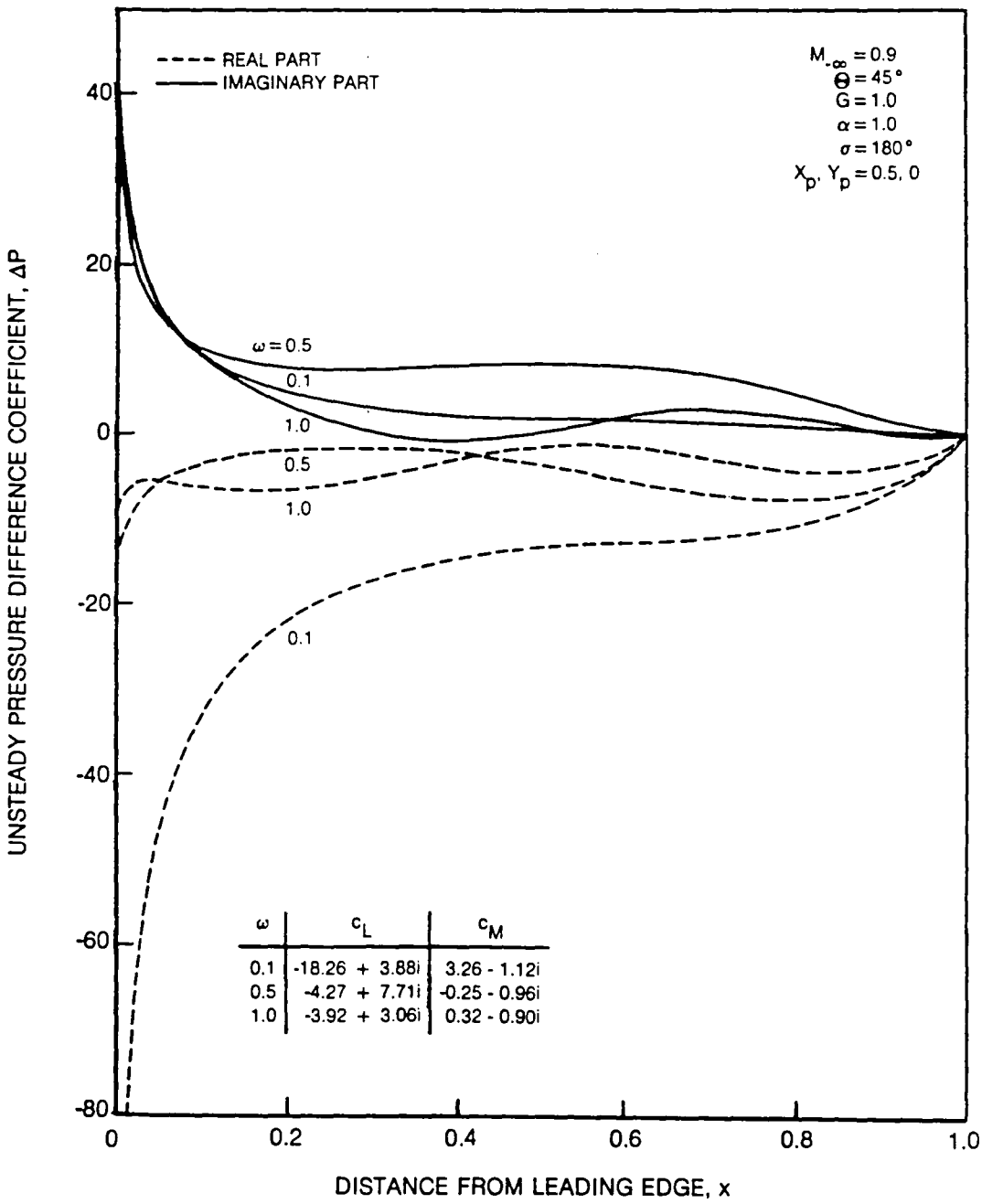

Fig. 24 Effect of Frequency on the Unsteady Response due to Torsional Vibrations of Staggered Flat-Plate Cascade

83-12-22-23

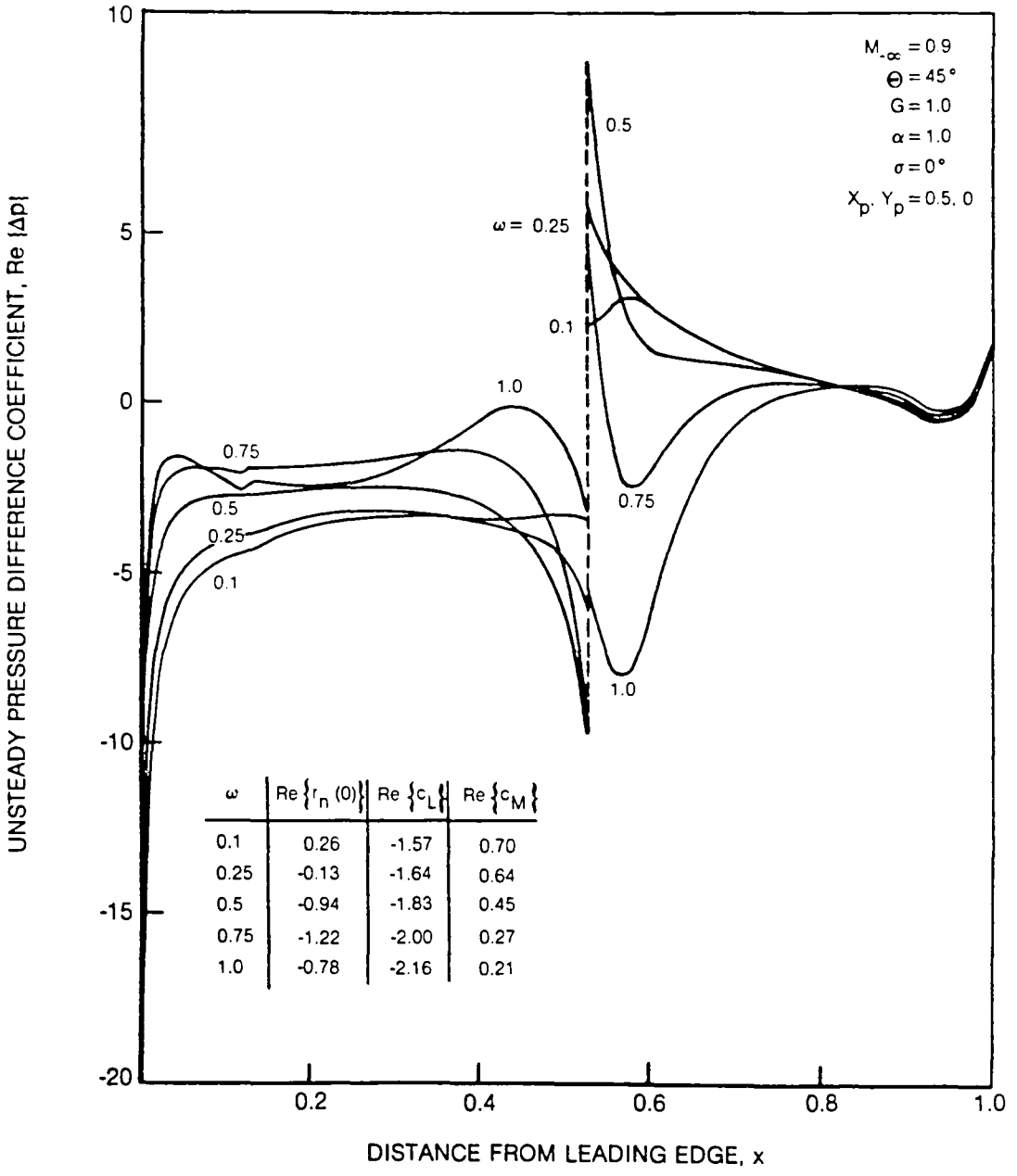

ω	Re $\{r_n(0)\}$	Re $\{c_L\}$	Re $\{c_M\}$
0.1	0.26	-1.57	0.70
0.25	-0.13	-1.64	0.64
0.5	-0.94	-1.83	0.45
0.75	-1.22	-2.00	0.27
1.0	-0.78	-2.16	0.21

Fig. 25 Effect of Frequency on the Unsteady Response Due to In-Phase ($\sigma = 0$ deg.) Torsional Vibrations of a Staggered DCA Cascade

a) In-Phase Component (Real Part) of the Unsteady Response

83-12-22-24

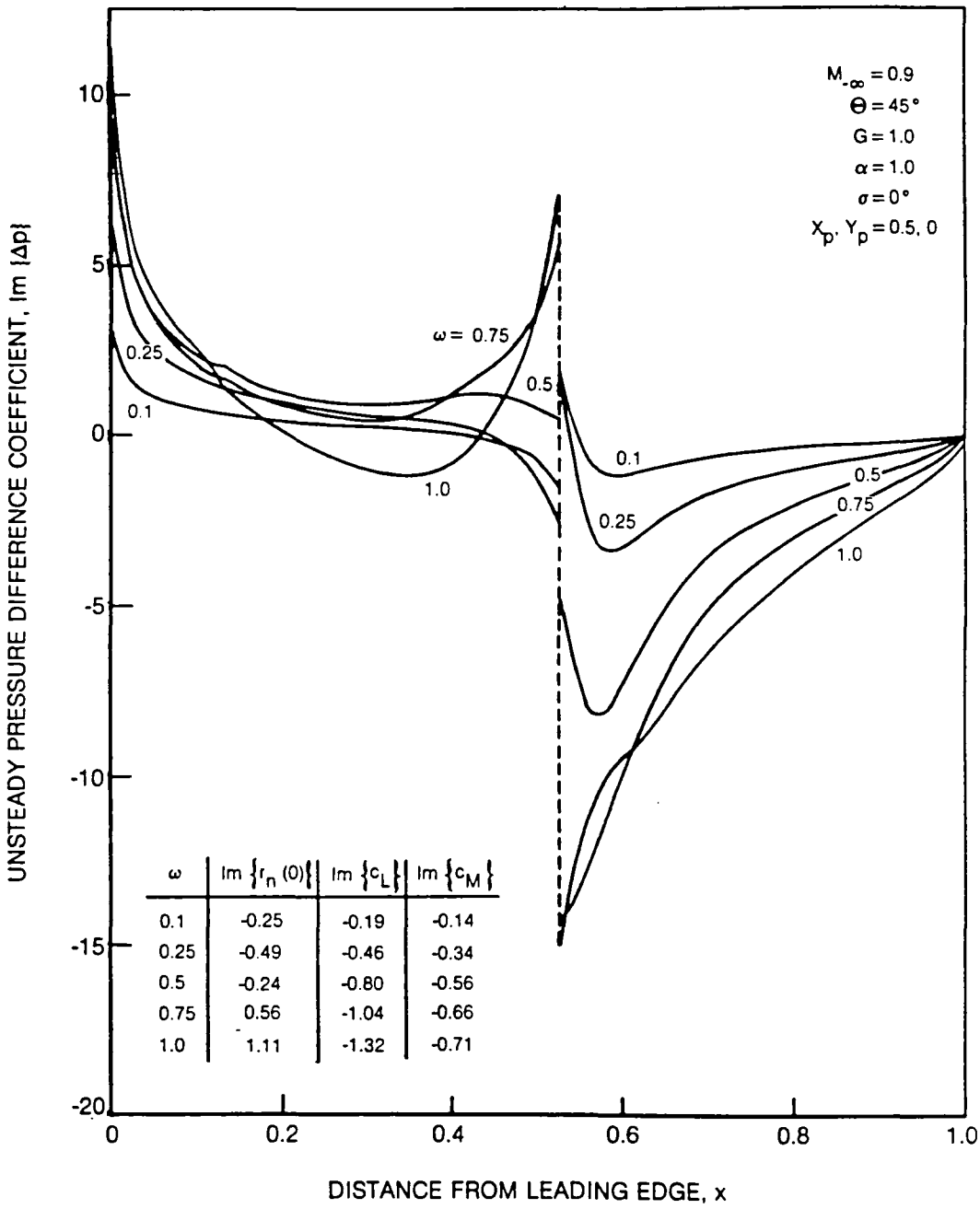

ω	Im $\{r_n(0)\}$	Im $\{c_L\}$	Im $\{c_M\}$
0.1	-0.25	-0.19	-0.14
0.25	-0.49	-0.46	-0.34
0.5	-0.24	-0.80	-0.56
0.75	0.56	-1.04	-0.66
1.0	1.11	-1.32	-0.71

Fig. 25 Effect of Frequency on the Unsteady Response due to In-Phase ($\sigma = 0$ deg.) Torsional Vibrations of a Staggered DCA Cascade
b) Out-of-Phase Component (Imaginary Part) of the Unsteady Response

83-12-22-25

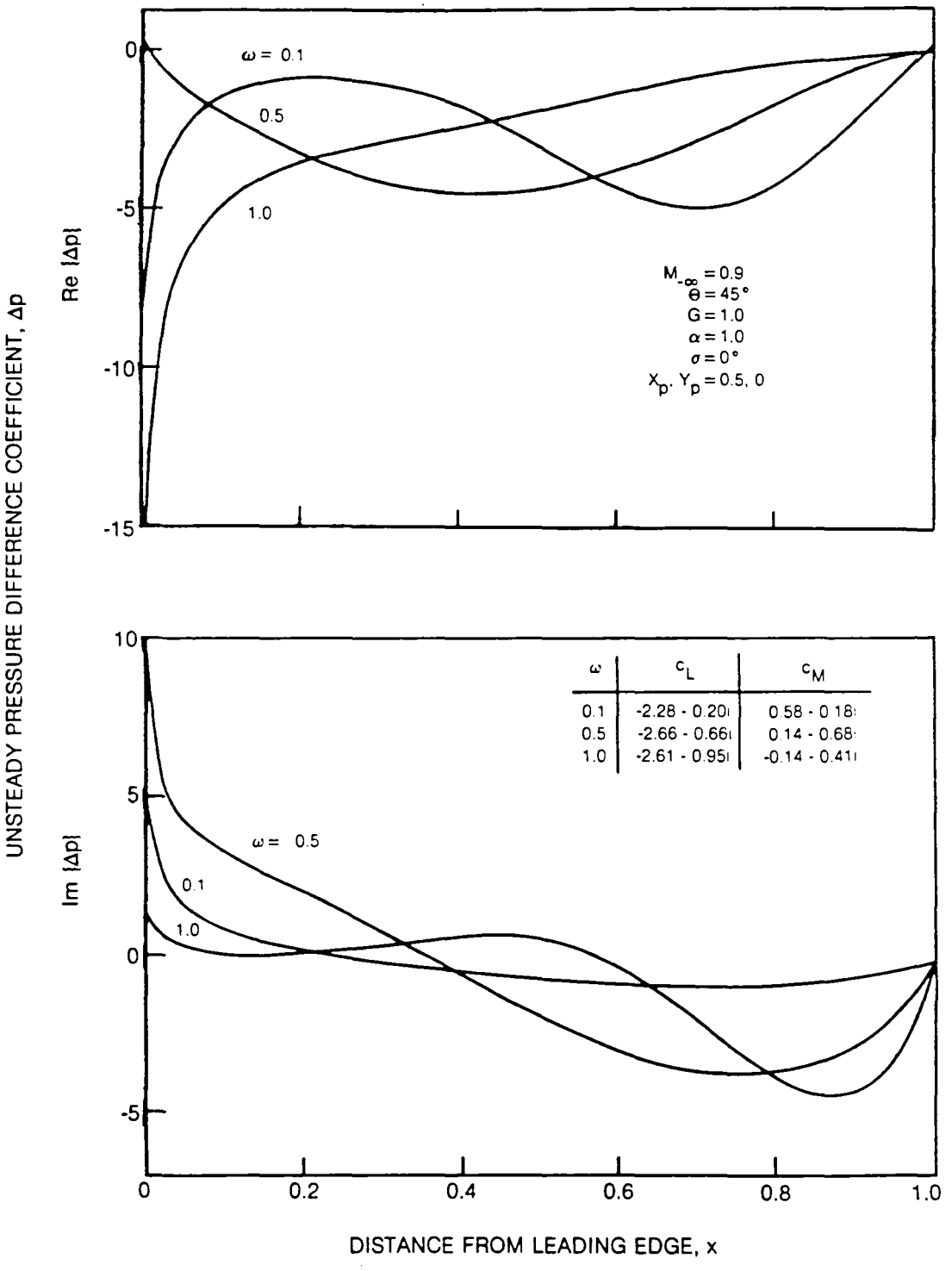

Fig. 26 Effect of Frequency on the Unsteady Response due to In-Phase Torsional Vibrations of a Staggered Flat-Plate Cascade

83-12-22-26

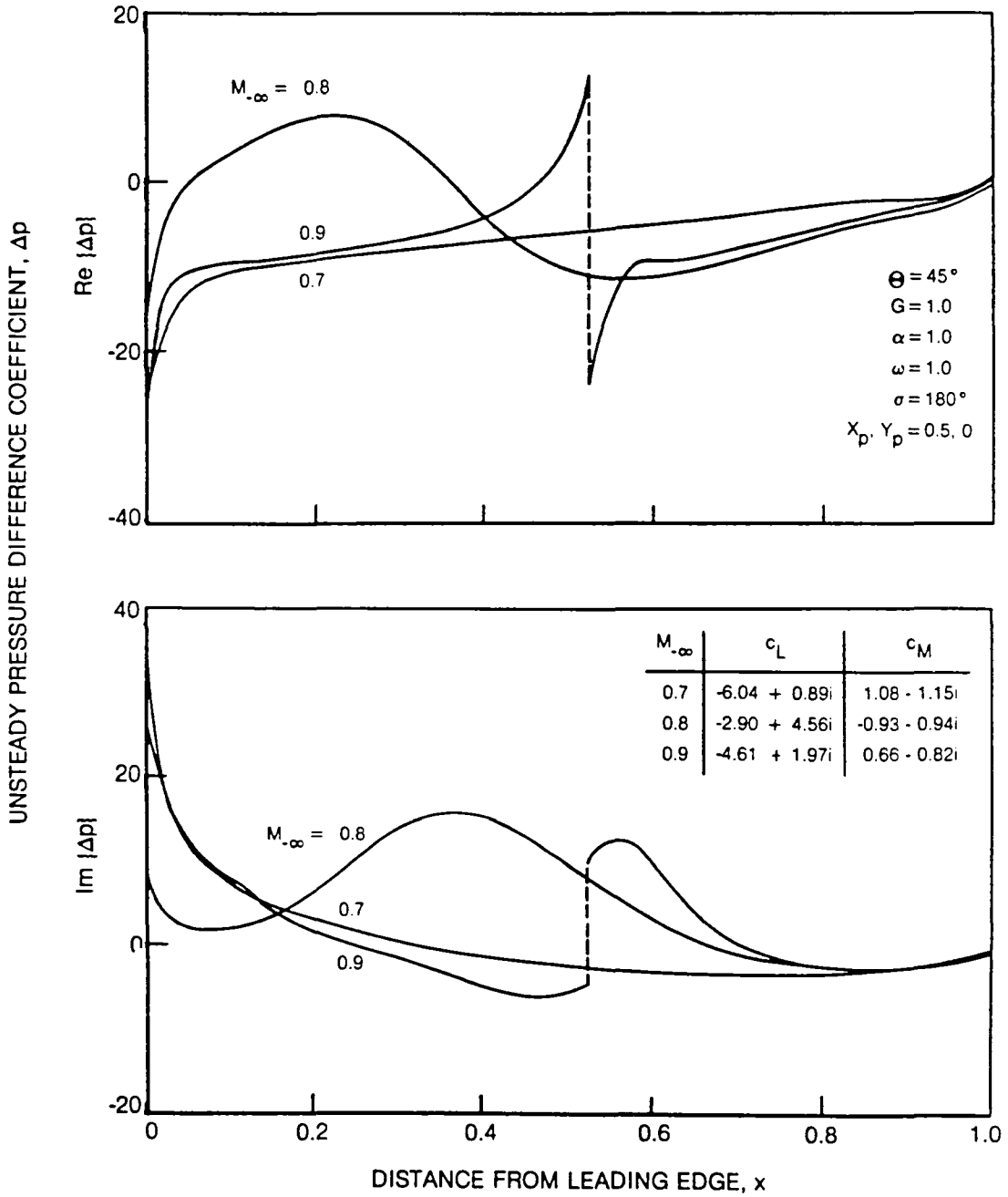

Fig. 27 Effect of Mach Number on the Unit-Frequency Response to Out-of-Phase ($\sigma = 180$ deg.) Torsional Vibrations of an Unstaggered DCA Cascade

83-12-22-27

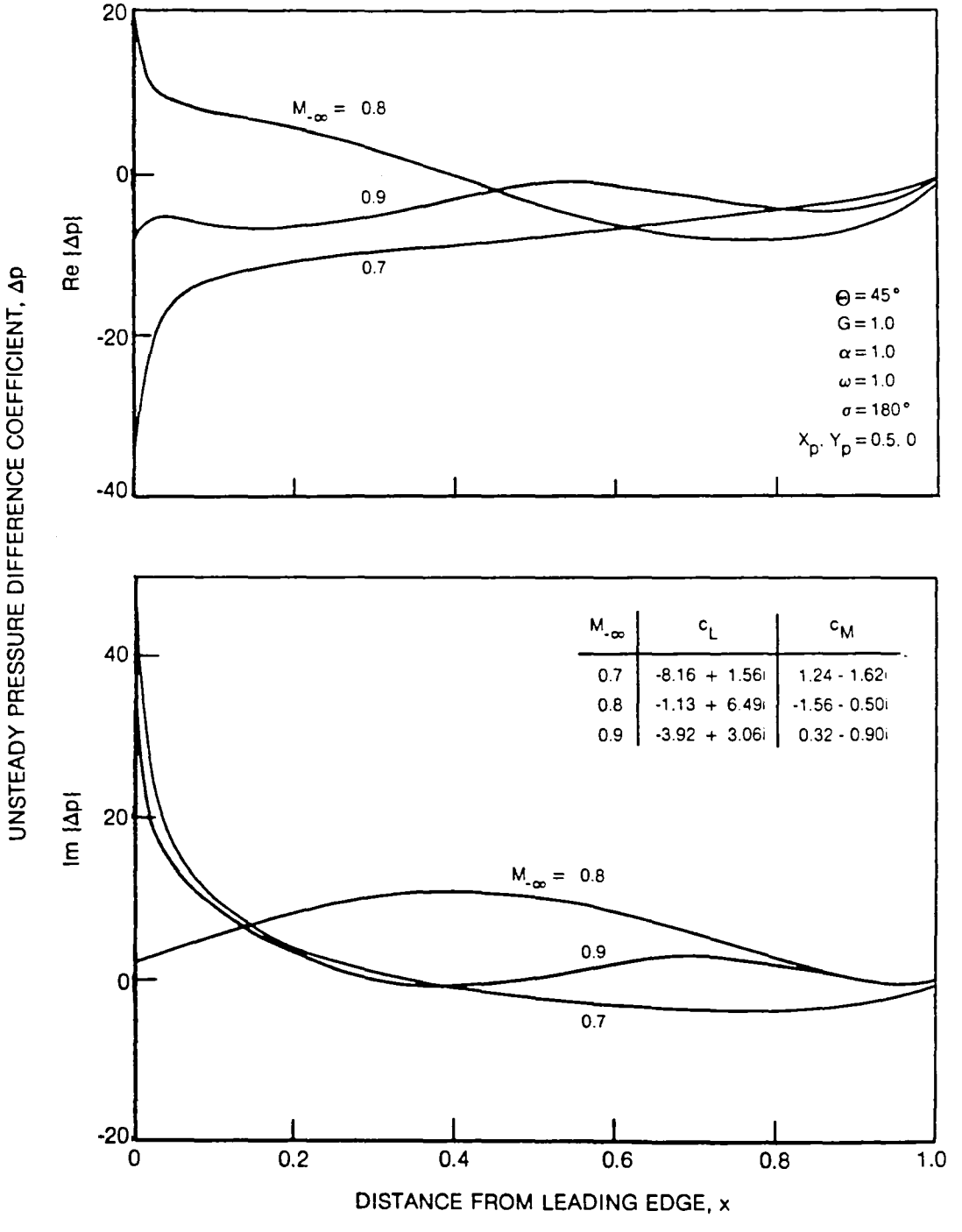

Fig. 28 Effect of Mach Number on the Unit-Frequency Response due to Out-of-Phase Torsional Vibrations of a Staggered Flat-Plate Cascade

83-12-22-28

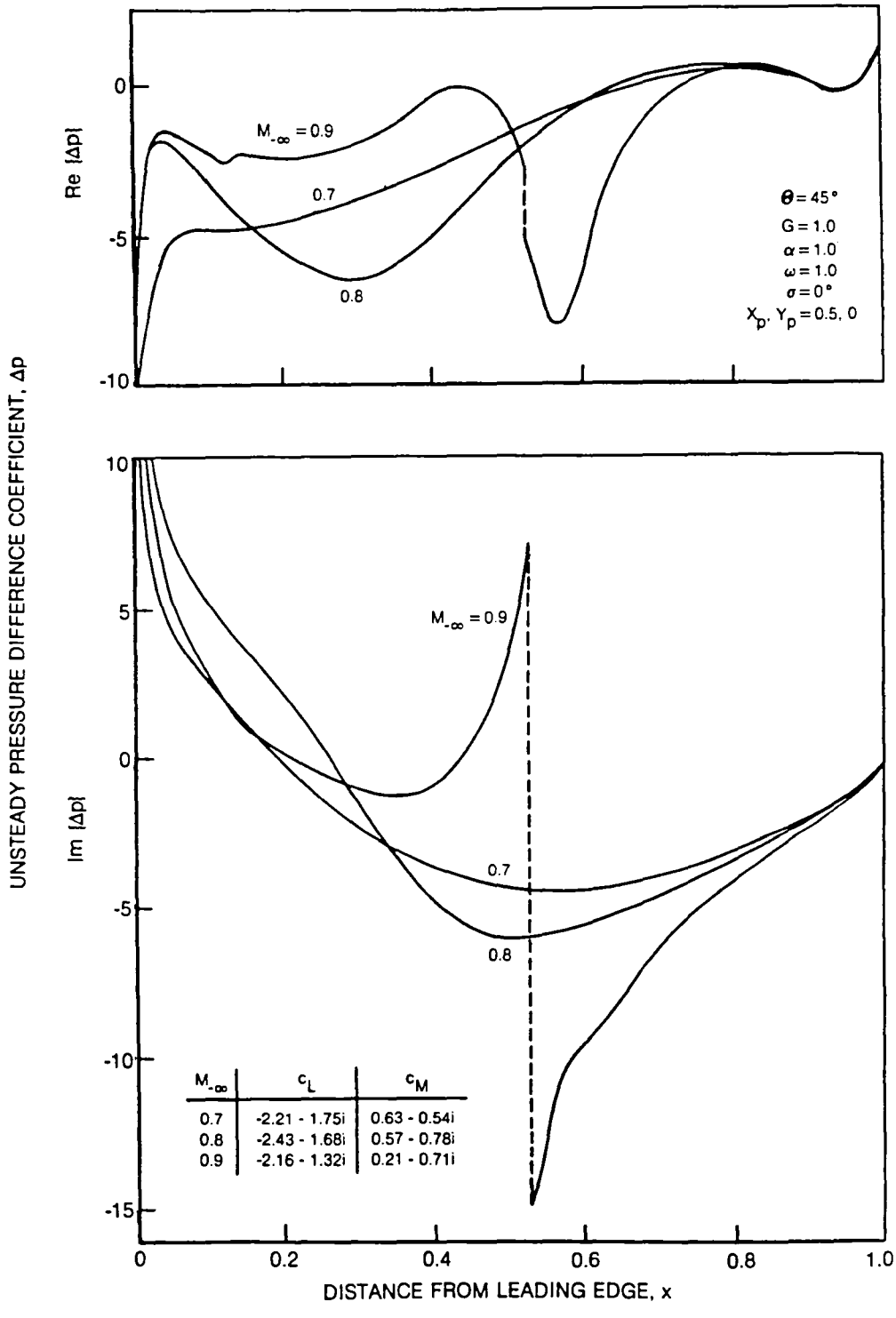

Fig. 29 Effect of Mach Number on the Unit-Frequency Response to In-Phase ($\sigma = 0$ deg.) Torsional Vibrations of a Staggered DCA Cascade

83-12-22-29

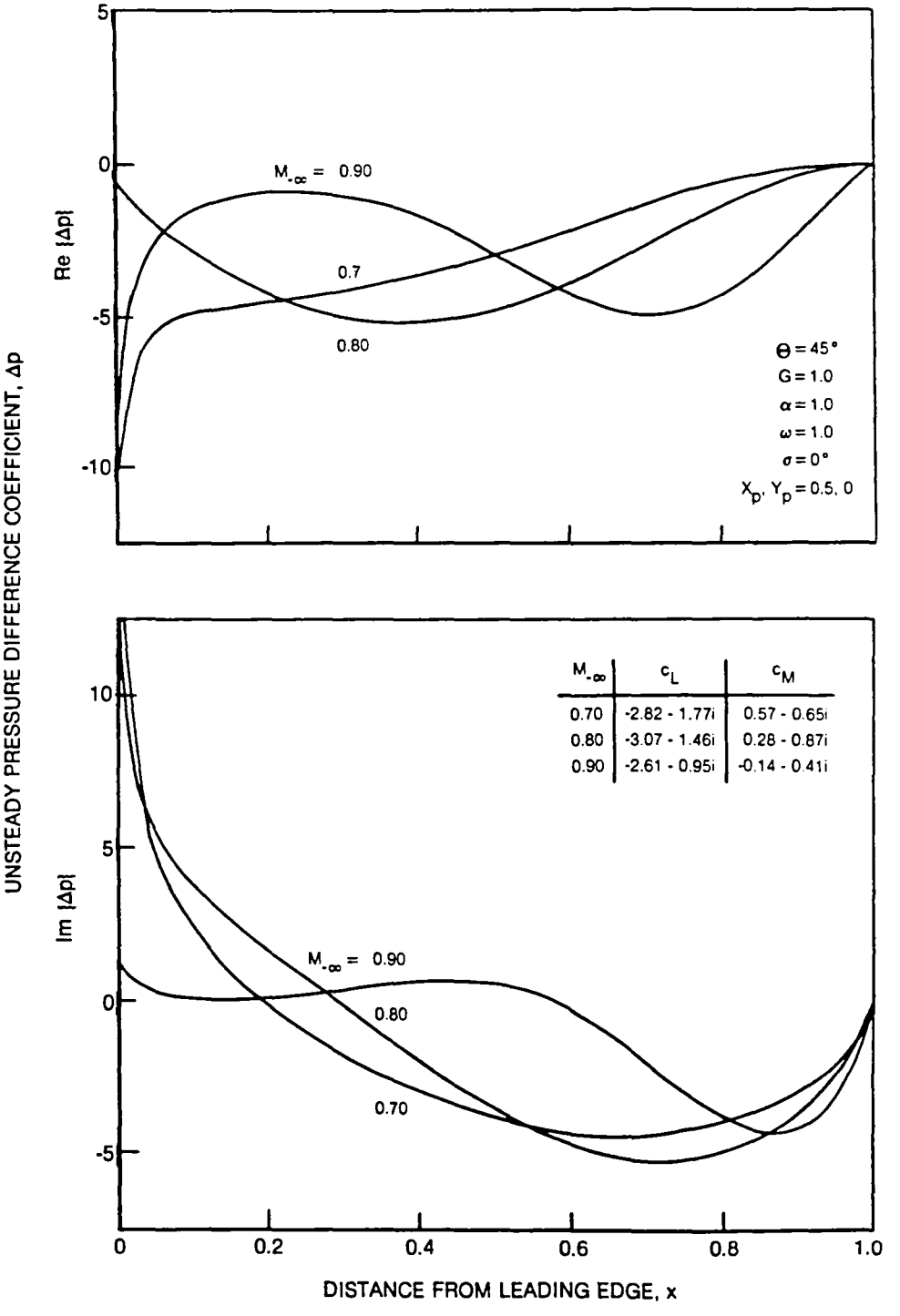

Fig. 30 Effect of Mach Number on the Unsteady Response to In-Phase Torsional Vibrations of a Staggered Flat-Plate Cascade

83-12-22-30

1 Report No	2 Government Accession No	3 Recipient's Catalog No
NASA CR-3833		

4 Title and Subtitle	5 Report Date
A Linear Aerodynamic Analysis for Unsteady Transonic Cascades	September 1984
	6 Performing Organization Code
7 Author(s)	8 Performing Organization Report No
Joseph M. Verdon and Joseph R. Caspar	R84-956393-8
	10 Work Unit No
9 Performing Organization Name and Address United Technologies Research Center Silver Lane East Hartford, Connecticut 06108	11 Contract or Grant No NAS3-23696
	13 Type of Report and Period Covered Contractor Report
12 Sponsoring Agency Name and Address National Aeronautics and Space Administration Washington, D. C. 20546	14 Sponsoring Agency Code 510-55-12 (E-2202)

15 Supplementary Notes

Final report. Project Manager, John J. Adamczyk, Fluid Mechanics and Instrumentation Division, NASA Lewis Research Center, Cleveland, Ohio 44135.

16 Abstract

A potential flow analysis is presented for predicting the unsteady airloads produced by the vibrations of turbomachinery blades operating at transonic Mach numbers. The unsteady aerodynamic model includes the effects of blade geometry, finite mean pressure variation across the blade row, high-frequency blade motion, and shock motion within the framework of a linearized, frequency-domain formulation. The unsteady equations are solved using an implicit, least-squares, finite-difference approximation which is applicable on arbitrary grids. A numerical solution for the entire unsteady field is determined by matching a solution determined on a rectilinear-type cascade mesh, which covers an extended blade-passage region, to a solution determined on a detailed polar-type local mesh, which covers and extends well beyond the supersonic region(s) adjacent to a blade surface. Results are presented for cascades of double-circular-arc and flat-plate blades to demonstrate the unsteady analysis, and to partially illustrate the effects of blade geometry, inlet Mach number, blade-vibration frequency and shock motion on unsteady response.

17 Key Words (Suggested by Author(s))	18 Distribution Statement
Unsteady transonic flow; Two-dimensional, finite-deflection, cascade; Small-amplitude, harmonic, blade vibrations; Shock motion	Unclassified - unlimited STAR Category 02

19 Security Classif. (of this report)	20 Security Classif. (of this page)	21 No. of Pages	22 Price*
Unclassified	Unclassified	79	A05

* For sale by the National Technical Information Service, Springfield, Virginia 22161

NASA-Langley, 1984

National Aeronautics and
Space Administration

Washington, D.C.
20546

Official Business
Penalty for Private Use, $300

THIRD-CLASS BULK RATE

Postage and Fees Paid
National Aeronautics and
Space Administration
NASA-451

NASA

POSTMASTER: If Undeliverable (Section 158 Postal Manual) Do Not Return